

Cost-Effective and Durable Graphene-based Oxygen Electrocatalysts in Alkaline Media

Kaipei Qiu

A thesis presented for the degree of
Doctor of Philosophy

Supervised by:

Prof. Zheng Xiao Guo

Department of Chemistry
University College London, UK

February 2017

Declaration

I, Kaipei Qiu, confirm that this thesis is composed by myself, that the work contained herein is my own except where explicitly stated otherwise in the text, and that this work has not been submitted for any other degree or professional qualification except as specified. Parts of this work have been published in peer-reviewed journals as stated in the List of Publications.

Abstract

Development of cost-effective and durable catalysts for sluggish oxygen reduction reaction (ORR) and oxygen evolution reaction (OER) is imperative to promote critical energy conversion and storage technologies such as fuel cells and metal-air batteries. Low-cost non-precious metal (NPM) and metal-free (MF) catalysts are promising choices to replace commercial noble metal counterparts. However, there exist crucial challenges in developing such catalysts with comparable or superior performance to the noble metals, while ensuring effective cost reduction. Hence, the primary goal of this thesis is to design and develop low-cost graphene-based ORR / OER electrocatalysts in alkaline media, either in the form of MF catalysts or as a support / co-catalyst to NPMs.

Three types of graphene-based systems were designed and evaluated.

- The first system involves “MF for ORR” – Intercalated graphene/graphitic carbon nitride (GCN): It was synthesised through intercalation of graphene by GCN to enhance the electrical conductivity while maintain sufficient catalytic sites. Utilisation of hierarchically porous structures can further increase the accessible active sites and improve mass transfer. The optimised structure shows comparable ORR activity and superior durability to commercial Pt/C.
- The second system is based on “NPM for ORR” – Maghemite embedded N-doped graphene framework ($\gamma\text{-Fe}_2\text{O}_3/\text{N-GF}$): The hierarchical N-GF substrate was firstly

optimised to achieve high pore volume for rapid mass transfer, and then incorporated by an appropriate amount of $\gamma\text{-Fe}_2\text{O}_3$, via “one-pot” synthesis, to boost reduction potentials without compromising active site accessibility. The optimised structure outperforms Pt/C for ORR, both in activity and durability.

- The third system focuses on “MF for bifunctional ORR/OER” – A P,N co-doped graphene framework (PNGF) shows almost identical activity and greater durability than commercial Pt/C for ORR and Ir/C for OER, respectively. Closely coupled first-principle simulations and experiment design show that the OER performance is strongly correlated with P-N bonds, while the ORR activity with N-doped moieties.

Table of Contents

Acknowledgement	- 8 -
List of Publications	- 9 -
List of Figures	- 12 -
Chapter 1. Introduction	- 18 -
Chapter 2. Literature Review	- 21 -
2.1 Oxygen Reduction Reaction (ORR) and Oxygen Evolution Reaction (OER)	- 21 -
2.1.1 Applications – Why does ORR or OER Matter?	- 21 -
2.1.1.1 Fuel Cells	- 26 -
2.1.1.2 Metal-Air Batteries	- 30 -
2.1.2 ORR / OER Mechanisms in Alkaline Electrolytes	- 35 -
2.2 Electrocatalysts for ORR and OER	- 38 -
2.2.1 ORR Catalysts	- 38 -
2.2.1.1 Pt Alloys	- 38 -
2.2.1.2 Non-Precious Metals	- 40 -
2.2.1.3 Metal-Free Materials	- 42 -
2.2.2 OER Catalysts	- 45 -
2.2.2.1 Precious Metals (Oxides)	- 45 -
2.2.2.2 Non-Precious Metals	- 46 -
2.2.2.3 Metal-Free Materials	- 47 -
2.3 Brief Overview of Graphene	- 47 -

2.3.1 Properties of Graphene	- 48 -
2.3.2 Synthesis of Graphene	- 48 -
Chapter 3. Experimental	- 51 -
3.1 Synthesis	- 51 -
3.1.1 Intercalated Graphene / Graphitic Carbon Nitride	- 51 -
3.1.2 Maghemite Embedded Nitrogen Doped Graphene Framework	- 53 -
3.1.3 Phosphorus / Nitrogen Co-Doped Graphene Framework	- 54 -
3.2 Physical Characterisation	- 55 -
3.3 Electrochemical Characterisation	- 55 -
Chapter 4. Intercalated Graphene / Graphitic Carbon Nitride	- 58 -
4.1 Introduction	- 58 -
4.2 Results and Discussion	- 61 -
4.3 Summary	- 81 -
Chapter 5. Maghemite Embedded Nitrogen Doped Graphene Framework	- 82 -
5.1 Introduction	- 82 -
5.2 Results and Discussion	- 85 -
5.2.1 Formation of Highly Porous N-doped Graphene Framework	- 85 -
5.2.2 Nano-confinement of Maghemite Catalysts	- 92 -
5.2.3 Comparison of Catalytic Activities.	- 98 -
5.3 Summary	- 110 -
Chapter 6. Phosphorus / Nitrogen Co-doped Graphene Framework	- 111 -
6.1 Introduction	- 111 -
6.2 Results and Discussion	- 114 -

6.3. Summary

- 128 -

Chapter 7. Conclusion and Future Work

- 129 -

References

- 134 -

Acknowledgement

I would like to express sincere gratitude to my PhD supervisor, Prof. Zheng Xiao Guo, for his guidance on my research project and kind support to my skills and career development. I would also like to thank my colleagues and collaborators, including Prof. Guo-Liang Chai, Prof. Maria-Magdalena Titirici, Prof. Junwang Tang, Prof. Wenjun Luo, Dr Yiwen Wang, Dr Bingjun Zhu, Mr. Chaoran Jiang, Mr. Min Ling, and Ms. Mo Qiao, for their insightful comments and helpful suggestions on my experimental design, results interpretation, and paper writing. Special thanks will be given to my wife, Mrs Yutian Lei, and my parents, Mr Huosheng Qiu and Mrs Aihong Pei - I couldn't have possibly done my PhD without their continuous support and encouragement.

List of Publications

1. **Highly Efficient Oxygen Reduction Catalysts by Rational Synthesis of Nanoconfined Maghemite in a Nitrogen-Doped Graphene Framework**

Kaipei Qiu, Guo-Liang Chai, Chaoran Jiang, Min Ling, Junwang Tang, and Zheng Xiao Guo

ACS Catalysis, **2016**, 6, 3558–3568. [DOI: 10.1021/acscatal.6b00531](https://doi.org/10.1021/acscatal.6b00531)

2. **Hierarchically Porous Graphene Sheets and Graphitic Carbon Nitride Intercalated Composites for Enhanced Oxygen Reduction Reaction**

Kaipei Qiu and Zheng Xiao Guo

Journal of Materials Chemistry A, **2014**, 2, 3209–3215. [DOI:10.1039/C3TA14158F](https://doi.org/10.1039/C3TA14158F)

3. **Highly Efficient Photocatalytic H₂ Evolution from Water using Visible Light and Structure-Controlled Graphitic Carbon Nitride**

David James Martin, Kaipei Qiu, Stephen Andrew Shevlin, Albertus Denny Handoko, Xiaowei Chen, Zheng Xiao Guo, and Junwang Tang

Angewandte Chemie International Edition, **2014**, 53, 9240–9245. [DOI: 10.1002/anie.201403375](https://doi.org/10.1002/anie.201403375)

4. **Naturally Derived Porous Carbon with Selective Metal- and/or Nitrogen-Doping for Efficient CO₂ Capture and Oxygen Reduction**

Bingjun Zhu, Kaipei Qiu, Congxiao Shang, and Zheng Xiao Guo

Journal of Materials Chemistry A, **2015**, 3, 5212–5222. [DOI: 10.1039/C4TA06072E](https://doi.org/10.1039/C4TA06072E)

5. Soy Protein Directed Hydrothermal Synthesis of Porous Carbon Aerogels for Electrocatalytic Oxygen Reduction

Sara-Maaria Alatalo, Kaipei Qiu, Kathrin Preuss, Adam Marinovic, Marta Sevilla, Mika Sillanpää, Zheng Xiao Guo, and Maria-Magdalena Titirici

Carbon, **2016**, 96, 622–630. [DOI:10.1016/j.carbon.2015.09.108](https://doi.org/10.1016/j.carbon.2015.09.108)

6. Selective Morphologies of MgO via Nanoconfinement on γ -Al₂O₃ and Reduced Graphite Oxide (rGO): Improved CO₂ Capture Capacity at Elevated Temperatures

Xiaoxue Zhang, Kaipei Qiu, Erkki Levänen, and Zheng Xiao Guo

CrystEngComm, **2014**, 16, 8825–8831. [DOI: 10.1039/C4CE01258E](https://doi.org/10.1039/C4CE01258E)

7. Graphene / Nitrogen-Doped Porous Carbon Sandwiches for the Metal-Free Oxygen Reduction Reaction: Conductivity versus Active Sites

Mo Qiao, Cheng Tang, Guanjie He, Kaipei. Qiu, Russell Binions, Ivan. Parkin, Qiang Zhang, Zheng Xiao Guo, and Maria-Magdalena Titirici

Journal of Materials Chemistry A, **2016**, 4, 12658–12666. [DOI: 10.1039/C6TA04578B](https://doi.org/10.1039/C6TA04578B)

8. Highly-Crystallized α -FeOOH for Stable and Efficient Oxygen Evolution Reaction

Wenjun Luo, Chaoran Jiang, Yaomin Li, Stephen Andrew Shevlin , Xiaoyu Han,
Kaipei Qiu, Yingchun Cheng, Zheng Xiao Guo, Wei Huang, and Junwang Tang

Journal of Materials Chemistry A, **2017**, 5, 2021-2028. [DOI: 10.1039/C6TA08719A](https://doi.org/10.1039/C6TA08719A)

**9. Active Sites Engineering Leads to Exceptional ORR and OER Bifunctionality
in P, N Co-Doped Graphene Frameworks**

Guo-Liang Chai, Kaipei Qiu (co-first author), Mo Qiao, Maria-Magdalena Titirici,
Congxiao Shang, and Zheng Xiao Guo,

Energy & Environmental Science, **2017** (Under Review).

List of Figures

Figure 1-1. A typical example of ORR / OER activity volcano.	- 18 -
Figure 1-2. Computationally predicated ORR / OER overpotentials for heteroatom doped graphene, compared with Pt for ORR and RuO ₂ for OER.	- 19 -
Figure 2-1. Summary of reactions and processes in various fuel cell systems.	- 22 -
Figure 2-2. Schematic structures of metal-air batteries.	- 23 -
Figure 2-3. Dependence of the cell voltage of a galvanic cell on the current load.	- 24 -
Figure 2-4. Comparison of energy conversion efficiency in a heat engine and H ₂ -O ₂ electrochemical fuel cell.	- 25 -
Figure 2-5. Schematic polarization curves of zinc-air cell.	- 25 -
Figure 2-6. Schematic illustration of AFC with a circulating electrolyte.	- 27 -
Figure 2-7. Schematic illustration of PEMFC stacks.	- 28 -
Figure 2-8. Schematic illustration of IMFC and DMFC.	- 29 -
Figure 2-9. Schematic illustration of SOFC.	- 30 -
Figure 2-10. Schematic illustration of ZAB with a tri-electrode configuration.	- 32 -
Figure 2-11. Schematic illustration of non-aqueous Li-O ₂ battery.	- 34 -
Figure 2-12. Reduction mechanism in a Li-O ₂ cell at low overpotentials.	- 34 -
Figure 2-13. Activity volcano for HER with respect to the binding strength of H*.	- 36 -
Figure 2-14. ORR / OER activity volcano for carbon based materials.	- 37 -
Figure 2-15. Activity volcano for Pt-alloy ORR catalysts.	- 39 -
Figure 2-16. Ever rising ORR activity of Pt-Ni alloy catalysts with (111) facets.	- 40 -

- Figure 2-17.** Schematic representation of two kinds of MeNC catalysts: (a) MeN_xC moieties, and (b) Me-N-C coupled interface. - 41 -
- Figure 2-18.** Typical atomic configuration of different types of dopants at different doping sites in the graphene matrix. - 43 -
- Figure 2-19.** ORR activity volcano of heteroatom doped graphene with regard to the binding of OOH^* intermediate. - 44 -
- Figure 2-20.** Overview of the state-of-the-art electrocatalysts for OER. - 45 -
- Figure 2-21.** Overpotentials of NPM OER catalysts at 10 mA cm^{-2} . - 46 -
- Figure 4-1.** Electron microscope images of GCN, GS and GSGCN composites. - 62 -
- Figure 4-2.** XRD of GO, GS, GCN and GS/GCN intercalated composites.错误! 未定义书签。
- Figure 4-3.** Nitrogen isotherms for GS/GCN intercalated composites at 77K.错误! 未定义书签。
- Figure 4-4.** BET SSA of GCN and GS/GCN intercalated composites, derived from N_2 isotherms at 77 K. - 64 -
- Figure 4-5.** FTIR of GO, GS, GCN and GS/GCN intercalated composites. - 65 -
- Figure 4-6.** XPS C1s spectra for GO, GS, GCN and GS/GCN composites. - 66 -
- Figure 4-7.** Pyridinic N content of GCN and GS/GCN intercalated composites. - 67 -
- Figure 4-8.** TG patterns for GS, GCN and GS/GCN intercalated composites. - 68 -
- Figure 4-9.** GS content and nitrogen content of GS/GCN intercalated composites. - 68 -
- Figure 4-10.** CV of GCN and GS/GCN intercalated composites. - 69 -
- Figure 4-11.** LSV of GCN and GS/GCN intercalated composites at 2000 RPM. - 70 -
- Figure 4-12.** E-SSA and E-SSA normalized peak current for GS/GCN composites. - 72 -

Figure 4-13. SEM image of hp-GSGCN_2x.	- 73 -
Figure 4-14. HRTEM image of hp-GSGCN_2x.	- 74 -
Figure 4-15. CV of GSGCN_2x and hp-GSGCN_2x.	- 76 -
Figure 4-16. LSV of GSGCN_2x, hp-GSGCN_2x and Pt/C at 1500 RPM.	- 76 -
Figure 4-17. LSV of GSGCN_2x and hp-GSGCN_2x at 500 - 2000 RPM.	- 77 -
Figure 4-18. K-L plots of GSGCN_2x and hp-GSGCN_2x at -0.4 V.	- 77 -
Figure 4-19. Electron transfer number for GSGCN_2x and hp-GSGCN_2x.	- 78 -
Figure 4-20. Tafel plots of GSGCN_2x and hp-GSGCN_2x.	- 78 -
Figure 4-21. CA of hp-GSGCN_2x and Pt/C in O ₂ -saturated 0.1M KOH + 3M CH ₃ OH, under 1600 RPM, at -0.3 V vs. Ag/AgCl for methanol tolerance.	- 80 -
Figure 4-22. CA of hp-GSGCN_2x and Pt/C in O ₂ -saturated 0.1M KOH, under 1600 RPM, at -0.3 V vs. Ag/AgCl for long-term stability.	- 80 -
Figure 5-1. SEM image of GF.	- 86 -
Figure 5-2. SEM image of GF+N ₂ .	- 86 -
Figure 5-3. SEM image of GF+800.	- 87 -
Figure 5-4. SEM image of GF+N ₂ _800.	- 87 -
Figure 5-5. TGA of GF and GF+N ₂ under N ₂ with a ramping rate of 3 °C min ⁻¹ .	- 88 -
Figure 5-6. Raman spectra of GO, GF_800, and GF+N_800.	- 89 -
Figure 5-7. N ₂ adsorption / desorption isotherms at 77K for GF+N.	- 90 -
Figure 5-8. N ₂ adsorption / desorption isotherms at 77K for GF+N_800.	- 90 -
Figure 5-9. PSD of GF+N derived from N ₂ isotherms at 77 K.	- 91 -
Figure 5-10. PSD of GF+N_800 derived from N ₂ isotherms at 77 K.	- 91 -
Figure 5-11. N ₂ adsorption / desorption isotherms at 77K for GF+N+Fe_800.	- 93 -

- Figure 5-12.** PSD of GF+N+Fe_800 derived from N₂ isotherms at 77 K. - 93 -
- Figure 5-13.** XRD pattern of GF+N₂+Fe1_800. - 95 -
- Figure 5-14.** XPS Fe2p spectrum of GF+N₂+Fe1_800. - 95 -
- Figure 5-15.** XPS N1s spectra of GF+N₂+Fe_800. - 96 -
- Figure 5-16.** TEM image of GF+N₂+Fe1_800. - 97 -
- Figure 5-17.** HRTEM image of GF+N₂+Fe1_800. - 97 -
- Figure 5-18.** LSV plots of GF+N_800 under 1600 RPM. - 98 -
- Figure 5-19.** LSV plots of GF+N₂+Fe_800 under 1600 RPM. - 99 -
- Figure 5-20.** LSV plots of GF+N+Fe_800 under 1600 RPM. - 100 -
- Figure 5-21.** Comparison of K-L plots at 0.65 V vs. RHE. - 101 -
- Figure 5-22.** Comparison of kinetic current densities J_k at 0.65 V vs. RHE and reduction potentials at 3 mA cm⁻². - 102 -
- Figure 5-23.** RRDE measurement of GF+N₂_800, GF+N₂+Fe1_800, GF+N₂+Pt1_800 and PtC. - 103 -
- Figure 5-24.** Peroxide formation of GF+N₂_800, GF+N₂+Fe1_800 and PtC. - 103 -
- Figure 5-25.** Tafel plots of GF+N₂_800, GF+N₂+Fe1_800 and PtC. - 104 -
- Figure 5-26.** Tafel plots of GF+N₂+Pt1_800 and GF+N₂+Fe1_800. - 104 -
- Figure 5-27.** EIS Nyquist plots of GF+N₂_800, GF+N₂+Fe1_800 and PtC. - 106 -
- Figure 5-28.** The electrode performance of GF+N₂_800, GF+N₂+Fe1_800 and PtC in 0.1M and 6M KOH. - 106 -
- Figure 5-29.** CA of GF+N₂+Fe1_800 and PtC in O₂-saturated 0.1M KOH, under 1600 RPM, at an initial ORR current of 3 mA cm⁻². - 108 -
- Figure 5-30.** LSV of GF+N₂+Fe1_800 before and after 5000 scans at 1600 RPM

between 1.0 - 0.4 V vs. RHE.

- 108 -

Figure 5-31. Comparison of the ORR potentials at the current densities of 0.5 and 3 mA cm⁻² for GF+N2+Fe1_800, PtC, and other recently reported Fe-based catalysts, measured by RDE under 1600 RPM.

- 109 -

Figure 6-1. The structures of P-doping and P,N co-doping sites. 错误! 未定义书签。

Figure 6-2. The structures of Z-PN-5-OX2 and Stone-Wales N-doping.错误! 未定义书签。

Figure 6-3. ORR / OER limiting potentials for Z-NP-5-OX2 and Stone-Wales defect structures. 错误! 未定义书签。

Figure 6-4. XPS P2p spectra for PNGF_DAP and PNGF_DAP_800.

- 115 -

Figure 6-5. XPS N1s spectra for PNGF_DAP and PNGF_DAP_800.

- 116 -

Figure 6-6. ORR / OER activities of PNGA_DAP and PNGF_DAP_800.

- 117 -

Figure 6-7. ETN and J_k of PNGA_DAP and PNGF_DAP_800 at 0.6 V vs. RHE.

- 118 -

Figure 6-8. ORR LSV for PNGF_DAP.

- 118 -

Figure 6-9. ORR LSV for PNGF_DAP_800.

- 119 -

Figure 6-10. K-L plots of PNGF_DAP and PNGF_DAP(op) at 0.6 V vs. RHE.

- 119 -

Figure 6-11 Relative ratio of P-N, P-C and P-O bonds in PNGF_DAP, PNGF_ADAP and PNGF_ADAP(op).

- 120 -

Figure 6-12. Relative ratio of g-N, 6-N and -NH₂ bonds in PNGF_DAP, PNGF_ADAP and PNGF_ADAP(op).

- 121 -

Figure 6-13. XPS P2p and N1s spectra for PNGF_ADAP and PNGF_ADAP(op).

- 121 -

Figure 6-14. ORR / OER activities of PNGF_DAP, PNGF_ADAP and PNGF_ADAP(op), measured by RDE at 1600 RPM.

- 122 -

Figure 6-15. Correlation between OER activity and PN bond concentrations.	- 123 -
Figure 6-16. OER Tafel plots of PNGF_DAP, PNGF_ADAP and PNGF_ADAP(op).	- 123 -
Figure 6-17. Comparison of ORR / OER activity and durability for PNGF_ADAP(op) and Pt/C+Ir/C before and after potential cycling of 5,000 times.	- 124 -
Figure 6-18. CA of PNGF_ADAP(op) and Pt/C in O ₂ -saturated 0.1M KOH, under 1600 RPM, at an initial ORR current of 3 mA cm ⁻² .	- 125 -
Figure 6-19. CA of PNGF_ADAP(op) and Ir/C in O ₂ -saturated 0.1M KOH, under 1600 RPM, at an initial OER current of 10 mA cm ⁻² .	- 125 -
Figure 6-20. ORR / OER catalytic activity of 0.15 mg cm ⁻² PNGF_ADAP(op).	- 126 -
Figure 6-21. Comparison of ORR / OER activity for the previously reported bifunctional metal-free catalysts.	- 127 -
Scheme 2-1. ORR reaction pathways in alkaline electrolytes.	- 36 -
Scheme 5-1. Proposed design principle for efficient NPM ORR catalysts.	- 84 -
Table 2-1. Comparison of different types of metal air batteries..	- 94 -
Table 4-1. Electrical conductivities of GCN, GS and GS/GCN composites.	- 72 -
Table 5-1. Summary of BET SSA, total pore volumes, elemental ratios, XPS C1s / N1s binding configurations for GF+N and GF+N_800.	- 92 -
Table 5-2. BET SSA and total PV of GF+N+Fe_800.	- 94 -

Chapter 1. Introduction

Oxygen reduction reaction (ORR) and oxygen evolution reaction (OER) are crucial for energy conversion and storage (ECS).¹⁻³ However, the commercial noble metals catalysts to date, such as platinum or iridium / ruthenium based materials generally suffer from cost and stability issues that hinder their large-scale applications.⁴⁻⁶ Development of cost-effective and durable ORR / OER catalysts has attracted considerable research interest as a result of the ever increasing demand on rechargeable metal-air batteries and regenerative fuel cells.⁷⁻¹² The ‘scaling relationship’ between the adsorption of different reaction intermediates during multi-step and multi-electron transfer processes elucidates the origin of ORR / OER overpotentials and catalytic irreversibility, from a thermodynamic point of view, and can be used as guidance for rational design of efficient catalysts, **Figure 1-1**.¹³⁻¹⁶

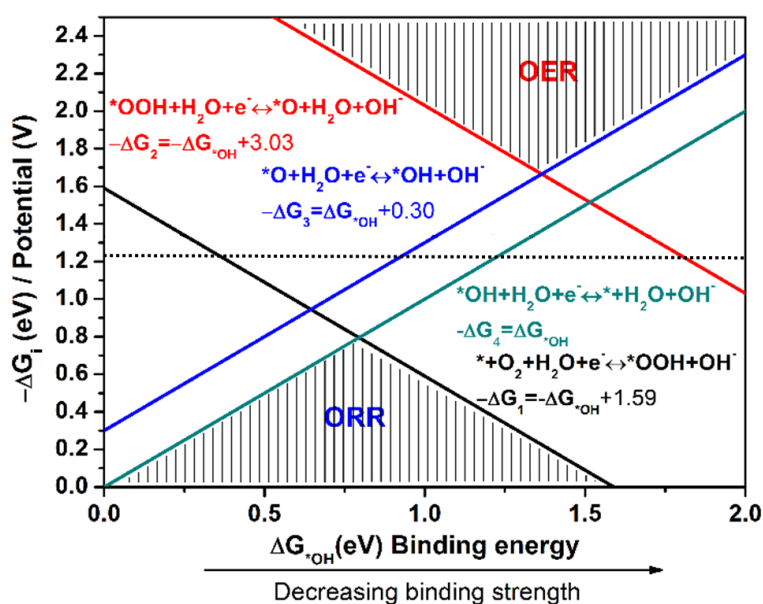


Figure 1-1. A typical example of ORR / OER activity volcano.¹³

Recently, graphene has attracted great attention for applications in electrocatalysis, due to its high electrical conductivity, large surface area and flexibility for structural modifications.¹⁷⁻²⁰ Computational simulations have predicted the possibility to design heteroatom-doped graphene based catalysts with comparable or even superior ORR / OER performance to the noble metal (oxide) counterparts, **Figure 1-2**.^{13, 21-23} However, there exist critical challenges in developing such catalysts while ensuring effective cost reduction in raw materials and synthesis.²⁴ Moreover, the thermodynamic instability of graphene based materials (mainly in the form of sp^2 carbon), especially at high potentials for OER, is another big issue to solve to ensure their long time operation.²⁵

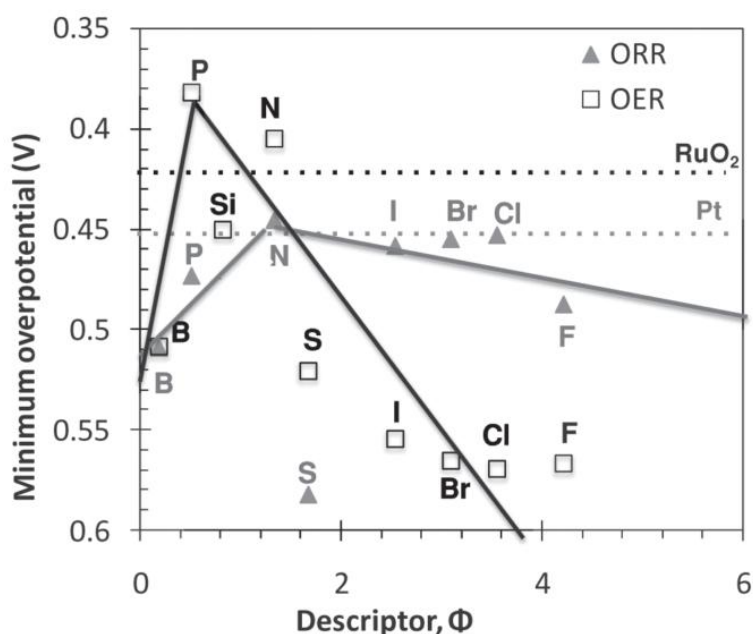


Figure 1-2. Computationally predicated ORR / OER overpotentials for heteroatom doped graphene, compared with Pt for ORR and RuO₂ for OER, respectively.²²

The relatively more rapid ORR / OER kinetics in alkaline than in acidic electrolytes allows the use of a broad range of low-cost non-precious metal (NPM) and metal-free (MF) catalysts to replace commercial noble metal counterparts.²⁶⁻²⁹ Hence the primary

goal of this thesis is to design and develop graphene-based ORR / OER electrocatalysis in alkaline media, either in the form of MF catalysts or as a support / co-catalyst to NPMs. An extensive literature survey with regard to the ORR- / OER-involving ECS techniques, the current research status of catalysts development and the property and synthesis of graphene will firstly be given in **Chapter 2**. Based on these understandings, three types of graphene-based systems have been designed: (1) intercalated graphene / graphitic carbon nitride as MF ORR catalysts, **Chapter 4**; (2) maghemite embedded N-doped graphene framework as NPM ORR catalysts, **Chapter 5**; and (3) P,N co-doped graphene framework as MF bifunctional ORR / OER catalysts, **Chapter 6**. Structural and electrochemical investigations have confirmed that all those three graphene based catalysts can demonstrate comparable or superior activity and exceptional durability to the respective commercial noble metal catalysts. Detailed experimental procedures for synthesis, characterisation, and evaluation of the developed catalysts have been provided in **Chapter 3**.

Chapter 2. Literature Review

2.1 Oxygen Reduction Reaction (ORR) and Oxygen Evolution Reaction (OER)

Electrocatalytic oxygen reduction and evolution reactions are at the heart of fuel cells, metal-air batteries, and etc. The sluggish kinetics of ORR and OER, featured by large overpotentials, represents one of the major bottlenecks in these critical enabling technologies for energy conversion and storage (ECS). In this chapter, the ORR- and OER-involving applications will firstly be overviewed, followed by a description of ORR / OER mechanisms and origin of overpotentials with a particular focus on the reaction pathway in alkaline electrolytes, pointing out the urgent need for development of cost-effective and durable ORR / OER catalysts.

2.1.1 Applications – Why does ORR or OER Matter?

The chemical energy stored in hydrogen and several hydrocarbon fuels is significantly higher than that found in common battery materials.⁴ This fact provides the impetus to develop fuel cells for a variety of applications. Fuel cells are an ideal primary energy conversion device for remote site locations and find application where an assured electrical supply is required for power generation, distributed power, remote, and uninterruptible power.³⁰ **Figure 2-1** depicts the operation of typical fuel cells.

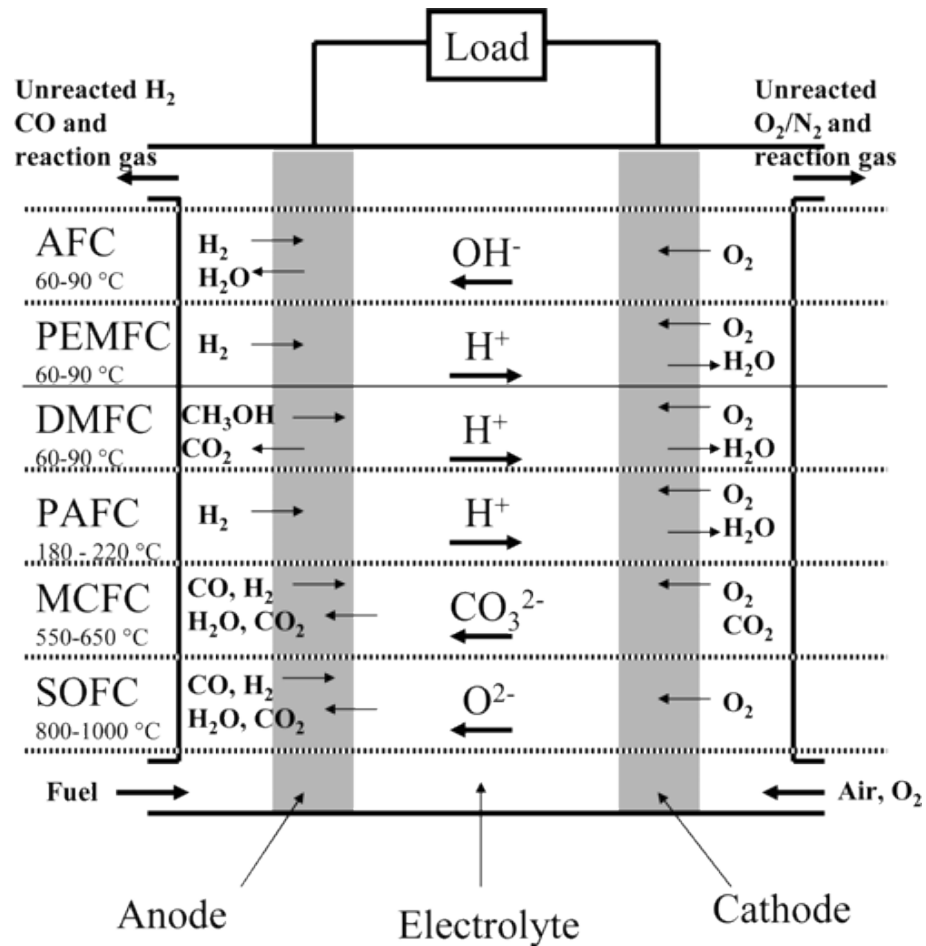


Figure 2-1. Summary of reactions and processes in various fuel cell systems.³⁰

Metal-air batteries are another type of promising ECS systems which combine metal anodes with high energy density and air electrodes with an open structure to draw cathode active materials (i.e., oxygen) from air, **Figure 2-2.**³¹⁻³³ Given that the cathode oxygen is not stored in the cell (similar to fuel cells) and meanwhile the anode metal possesses a high ratio of valence electrons to atomic nuclei, the theoretical specific energy of metal air batteries (e.g. 5,210 or 1,090 Wh kg⁻¹ for Lithium-air or Zinc-air batteries, respectively) can be considerably higher than the state-of-the-art Lithium-ion batteries (e.g. 100-265 Wh kg⁻¹).³³

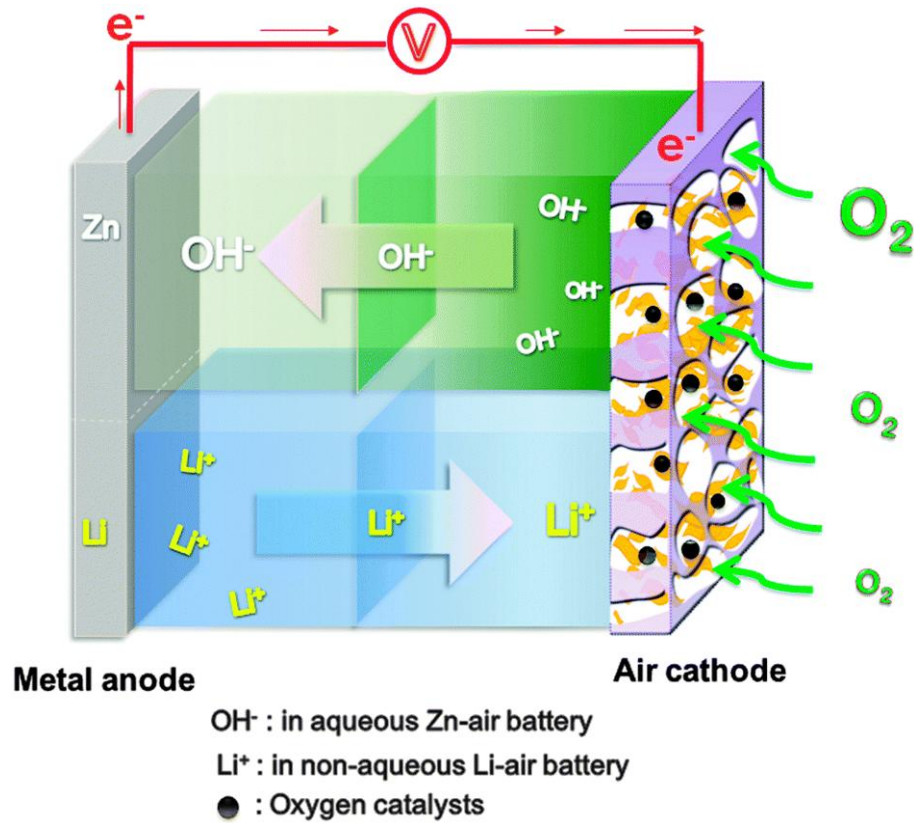


Figure 2-2. Schematic structures of metal-air batteries (aqueous Zn-air and non-aqueous Li-air)

composed of a metal as the anode and a porous air electrode as the cathode.³²

Note that the thermodynamic efficiency (ξ_{th}) of an electrochemical energy conversion process, **Figure 2-3**, is defined by **Equation 2-1**:³⁴

$$\xi_{th} = \frac{\Delta G}{\Delta H} = 1 - \frac{T\Delta S}{\Delta H} = \frac{E^0}{E_H^0} \quad \text{Eq. 2-1}$$

The free energy ΔG , the maximum electric work obtainable from a chemical reaction, is defined by **Equation 2-2**:

$$\Delta G = -nFE^0 \quad \text{Eq. 2-2}$$

Where n is the number of electron transferred in the overall reaction, F is the faraday constant (96485 C mol^{-1}) and E^0 is the thermodynamic cell voltage.

Moreover, the reaction enthalpy ΔH , the heat delivered by the chemical reaction, is defined by **Equation 2-3**, according to the Gibbs-Helmholtz equation:

$$\Delta H = \Delta G + T\Delta S = -nFE_H^0$$

Eq. 2-3

Where ΔS is the reaction entropy and E_H^0 is thermal cell voltage.

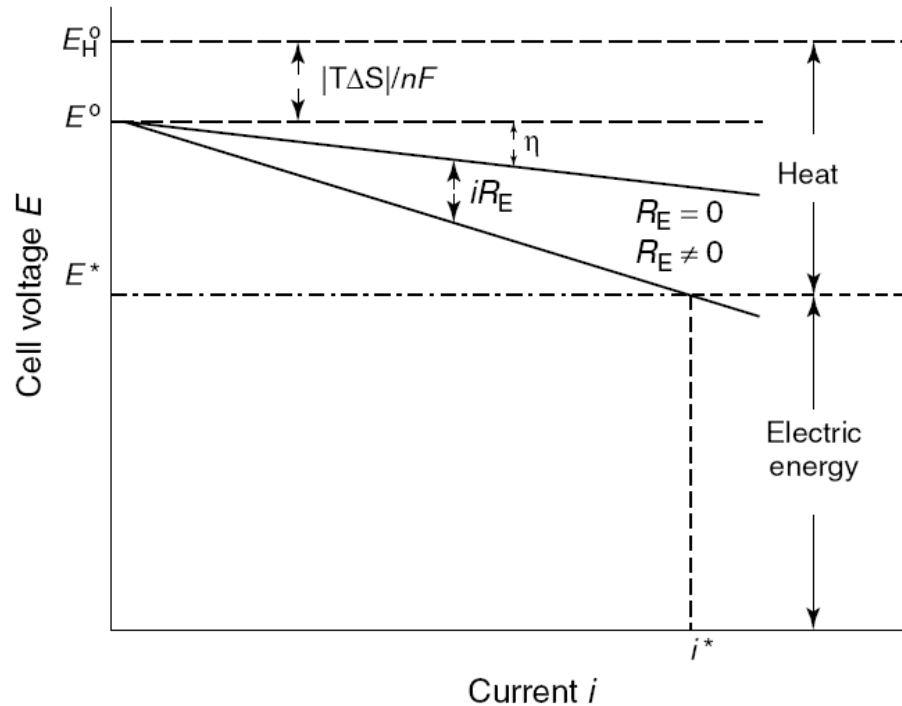


Figure 2-3. Dependence of the cell voltage E^* of a galvanic cell (with reaction entropy $\Delta S < 0$) on the current load, i^* . η is overpotential at the electrodes and R_E is electrolyte resistance.³⁴

As a result, for a fuel cell reaction with $\Delta S < 0$, e.g. $H_2 + 1/2 O_2 = H_2O$, E^0 is 1.23 and E_H^0 is 1.48 V, giving a thermodynamic efficiency ξ_{th} of 0.83.³⁴ The theoretical efficiency of an electrochemical fuel cell system is much higher than a conventional heat engine limited by Carnot efficiency, especially at low temperature (**Figure 2-4**), which is one of the key advantages of fuel cells.³⁵ This also indicates that a low temperature fuel cell (e.g. proton exchange membrane fuel cells or alkaline fuel cells, PEMFCs or AFCs) can theoretically be more efficient than a high temperature fuel cell (e.g. solid oxide fuel cells, SOFCs). More details are given in **Section 2.1.1.1**

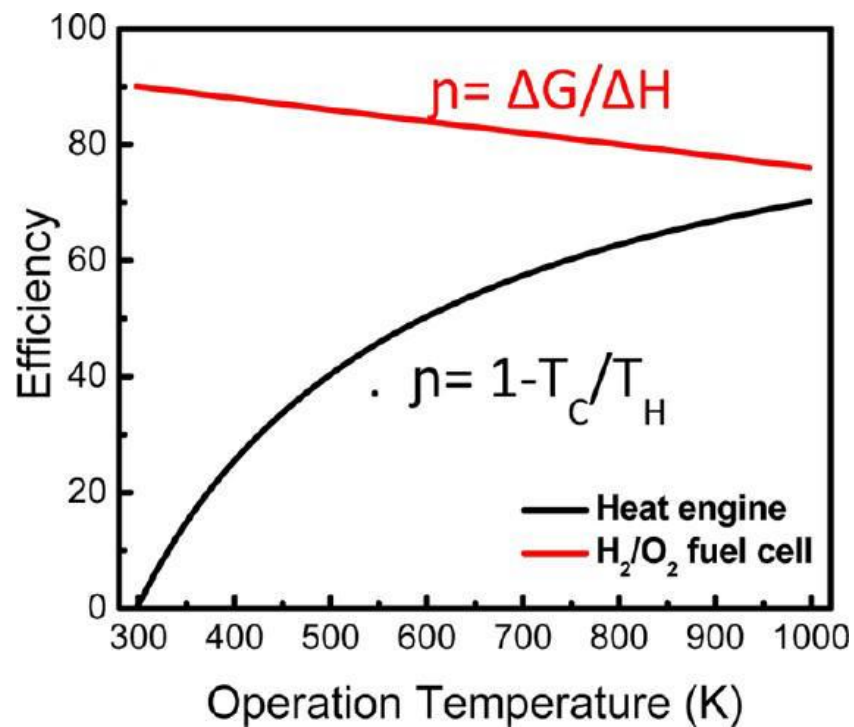


Figure 2-4. Comparison of energy conversion efficiency in a heat engine and H₂-O₂ electrochemical fuel cell.³⁵

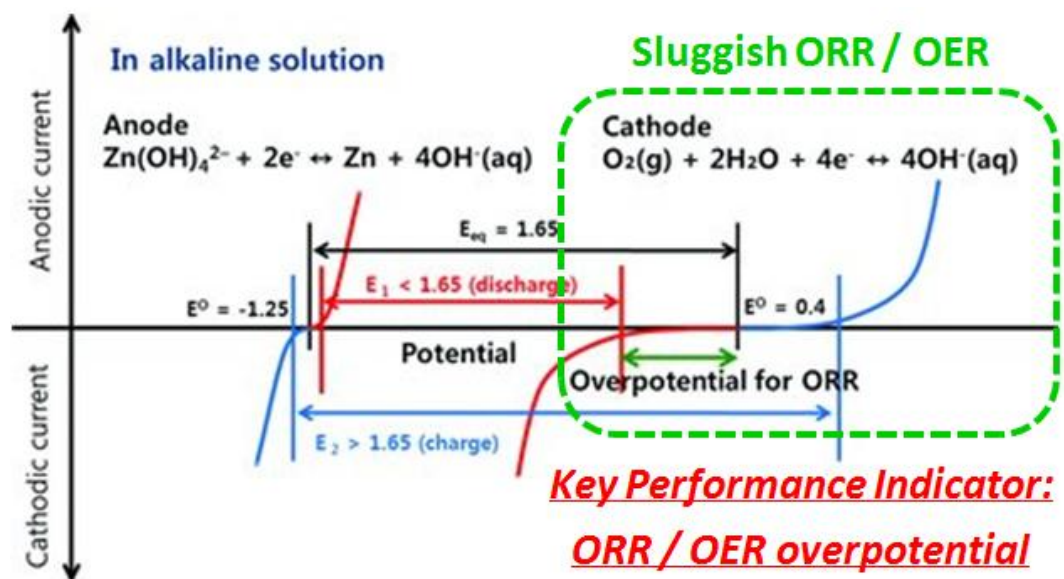


Figure 2-5. Schematic polarization curves of zinc-air cell. The equilibrium potential of the zinc-air cell (black line) is 1.65 V, but the practical voltage (red line) in discharge is lower than 1.65 V due to the sluggish ORR. A large potential is needed to charge zinc-air battery, higher than the equilibrium potential (blue line).³³

The practical efficiency of an electrochemical cell depends on the overpotentials applied to achieve usable current. As shown in the schematic polarisation curve of a zinc-air cell, **Figure 2-5**, the overpotentials required for sluggish cathodic ORR and OER are much larger than those for the anodic reactions.³⁶ Similar situations also occur in, e.g. hydrogen fuel cells where the cathodic ORR is six or more orders of magnitude slower than the anodic hydrogen oxidation reactions,³⁷ which will be further explained in **Section 2.1.2**.

2.1.1.1 Fuel Cells

Alkaline fuel cells (AFCs), or Bacon fuel cells named after its British inventor, are one of the most developed fuel cells technologies. AFCs adopt aqueous alkaline electrolytes (e.g. solutions of potassium or sodium hydroxide) and consume pure oxygen rather than air to prevent the poisoning reaction with atmospheric carbon dioxide (i.e. $\text{CO}_2 + 2\text{KOH} \rightarrow \text{K}_2\text{CO}_3 + \text{H}_2\text{O}$), **Figure 2-6**.³⁸ The less corrosive alkaline electrolytes than strong acidic electrolytes allow much greater latitude in the selection of electrocatalysts and materials of construction on both cathodes and anodes.³⁹

AFCs have been widely applied for space applications by National Aeronautics and Space Administration (NASA) since 1960s, in Apollo-series missions and on the space shuttle, the only applications that could afford costly but efficient $\text{H}_2\text{-O}_2$ fuel cell.³⁹ Since mechanical pumps were not reliable enough, microporous asbestos saturated with immobilized KOH electrolytes were used in NASA space fuel cells. However, such static AFCs may not be suitable for electric vehicle applications, of which the normal operation

requires frequent and safe shut down at ambient conditions for long time periods, causing severe carbon oxidation and faster catalysts degradation at high open circuit voltages. AFCs with circulating electrolytes may help reduce the carbonate formation.³⁸ More recently, novel alkaline membrane fuel cells (AMFCs) have been developed, which is closely related to the polymer electrolyte membrane fuel cells (PEMFCs) except using anion-exchange rather than proton-exchange membranes (PEM).⁴⁰ The most important advantage of using a membrane instead of a liquid electrolyte is the elimination of the negative effects of CO_2 .⁴¹ The conducting species is now in a fixed solid polymer; therefore there will be some carbonates due to the reaction of the OH^- with CO_2 but because there are no mobile cations (i.e. K^+), solid crystals of metal carbonate will not be formed to block the gas diffusion electrodes. At the moment, the membrane conductivity and durability of AMFCs are still not comparable to PEMFCs.⁴¹

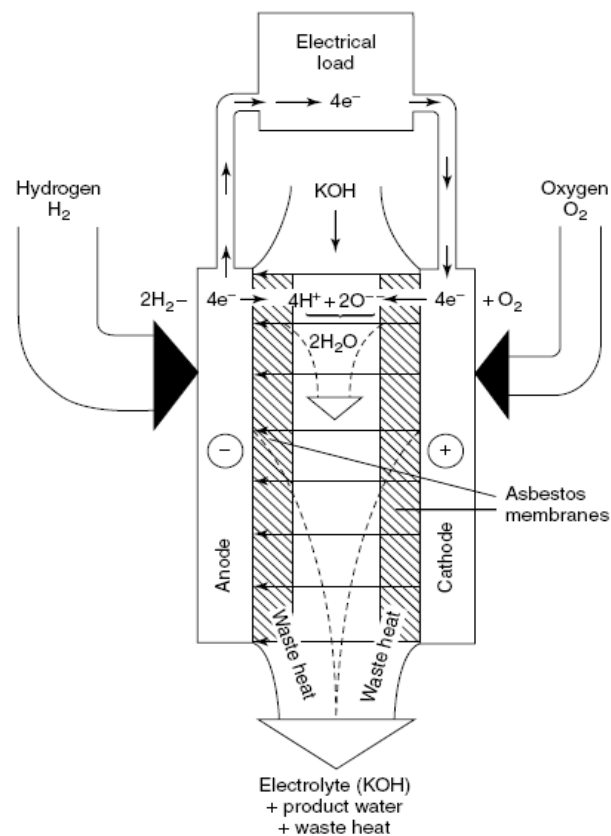


Figure 2-6. Schematic illustration of AFC with a circulating electrolyte.³⁸

PEMFCs have been adopted in commercial fuel cells vehicles (FCV), e.g. Toyota MIRAI and Honda CLARITY. A typical PEMFC is manufactured as a stack of identical repeating unit cells comprising a membrane electrode assembly (MEA) in which hydrogen gas (H_2) is oxidized on the anode and oxygen gas (O_2) is reduced on the MEA cathode, all compressed by bi-polar plates that introduce gaseous reactants and coolants to the MEA and harvest the electric current (**Figure 2-7**).⁴²⁻⁴⁴ The electrochemical reactions occur in the MEA electrodes, each attached to a solid polymer ion exchange membrane that conducts protons but not electrons. The cathodic oxygen reduction reaction (ORR) and anodic hydrogen oxidation reaction both occur on the surfaces of platinum based catalysts. Pure water and heat are the only byproducts. Porous gas diffusion layers transport reactants and product water between the flow fields and catalyst surfaces while exchanging electrons between them.⁴²

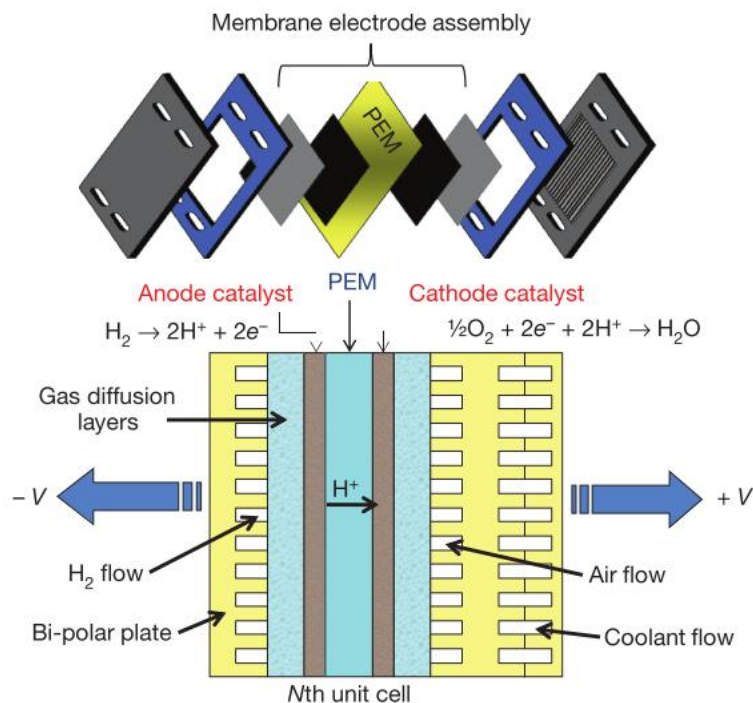


Figure 2-7. Schematic illustration of PEMFC stacks including the components of an expanded MEA.⁴²

Direct-methanol fuel cells, DMFCs, are a sub-category of PEMFCs in which methanol rather than hydrogen is used as the fuel in anodes, **Figure 2-8**.⁴⁵⁻⁴⁷ DMFCs do not have many of the fuel storage problems typical of some fuel cell systems because methanol has a higher energy density than hydrogen – though less than gasoline or diesel fuel.⁴⁵ Methanol is also easier to transport and supply to the public using the current infrastructure because it is a liquid, like gasoline.⁴⁶ DMFCs are often used to provide power for portable fuel cell applications such as cell phones or laptop computers.⁴⁷

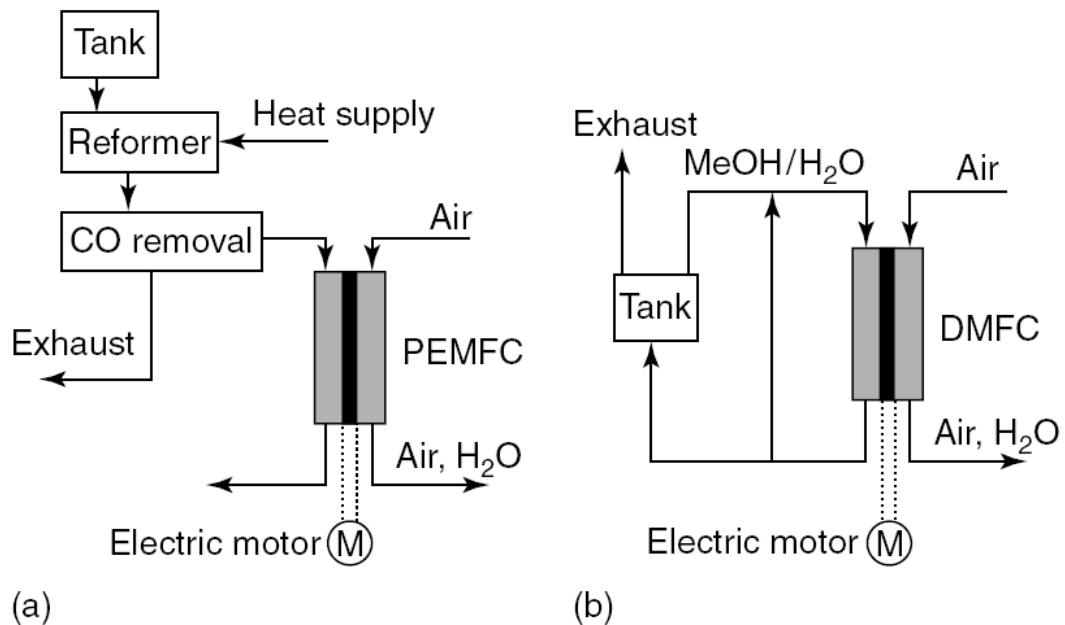


Figure 2-8. Schematic illustration of (a) IMFC, indirect methanol fuel cell, and (b) DMFC.⁴⁵

Solid oxide fuel cells (SOFCs) use a hard, non-porous ceramic compound as the electrolyte, **Figure 2-9**, and operate typically at, i.e. 850 - 1,000 °C.⁴⁸⁻⁵⁰ In contrast to low temperature fuel cells, high temperature operations remove the need of precious catalysts and fuel reformers, thus reducing the cost of overall systems.⁴⁸ In addition to hydrogen, SOFCs can also use natural gas, biogas, and gases made from coal as fuels. On the other hand, high-temperature operations result in a slow start-up and require

significant thermal shielding to retain heat and protect personnel, which restrict SOFCs to stationary but not transportation applications.⁴⁸ In addition, it places stringent durability requirements on materials.⁴⁹ Current research of SOFCs is devoted to develop low-cost materials with enhanced durability at high temperature or low-temperature SOFCs (i.e. < 700 °C) with comparable performance.⁵¹⁻⁵⁵

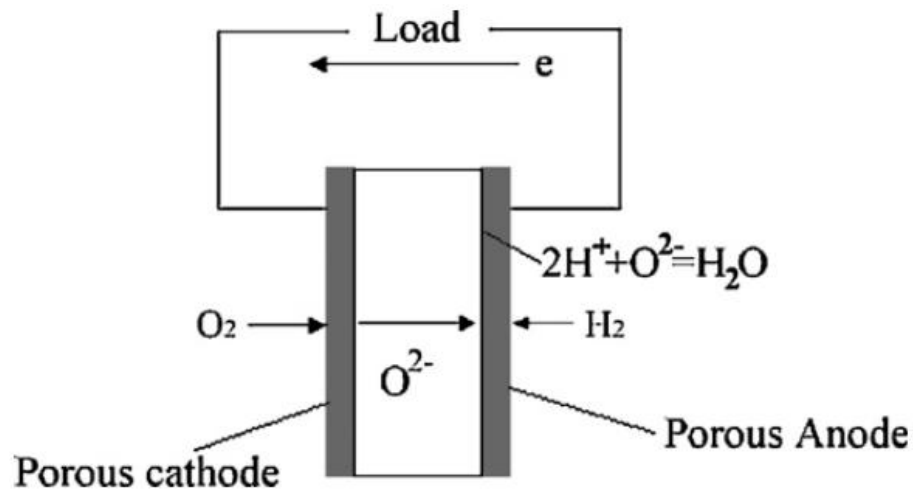


Figure 2-9. Schematic illustration of SOFC.⁴⁹

2.1.1.2 Metal-Air Batteries

Metal-air batteries are between traditional batteries and fuel cells. They have the design features of traditional batteries in which a metal is used as the negative electrode. They also have similarities to conventional fuel cells in that their porous positive electrode structure requires a continuous and inexhaustible oxygen supply from the surrounding air as the reactant, making possible very high theoretical energy densities – about 2-10 fold higher than those of lithium-ion batteries.⁵⁶

Among different types of metal-air batteries, aqueous zinc-air battery (ZAB) is a relatively mature technology.⁵⁷ Primary ZAB has been known to the scientific community

since the late nineteenth century.⁵⁸ Commercial products started to emerge in the 1930s.⁵⁹ ZAB has a high theoretical energy density of 1086 Wh kg^{-1} (including oxygen), about five times higher than the current lithium-ion technology. They can potentially be the least expensive ECS technology with a projected cost of less than $\text{£}100 \text{ kWh}^{-1}$, compared with an average cost of at least $\text{£}250\text{-}300 \text{ kWh}^{-1}$ for lithium-ion batteries (LIB) or all-vanadium redox flow batteries (VRFB).⁶⁰ Major challenges for the wide application of rechargeable ZAB, in spite of its superior energy density and low cost, lie in the relatively low activity (i.e. a power density of 90 W kg^{-1} at the round-trip efficiency of 60%) and the limited lifetime (i.e. lasting for no more than 300-500 cycles without apparent performance loss).⁶¹⁻⁶³

Dendrite formation on zinc anodes is one of the major issues restricting the long-term durability of rechargeable ZAB.³⁶ Over the recent past, the electrolyte compositions and the operational conditions of ZAB have been comprehensively studied and optimised to control the structure and morphology of the deposited zinc: for example, it is found that a $60 \text{ }^\circ\text{C}$ zincate electrolyte with bismuth(III) additives can effectively reduce the growth of zinc dendrites and maintain a good operation for ca. 50 cycles under a current density up to 100 mA cm^{-2} .⁶⁴ Meanwhile, to further extend the ZAB service life, a 'regenerative' flow battery design can be adopted by pumping fresh zincate electrolytes for zinc deposition, which not only prevents the dendrite but also the shape change of zinc anode during cycling and the zinc passivation for an enhanced anode materials utilisation as well.⁶⁵ Hence, the stability of zinc anode and electrolyte should be less of a problem for the lifetime of rechargeable ZAB.⁶⁶ All those point to a pertaining challenge that the durability issues are all related with its air cathode, such as cathode flooding,

electrolyte drying out, carbon corrosion and loss of catalytic materials.³⁶

In order to achieve electrically rechargeable ZAB, recent research has proposed an alternative tri-electrode cell configuration, **Figure 2-10**, i.e., using a third electrode for OER during the charging process in addition to the Zn anode and the normal air cathode for ORR.⁶⁷ Such a cell design, despite complicating the whole battery assembly and manufacturing, allows the use of the corresponding state-of-the-art ORR / OER catalysts for discharging and charging and has been proven significantly improve the cycle life for rechargeable ZAB, compared with the bi-functional electrodes containing the same catalysts.¹⁰

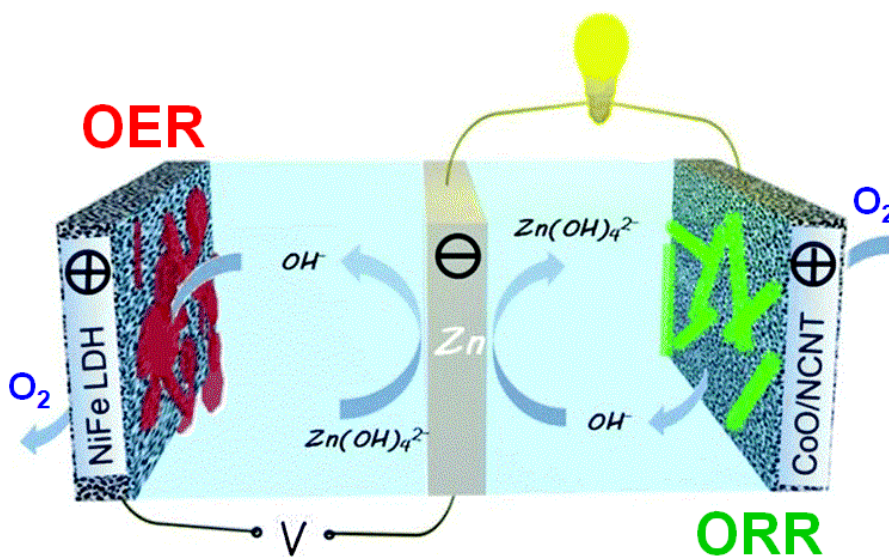


Figure 2-10. Schematic illustration of ZAB with a tri-electrode configuration.⁶⁷

Besides zinc-air batteries, other aqueous metal-air systems such as iron-air, aluminium-air and magnesium-air have also been considered, but are not as favoured as zinc-air.⁶⁸⁻⁷⁰ These batteries were first invented in the 1960s and 1970s (**Table 2-1**).⁷¹⁻⁷³ Among them, iron-air is the only one that can be electrically recharged. Practical iron-air batteries are capable of a long cycle life (> 1000 cycles).⁶⁸ However,

their energy density is not high, typically in the range of 60-80 Wh kg⁻¹, which falls short of the desired target set for electric vehicle applications. Iron-air batteries are mostly intended for grid-scale energy storage because of their low-cost (< £60 kWh⁻¹) and long cycle life.⁶⁸ Aluminium-air and magnesium-air batteries have high theoretical energy densities and working voltages (**Table 2-1**). Unfortunately, practically attainable values are much lower due to the parasitic corrosion reaction evolving hydrogen gas at the metallic negative electrode.^{69, 70} Moreover, aluminium-air and magnesium-air are not electrically rechargeable since the electrodeposition of aluminium and magnesium is not thermodynamically feasible in aqueous electrolytes.³⁶

Battery systems	Fe-air	Zn-air	Al-air	Mg-air	Na-air	K-air	Li-air
Year invented	1968	1878	1962	1966	2012	2013	1996
Cost of metals (\$ kg ⁻¹) ^a	0.40	1.85	1.75	2.75	1.7	~20	68
Theoretical voltage (V)	1.28	1.65	2.71	3.09	2.27	2.48	2.96
Theoretical energy density (Wh kg ⁻¹) ^b	763	1086	2796	2840	1106	935	3458
Electrolyte for practical batteries	Alkaline	Alkaline	Alkaline or saline	Saline	Aprotic	Aprotic	Aprotic
Practical voltage (V)	~1.0	1.0-1.2	1.1-1.4	1.2-1.4	~2.2	~2.4	~2.6
Practical energy density (Wh kg ⁻¹)	60-80	350-500	300-500	400-700	Unclear ^c	Unclear ^c	Unclear ^c
Primary (P) or electrically recharge-able (R)	R	R	P	P	R	R	R

^a Data source: <http://www.metalprices.com>. ^b Oxygen inclusive. ^c Reported values in literature were normalized to the mass of catalysts.

Table 2-1. Comparison of different types of metal air batteries.³⁶

Non-aqueous organic electrolytes can be used to prevent the hydrogen evolution side reaction that commonly occurs on various metallic negative electrodes during the charging process in aqueous electrolytes. Typically, non-aqueous lithium-air, sodium-air and potassium-air batteries were introduced to the public and have gained rapidly increasing attention.⁷⁴⁻⁷⁷ Lithium-air is particularly appealing due to its very high theoretical energy density (i.e. 3458-5210 Wh kg⁻¹, dependent on the final product).⁷⁷ Nonaqueous metal-air batteries have a starkly different battery electrochemistry from their aqueous counterparts, **Figure 2-11**.⁷⁸ ORR in organic solvents proceeds at a rate

orders of magnitude slower than in aqueous electrolytes.³¹ This leads to the formation of insoluble metal peroxide or superoxide particles, the accumulation of which at the air electrode blocks oxygen diffusion, and gradually shuts off battery reactions.⁷⁹⁻⁸³ The latest mechanistic investigations by Bruce et al., **Figure 2-12**, reveal that promotion of discharge in solution is the key to reduce overpotentials and enhance durability.^{82, 83}

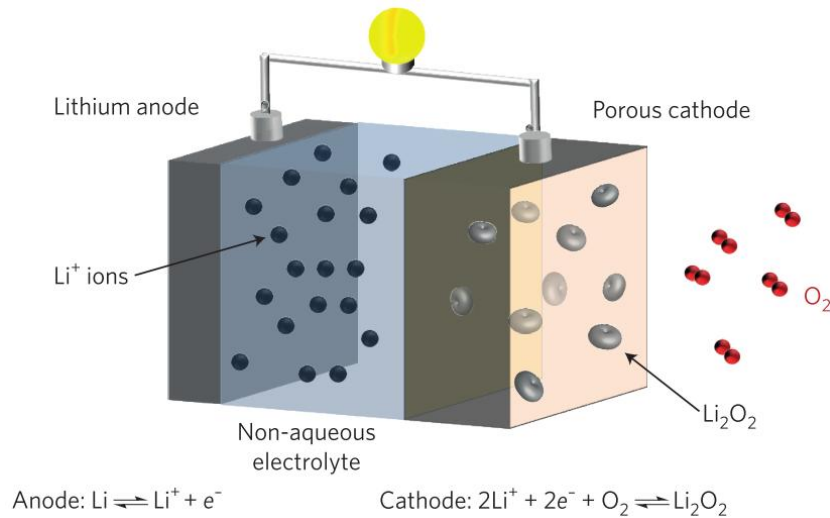


Figure 2-11. Schematic illustration of non-aqueous Li-O₂ battery.⁷⁸

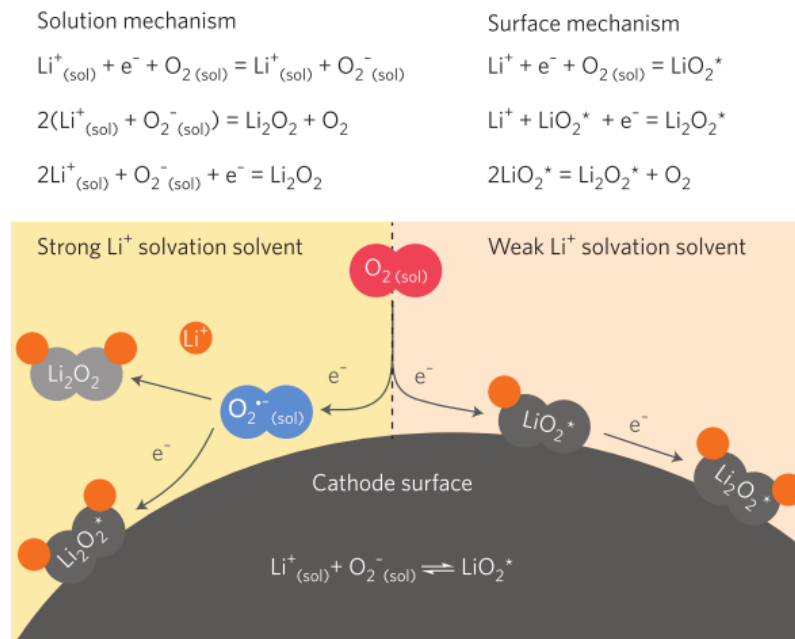
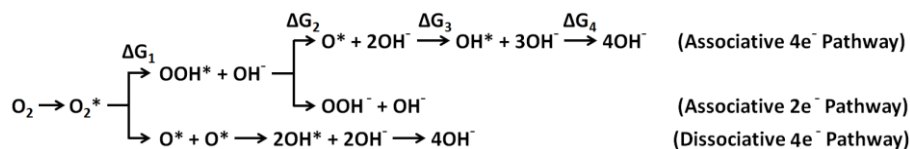


Figure 2-12. Reduction mechanism in a Li-O₂ cell at low overpotentials.⁷⁸

2.1.2 ORR / OER Mechanisms in Alkaline Electrolytes

The kinetics of ORR / OER is generally faster in an alkaline than in an acidic media, featured by a smaller over-potential and a higher exchange current, primarily due to the reduction of the thermodynamic barrier as the pH of electrolyte increases.^{26, 27} Such an advantage gives rise to the possibility of applying a wide range of non-noble metal or metal-free catalysts, even those with a relatively weak oxygen binding energy.^{28, 29} Taking ORR as an example, in order to achieve comparable activities, a relatively small amount of catalysts is generally required, e.g. in 0.1 M KOH than in 0.5 M H₂SO₄ or 0.1 M HClO₄,⁸⁴⁻⁸⁷ implying the development of noble metal alternatives is more feasible in an alkaline environment.

The ORR and OER processes are complicated multi-step reactions involving a total of four-electron transfer.⁸⁸ Note that OER is essentially a reverse process of ORR, the following discussion of reaction pathway will mainly focus on ORR. **Scheme 2-1** shows the ORR pathway in alkaline electrolytes.²¹ The dissociative pathway, also known as parallel pathway, involves a dissociation of oxygen and its subsequent reduction to water; while the associative pathway, or the series pathway, involves the formation of peroxide (OOH*), which can be either a final product (OOH⁻) or an intermediate leading also to water.⁸⁹ The dissociative pathway requires a cleavage of O=O bond at the initial stage and can only occur on a few metal surfaces at ambient conditions, such as Pt, Pd and Ag. Most other catalysts including carbon tend to reduce oxygen via an associative pathway. The difference lies in that carbon is poor at reducing the intermediate peroxide, while other metals such as Fe- or Co-based catalysts also show good activity towards peroxide reduction.⁸⁸



Scheme 2-1. ORR reaction pathways in alkaline electrolytes.²¹

Computational simulations of ORR / OER activity are based on the associative pathway.

It has been proposed that the over-potentials of ORR and OER are related to the strength of binding with different reaction intermediates on the catalysts surface (OOH*, O* and OH*) and the potential limiting step of ORR or OER is controlled by the unit step requiring the minimum or maximum reaction energy.⁹⁰ The ideal electrocatalysts need no driving force to catalyse the reactions, which means all the reaction energies are exactly equal to 1.23 V as the equilibrium potential for OER / ORR.⁹¹ Such ‘reversible’ catalysts with negligible overpotentials may exist in a two-electron transfer reaction involving one single intermediate, such as hydrogen evolution and oxidation reaction (HER / HOR).⁹² The ideal catalysts satisfy the Sabatier principle to bind the intermediate neither too weakly (no reaction) nor too strongly (catalysts poisoning), **Figure 2-13.**⁹³⁻⁹⁵

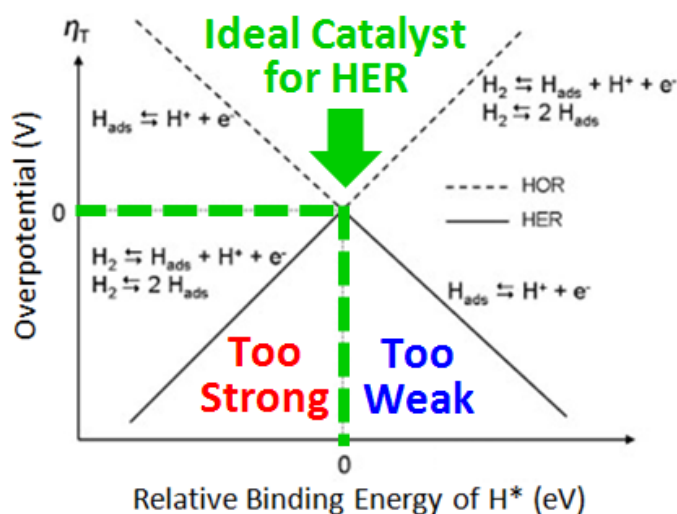


Figure 2-13. Activity volcano for HER with respect to the binding strength of H^* .⁹²

However, for multi-electron transfer reactions such as ORR and OER, large ‘thermodynamic’ overpotentials (e.g. top of activity volcano far from the equilibrium potentials) can hardly be avoided.⁹¹ Such catalytic irreversibility is owing to the scaling relationship between the adsorption energies of different reaction intermediates that bind to catalytic surfaces via similar atoms.⁹⁶ It has been noted that for ORR and OER in alkaline electrolytes, the binding energy of OOH* and OH* are inter-dependent, with a gap of ca. 3.0-3.4 eV regardless of the binding energy of O*.^{13, 94, 96} Hence, the minimum reaction potential for the second or third elementary step in OER ($\text{OH}^* + \text{OH}^- \rightarrow \text{O}^* + \text{e}^- + \text{H}_2\text{O}$ or $\text{O}^* + \text{OH}^- \rightarrow \text{OOH}^* + \text{e}^-$) is at least 1.5 – 1.7 V vs. RHE, while the maximum reaction potential of the first or the fourth elementary step in ORR ($\text{O}_2^* + \text{e}^- + \text{H}_2\text{O} \rightarrow \text{OOH}^* + \text{OH}^-$ or $\text{OH}^* + \text{e}^- \rightarrow \text{OH}^-$) is at most 0.76 – 0.96 V vs. RHE, leading to a ‘thermodynamic over-potential’ of at least 270 – 470 mV for ORR and OER in most cases (**Figure 2-14**). The ‘scaling relation’ between *OH and *OOH explains the origin of sluggish kinetics for ORR / OER, compared with HER / HOR, and also indicates that one single catalytic site can hardly be active for both ORR and OER.⁹⁷

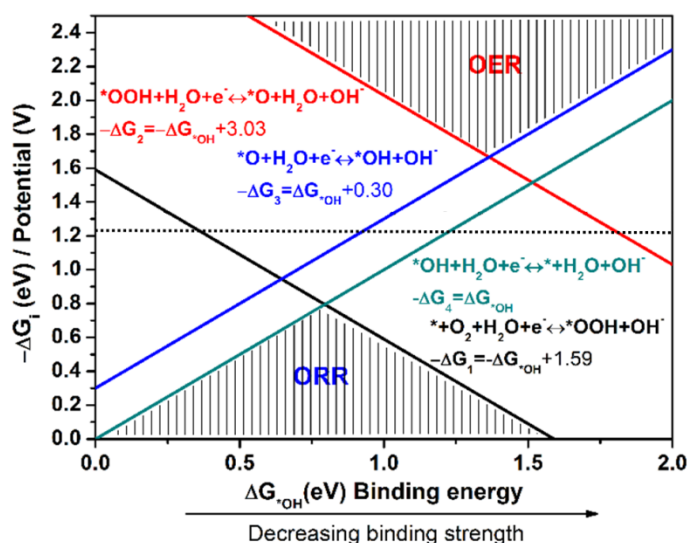


Figure 2-14. ORR / OER activity volcano for nitrogen-doped carbon based materials.¹³

2.2 Electrocatalysts for ORR and OER

The commercial noble-metal based ORR / OER electrocatalysts suffer from cost and durability issues, and only exhibit either ORR or OER activity rather than both. In order to reduce the amount of noble metal catalysts used in fuel cells and metal air batteries and furthermore the overall cost of the ECS devices without comprising their electrochemical performance, two major paths have been considered: e.g. for ORR, (1) to alloy Pt with transition metals; or (2) replace Pt based materials with low-cost non-precious metal / metal-free catalysts. Note that the active sites for ORR / OER are generally different as explained in **Section 2.1.2**, the overview of the state-of-the-art electrocatalysts in this chapter will accordingly be divided into two separate sections, **Section 2.2.1** for ORR and **Section 2.2.2** for OER, respectively. In each section, the noble metal, non-precious metal and metal-free catalysts will all be covered.

2.2.1 ORR Catalysts

2.2.1.1 Pt Alloys

In order to reduce the amount of Pt used in fuel cells, and also to further enhance the intrinsic activity of Pt catalysts, alloying Pt with some secondary metals have been one of the main research focuses over the last decades.⁹⁸ Typically, Pt alloys are composed of a Pt over-layer and a core of Pt alloyed with a less noble late transition 3d metal.⁹⁹ The Pt over-layer provides kinetic stability against the dissolution of the less noble solute component. At the same time, the electronic structure of the Pt surface is modified by the underlying alloy, resulting in improved ORR activity.⁹⁹⁻¹⁰⁴ The activities of Pt-alloy based NPs depend on both the composition and structure (ordering and

morphology) and their interactions. A wide variety of transition metals (Ni, Fe, Co, Y, *etc.*) has been incorporated into the Pt skeleton by carefully designed solution-based synthesis leading to uniformly shaped nanoparticles, **Figure 2-15**.¹⁰⁵⁻¹¹³

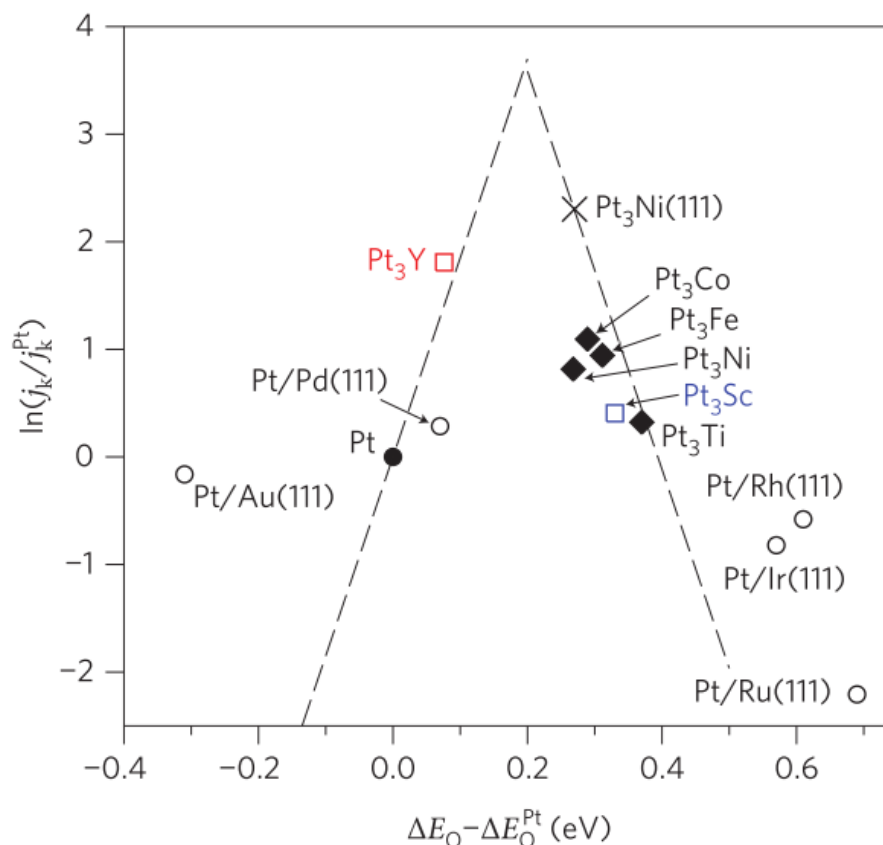


Figure 2-15. Activity volcano for Pt-alloy ORR catalysts: measured kinetic current density with respect to the calculated oxygen adsorption energy.¹⁰⁵

In addition to expanding the variation of compositions, the architectural studies of Pt alloys have also been proposed to preferably expose the most electro-catalytically active facets and sites. The primary approach is controllable tuning the surface composition to optimize the whole alloy's activity.¹¹⁴ In 2007, Stamenkovic et al. reported exceptionally high catalytic ORR reactivity for a thermally annealed Pt₃Ni alloy surface with a well-defined (111) orientation.¹¹⁵ Since then, the race towards the most

catalytically active shapes with exclusive exposure of (111)-oriented surface facets has significantly boosted the ORR activity of Pt-alloy catalysts.^{106, 116-124} The current record performance was achieved by molybdenum-doped Pt-Ni nanooctahedra with about 8-nm edge length which possessed mass activity almost 70 times higher than those of benchmark Pt catalysts proposed in 2010, **Figure 2-16**.¹¹⁴

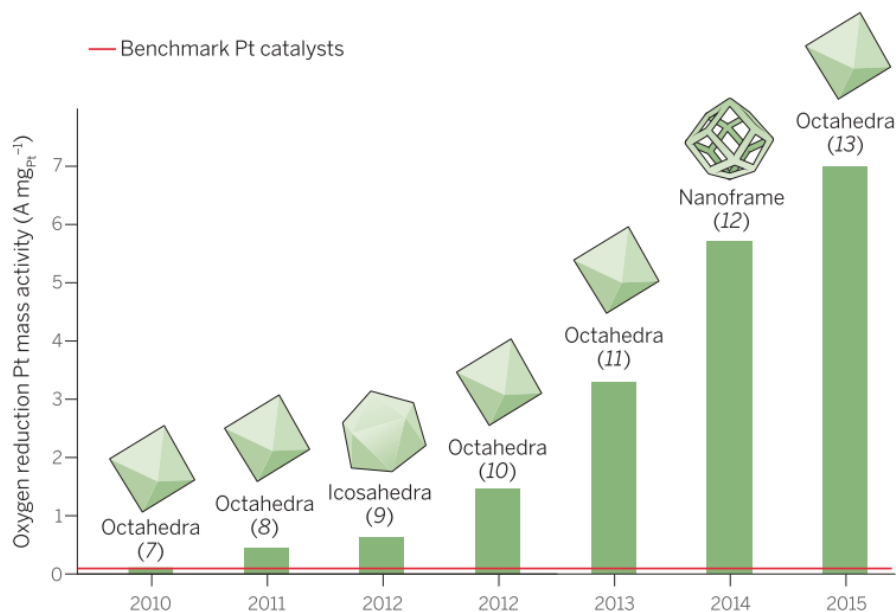


Figure 2-16. Ever rising ORR activity of Pt-Ni alloy catalysts with (111) facets.¹¹⁴

2.2.1.2 Non-Precious Metals

The most promising non-precious metal catalysts are transition metal-nitrogen-carbon (MeNC) based, which can be divided into metal-N₄ organometallic complexes (MeN_xC moieties) and metals coupled with nitrogen-containing carbon materials (Me-N-C coupled interface), **Figure 2-15**.^{125, 126} Jasinski et al. first reported the ORR activity of unsupported cobalt phthalocyanines in 1964.¹²⁷ The Me-N₄-containing macrocycles adsorbed on different carbon substrates also exhibited catalytic activity for ORR.¹²⁸⁻¹³⁰ In the 1970s, it was discovered that the stability and the activity of ORR catalysts could be

significantly improved by heating the Me-N₄-containing macrocycle / carbon composites to elevated temperatures in an inert atmosphere.¹³¹

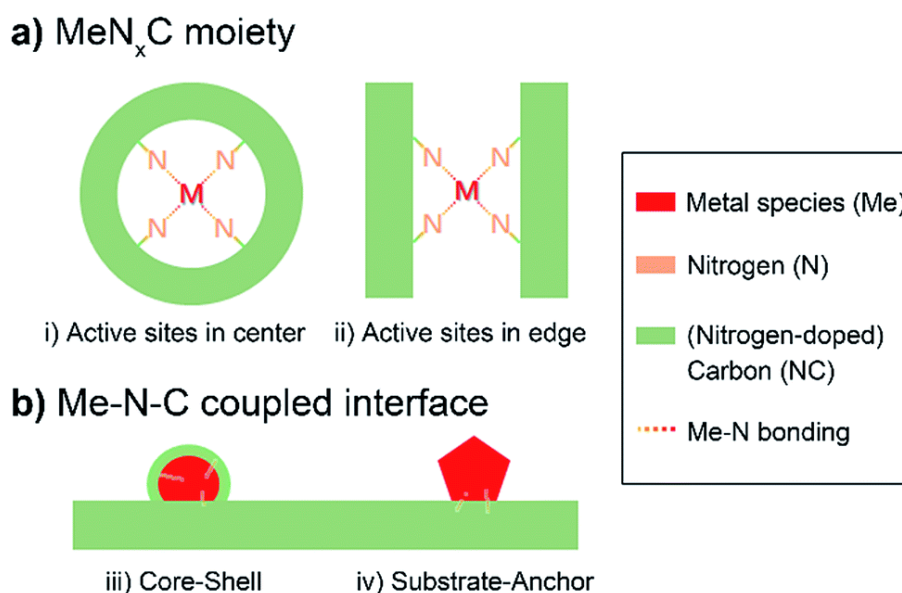


Figure 2-17. Schematic representation of two kinds of MeNC catalysts: (a) MeN_xC moieties, and (b) Me-N-C coupled interface.¹²⁵

In the late 1980s, Yeager et al. reported the ORR activity of carbonized polyacrylonitrile (PAN) mixed with iron or cobalt salts, which were adsorbed on different carbon substrates before heat treatment.¹³² This was an important result because it illustrated that the metal and nitrogen could come from different precursors and N₄-metal-containing macrocycles are not necessarily needed. It was believed that, for this combination of precursors, nitrogen atoms acted as binding sites for transition metal atoms, which led to the retention of nitrogen during pyrolysis.¹²⁶

In a very different approach, Dodelet et al. used a gaseous nitrogen precursor (acetonitrile), which was added to the carbon support and iron source during pyrolysis using acetonitrile in argon as carrier gas.¹³³ In this work, polyvinylferrocene was

adsorbed on carbon black and the mixture was pyrolyzed at 1000 °C. The product was catalytically active for the reduction of oxygen, when the iron precursor and nitrogen precursor were brought in contact during pyrolysis.¹³³ Catalyst materials prepared without any source of Fe or nitrogen source gave no catalytic activity for ORR, indicating the necessary role of Me-N interaction to the ORR activity. The same research group has also prepared very active ORR catalysts by pyrolyzing Fe acetate or Fe porphyrin precursors on carbon supports in H₂ / NH₃ / Ar atmosphere at 400-1000 °C.¹³⁴ Similar synthetic methods, using Co acetate or Co porphyrin precursors, have also been used to prepare ORR-active, Co-based electrocatalysts.^{135, 136}

The 'real' catalytic sites in MeNC catalysts are still not clear. Although a wide range of synthesis routes have been proposed and a variety of active sites have been claimed, all the top-performing MeNC materials demonstrated similar activity and thus the same active sites – in alkaline electrolytes, the performance of MeNC can be comparable or superior to noble metal catalysts; while in acidic media, the activity of MeNC are normally not as good as noble metals.¹²⁶

2.2.1.3 Metal-Free Materials

Besides being used as a support for metal catalysts, metal-free materials can also demonstrate considerable catalytic activity.¹³⁷⁻¹³⁹ The origin of their high activity may be the unique electronic structure for reactant / intermediate adsorption and variable nanostructure for enlarging the number of exposed active sites.^{13, 22} Note that pure carbons (nanostructured carbons, carbon nanotubes, and graphene sheets) generally

show negligible catalytic activities, doping non-metal heteroatoms such as N, B, S, O, and P into their frameworks can significantly enhance ORR activities by (1) changing the electronic character of the carbon and (2) creating rational defect structures to enable a stronger oxygen adsorption.^{23, 140}

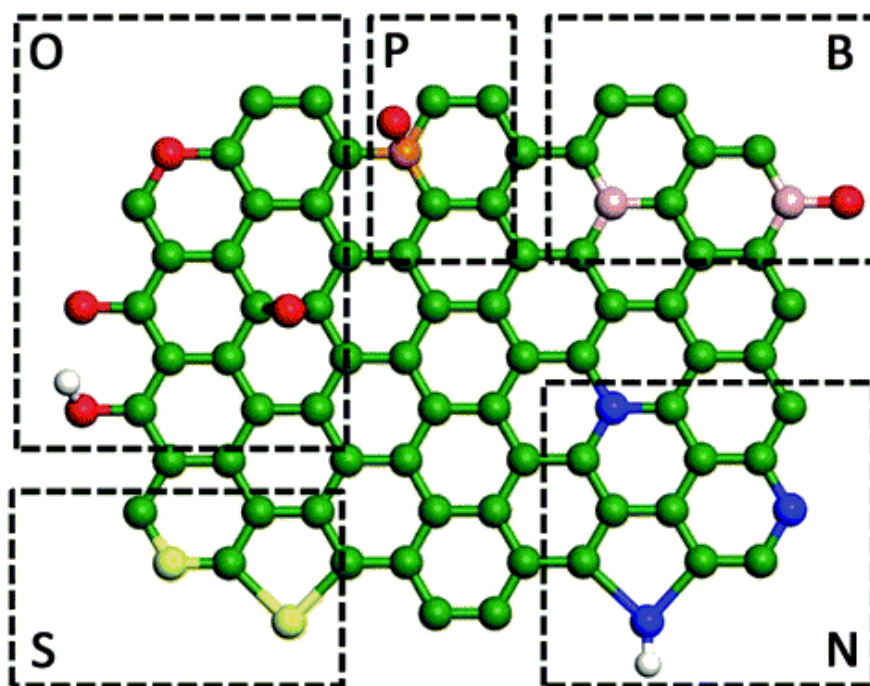


Figure 2-18. Typical atomic configuration of different types of dopants at different doping sites in the graphene matrix.⁹⁷

The ORR activity of heteroatom doped carbon is strongly dependent on the specific doping site and content of heteroatoms, which can be carefully controlled by designed doping procedure and precursor choice (**Figure 2-18**).⁹⁷ Among all heteroatoms, nitrogen doped CNT and graphene are most widely studied due to their easier synthesis and relatively good performance.²² Generally, there are three types of nitrogen species in carbon matrix (i.e. pyridinic, pyrrolic, graphitic N) depending on their different positions and bonding configurations; the mechanism of different nitrogen functions

toward ORR has recently been revealed by theoretical studies.²¹ Beyond single doped graphene, double or triple-doped graphene (e.g. B/N,^{141, 142} S/N,¹⁴³ P/N,¹⁴⁴ and N/B/P¹⁴⁵) show much higher ORR activity as compared to single-doped ones., which may be due to the inter-molecular synergistic catalysis as revealed by DFT calculations.¹⁴⁶

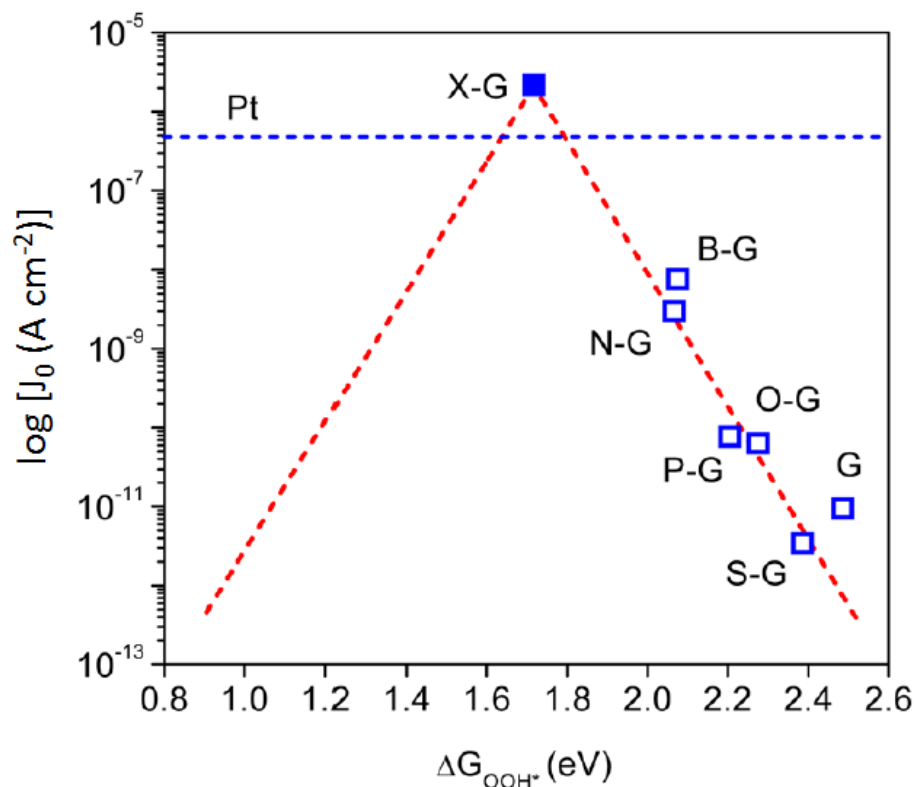


Figure 2-19. ORR activity volcano of heteroatom doped graphene with regard to the binding of OOH* intermediate. As predicted, the ORR activity of ideal doped graphene may surpass Pt.²¹

Although the experimental studies of ORR mechanism on metal-free materials are difficult, theoretical analysis indicates that dopant can tailor the electron-donor properties of nearby carbon atoms, which act as catalytic sites to enhance the adsorption of OOH* intermediate.^{21, 138} Extensive efforts have been undertaken to investigate the origin of ORR activity of graphene-based materials by performing systematic experiments and calculations.²¹ It was shown that among various doped

graphenes, N-graphene shows the lowest free energy change, indicating its possible highest ORR activity, which is consistent with many experimental results.²³ Recent studies combining the DFT calculations and electrochemical measurements showed that an ideal doped graphene material has a potential to surpass the ORR performance of the state-of-the-art Pt catalysts, **Figure 2-19**,^{13, 21, 22}

2.2.2 OER Catalysts

2.2.2.1 Precious Metals (Oxides)

The first studies of OER electrocatalysts date back to the 1960s and were devoted to single metals.¹⁴⁷ The experimentally established sequence of overpotentials for OER in acidic solutions is: Ru < Ir < Pd < Rh < Pt. However, single metals tend to be oxidised at high potentials, forming metal oxide film on the surface during OER process.¹⁴⁸ Consequently, metal oxide with the highest OER activity is rutile-type ruthenium oxide (r-RuO₂) in both acidic and alkaline solutions (**Figure 2-20**).¹⁴⁹

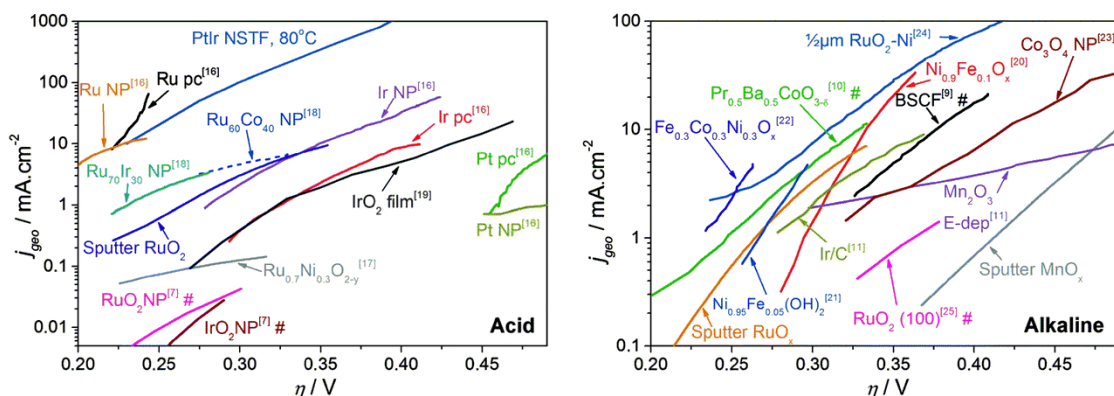


Figure 2-20. Overview of the state-of-the-art electrocatalysts for OER in either acidic or alkaline solutions.¹⁴⁹

A major drawback of the most active RuO_2 is its weak stability under acidic conditions in the case of commercial water electrolysis. During oxygen evolution under high potentials, i.e. > 1.4 V vs. RHE, it can be further oxidized to ruthenium tetroxide (RuO_4) while the latter is dissolvable.¹⁵⁰ As a result, the surface of RuO_2 is irreversibly changed and its high activity is vanished. An alternative to RuO_2 is iridium oxide (IrO_2) that possesses only a slightly higher overpotential but significantly enhanced OER stability for up to 2.0 V vs. RHE.¹⁴⁸

2.2.2.2 Non-Precious Metals

Non-precious metals (NPM) OER catalysts, mainly of transition metals and their oxides / oxy-hydroxides, are only stable in alkaline electrolytes. The firstly studied and still popular NPM electrocatalysts are Ni- and Co-based oxides, although their activities are not comparable to precious IrO_x (**Figure 2-21**).¹⁵¹⁻¹⁵³ Multimetal oxides / oxy-hydroxides based on Fe, Co and Ni show an improved activity to the corresponding single-metal oxides.¹⁵⁴⁻¹⁵⁸ Very recently, a FeCoW oxy-hydroxide with near optimal binding energy has been developed, which exhibits the lowest overpotential of 230 mV reported at 10 mA cm^{-2} in alkaline electrolytes.¹⁵⁹

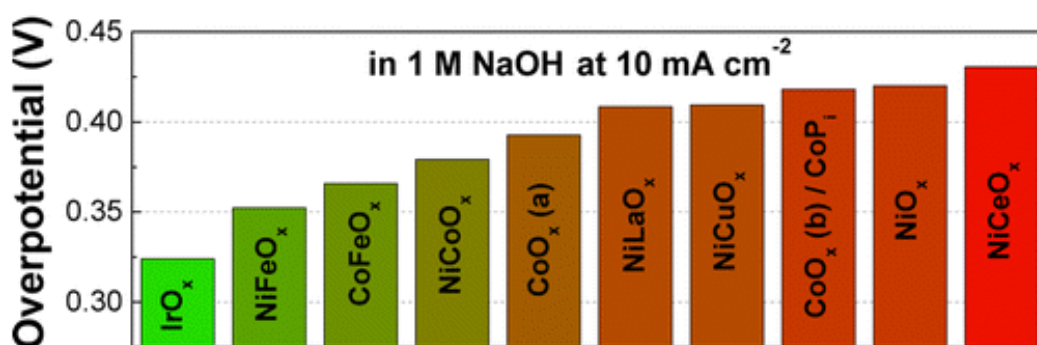


Figure 2-21. Overpotentials of NPM OER catalysts at 10 mA cm^{-2} in alkaline electrolytes.¹⁵¹

2.2.2.3 Metal-Free Materials

Different from the case of ORR, for which metal-free (MF) catalysts have been widely investigated and shown to be competitive, the studies of non-metal materials for OER have just begun. The theoretical studies of OER on carbon surfaces regarding oxygen / hydroxide adsorption behaviour and mechanism are very rare..^{10, 22, 160, 161} Although high-surface-area porous MF catalysts may demonstrate high OER current, their intrinsic activity (i.e. roughness factor / electrochemical surface area corrected current density) and turnover frequency (TOF) are still worse than metal catalysts, let alone the suspicious long-term stability against carbon oxidation at high potentials.⁹⁷

2.3 Brief Overview of Graphene

Although graphene or single atomic plane of graphite has been theoretically studied for more than sixty years¹⁶² and has been widely used to describe the properties of various carbon-based materials,¹⁶³ it was generally regarded as an integral part of three-dimensional (3D) materials and free-standing (sufficiently isolated from its environment) graphene was presumed not to exist¹⁶⁴ until the unexpected discovery in 2004.¹⁶⁵ Following the initial investigations on its physical property, the Call from Ruoff in 2008 largely expanded the research focus from its electronic properties to other applications including electrocatalysis.¹⁶⁶ Stable chemical converted graphene (CCG) dispersion in various solvents opens the gate to modify / tune the chemical properties of graphene, facilitating the formation of either graphene derivatives or graphene supported composites.¹⁶⁷ Moreover, the low cost and easy synthesis of graphite oxide

(GO, the precursor of CCG) make mass production of graphene-based materials potentially feasible.¹⁶⁸ In this chapter, the property (**Section 2.3.1**) and synthesis route (**Section 2.3.2**) of graphene based materials will be summarized.

2.3.1 Properties of Graphene

In addition to the unique electronic properties of graphene that have been comprehensively investigated during the first five years after its discovery,¹⁶⁹ graphene also demonstrates large theoretical specific surface area ($> 2500 \text{ m}^2 \text{ g}^{-1}$),¹⁷⁰ high electrical conductivity (less than Ag),¹⁷¹ excellent thermal conductivity (about 100 times of Cu),¹⁷² and strong mechanical strength (strongest ever measured).¹⁷³ In fact, it is speculated that in many applications graphene will out-perform CNTs, graphite, metals and semiconductors where it is used as an individual material or as a component in a hybrid or composite material.^{174, 175}

2.3.2 Synthesis of Graphene

All different graphene synthesis methods can be generally classified as either a bottom-up or a top-down approach: the former involves the direct formation of graphene from carbon sources, while the latter is to split graphite or its derivatives.¹⁶⁹

Chemical vapour deposition (CVD), one of the most common bottom-up approaches for graphene synthesis, is typically used to grow large-area, single or few-layer graphene sheets. Ni and Cu catalysts represent two types of growth mechanisms due to their different solubility of carbon.¹⁷⁶⁻¹⁷⁸ For those catalysts with a high solubility of carbon

such as Ni, the hydrocarbon compound cracks at high temperatures to form carbon species, which dissolve in the metal; upon cooling, the carbon species precipitate out from the surface of the metal followed by nucleation and growth to form graphene. This is called 'carbon segregation and/or precipitation' mechanism where the number of graphene layers is strongly dependent on the cooling rate.¹⁷⁷ For catalysts with low solubility of carbon such as Cu, graphene synthesis obeys the 'surface growth' mechanism. Instead of diffusing into the metal matrix, a carbon precursor firstly adsorbs on the surface of the catalyst, and then nucleates and grows to form a graphene island, and finally graphene by continuous growth.¹⁷⁸ Other bottom-up approaches include plasma enhanced CVD (PECVD), which allows the growth of single-layer graphene at shorter reaction time and lower temperature compared to the normal CVD.¹⁷⁹ Graphitization of carbon-containing substrates, such as SiC, through the high temperature annealing can give rise to single-layer and few-layer graphene films as well.^{180, 181} In addition to the above methods based on the solid-phase deposition, graphene could also be produced via a wet chemical reaction of ethanol and sodium followed by pyrolysis,¹⁸² or through organic synthesis to give graphene-like polyaromatic hydrocarbons.^{183, 184}

The first isolation of graphene was obtained by mechanical cleavage of bulk graphite – repeatedly peeling graphite with a scotch tape until the thinnest layer was found.¹⁶⁵ Although labour intensive and extremely low-yield, such a method can provide high-quality graphene crystallites up to several hundred micron in size, which is sufficient for most research purposes (especially in physics).¹⁶³ Instead of cleaving graphite manually, ultrasonic¹⁸⁵ or electrochemical exfoliation¹⁸⁶ has been explored,

which can lead to stable suspension of exfoliated graphene in a variety of solution. Using chemically 'loosened' graphite as starting materials can further facilitate the aforementioned sonication process,¹⁸⁷ of which the most commonly used are GO¹⁶⁸ and various intercalated graphite^{188, 189} (i.e. alkali metal graphite intercalation compound). It is worthwhile to emphasize GO here, which features easy synthesis, high yield, low cost, and reasonably good dispersibility in a variety of solvents (i.e. up to 2-10 mg cm⁻² in water), thus particularly suitable for both laboratorial and industrial application.¹⁶⁸

Chapter 3. Experimental

3.1 Synthesis

3.1.1 Intercalated Graphene / Graphitic Carbon Nitride¹⁹¹

Graphite oxide (GO) was synthesized by a modified Hummer method.¹⁹⁰ In a typical experiment, 5 g graphite (< 20 micron, Sigma-Aldrich) was vigorously stirred with 115 ml concentrated sulphuric acid (95-97%, Merck KGaA) in an ice bath (0 °C) and 15 g potassium permanganate (99+%, Sigma-Aldrich) was slowly added in to prevent a rapid temperature increase. The mixture was stirred in the ice bath for 30 minutes. After that the mixture was moved to an oil bath (30 °C) and was further stirred for 2 hours. Then 115 ml deionised (DI) water (18.2 MΩ, Barnstead Easypure RoDi) was slowly added in, during which the temperature of the mixture may rise to ~40-45 °C. The diluted mixture was kept stirring at that temperature for another 30 minutes. Subsequently, 700 ml DI water was added into the mixture followed by 50 ml hydrogen peroxide aqueous solution (30 wt%, Sigma-Aldrich). The mixture was left overnight before being washed with 6-7 L DI water with centrifuge (Heraeus Biofuge Primo). When the pH value of the drained water was 7, the GO obtained was freeze-dried (Virtis BT2KES) for about a week before further use. **[Note that the explosive manganese(VII) heptoxide, Mn₂O₇, can be produced during the synthesis of graphite oxide, it is important to add permanganate slowly and control the temperature below 50 °C. The stirring should be kept fast but without splashing. Using a larger reactor, i.e. 1 L conical**

flask is helpful. Wearing goggles and gloves are necessary.]

Graphitic carbon nitride (GCN) was synthesized by the polymerization of cyanamide.¹⁹²

In a typical experiment, cyanamide powder (99%, Sigma-Aldrich) was directly heated at 550 °C for 4 hours under nitrogen, with a ramping of 2.2 °C min⁻¹.

Graphene / graphitic carbon nitride intercalated composites (GSGCN) were synthesized by wet chemical mixing of GO and cyanamide (GCN precursor) followed by thermal annealing. In a typical experiment, desirable amount of cyanamide aqueous solution (50 wt%, Sigma-Aldrich) were added in 100 ml GO suspension (1 mg ml⁻¹). The mixture was sonicated for 1 hour till there was no visible precipitate. After that, the sample was dried in a vacuum oven (80 °C) overnight. The grey / black powder obtained was then ground and transferred into a crucible with lid. For thermal annealing, the heating programme was the same as that for the synthesis of GCN – the sample was annealed at 550 °C for 4 hours under nitrogen, with a ramping rate of 2.2 °C min⁻¹. The GS/GCN composites were labelled based on the mass ratio of cyanamide and GO, e.g. 100, 150, 200, 250, and 300 mg cyanamide was mixed with 100 mg GO, the GS/GCN composites obtained were marked as GSGCN_1x, GSGCN_1.5x, GSGCN_2x, GSGCN_2.5x and GSGCN_3x, respectively.

Hierarchically porous graphene / graphitic carbon nitride intercalated composites (hp-GSGCN_2x) were synthesized via the same fabrication procedure as GSGCN_2x, but an extra 5 ml colloidal silica solution (40 wt% suspension in water, Sigma-Aldrich) was added to the mixture of cyanamide and GO before sonication. After being annealed at 550 °C, the material obtained was washed with 10 g ammonium bifluoride (95%, Sigma-Aldrich) for 24 hours to remove the silica templates, followed by three rounds of

filtration and washing with 1 L DI water and 0.5 L ethanol (100%, Merck KGaA). The hp-GSGCN_2x obtained was dried in vacuum oven (80°C) overnight before characterisation and evaluation.

3.1.2 Maghemite Embedded Nitrogen Doped Graphene Framework¹⁹³

Graphene oxide aqueous solution (2 mg ml⁻¹) was achieved by continuous probe sonication (Hielscher UP400) of a mixture of 1 g graphite oxide (GO, detailed synthesis was described in **Section 3.1.1**) and 500 ml DI H₂O for 24 hours, followed by centrifugation (Heraeus Biofuge Primo) at 8000 RPM (revolution per minute) for 30 min to remove any trace amount of unexfoliated GO.

Hierarchically porous nitrogen-doped graphene framework, and confinement of maghemite nanoparticles, was achieved via a hydrothermal reaction. The overall approach for was a one-pot process, using the graphene oxide aqueous solution, cyanamide and iron(III) chloride as precursors for the framework, the N-doping and the maghemite nanoparticles, respectively, which was followed by freeze drying and further thermal treatment. An un-doped control samples (GF_800) was first synthesized using 15 ml graphene oxide aqueous solution (2 mg ml⁻¹) without any other nitrogen or iron precursor. For optimization of N-doping, to the same amount graphene oxide solution was added an aqueous cyanamide solution (50 wt%) of 120, 240 or 600 µl; hereafter named with a suffix, N1, N2 or N5, respectively. Finally the optimized composition from the above was used for further addition of iron(III) chloride hexahydrate, FeCl₃·6H₂O, of 0.05, 0.15 or 0.25 mmol (13.5, 40.5 or 67.5 mg; hereafter named with a suffix, Fe1, Fe3

or Fe₅, respectively). In all the cases, the mixtures of graphene oxide solution and/or cyanamide solution and/or iron(III) chloride hexahydrate were sonicated for 30 minutes before being moved into the Teflon-lined stainless steel autoclave for hydrothermal reaction at 180 °C for 12 hours. The hydrogels formed were freeze-dried for 24 hours and then were thermally annealed at 800 °C for 1 hour under flowing nitrogen (ramping rate was 3 °C min⁻¹). The samples obtained were thus named as GF+N_x+Fe_y_800 (values of x and y denote the ratios of the relevant precursors mentioned above). To understand the origin of porosity for the developed substrate, a doped graphene framework without high temperature thermal treatment was also prepared for comparison, and was named as GF+N_x.

3.1.3 Phosphorus / Nitrogen Co-Doped Graphene Framework

Phosphorus and nitrogen co-doped graphene frameworks (PNGF) are prepared via a one-pot hydrothermal reaction using graphene oxide (detailed synthesis of graphene oxide was described in **Sections 3.1.1 and 3.1.2**) as the carbon sources, and diammonium phosphate (DAP) or ammonium dihydrogen phosphate (ADP) as the single phosphorus and nitrogen precursors, and / or cyanamide solution (CA, 50 wt%) as an extra nitrogen precursor, followed by freeze-drying and / or high-temperature calcinations. The samples achieved have been named as PNGF_DAP, PNGF_ADAP, PNGF_ADAP(op), PNGF(op), according to their corresponding synthesis conditions. More specifically, in order to form PNGF_DAP or PNGF_ADAP, 396 mg DAP (3 mmol) or 345 mg ADP (3 mmol) was added into 15 ml graphene oxide (2 mg ml⁻²) and mixture was sonicated for 30 min before being moved into a Teflon-lined stainless steel autoclave for hydrothermal reaction at 180 °C for 12 h. The hydrogel formed was freeze-dried for 24 h. The thermal annealing to achieve PNGF_DAP_800 was conducted at 800 °C for 1 h under flowing nitrogen (ramping rate was 3 °C min⁻¹). The

PNGF_AD_P(op) was synthesized via a similar route as PNGF_AD_P but using a smaller amount of AD_P (132 mg, 1 mmol). The PNGF(op) was synthesized via a similar route as PNGF_AD_P(op) but adding CA (240 μ l) as an extra nitrogen precursor in the hydrothermal reaction.

3.2 Physical Characterisation

The morphology and microstructure of the samples were investigated by scanning electron microscope, transmission electron microscopy (JEOL 2100, Japan) and X-ray diffraction (STOE Stadi P). Nitrogen sorption isotherms and BET surface areas were measured at 77 K with Quantachrome Autosorb iQ-c.

The chemical composition was analysed by X-ray photoelectron spectroscopy (Thermo Scientific K-Alpha, UK), Raman spectroscopy (Renishaw), Fourier transform infrared spectroscopy (Thermo Scientific Nicolet iS10), and thermogravimetric analysis (Setaram Setsys 16/18). Electrical conductivity was measured by the four-probe technique (Jandel RM3) with the pressed pellet of materials as samples.

3.3 Electrochemical Characterisation

The electrochemical performance of the synthesized catalysts was mainly measured in the O₂-saturated 0.1 M KOH aqueous electrolyte. Oxygen was purged for 30 min before measurement, and continuously bubbled through the electrolyte during the tests, in order to ensure the saturation of O₂ in the electrolyte. Rotating disk electrode (RDE, glass carbon tip, Metrohm) or rotating ring disk electrode (RRDE, Pt-ring / glassy carbon

disk, Gamry) was used as the working electrode, Ag/AgCl (sat. KCl, Metrohm) was used as the reference electrode, and a platinum sheet (Metrohm) was used as the counter electrode. The scan rates for cyclic and rotating voltammetry were 100 and 10 mV s⁻¹, respectively, and ring potential was constant at 0.5 V vs. Ag/AgCl for rotating voltammetry. All the results were recorded using Metrohm Autolab 302N or Metrohm Multi Autolab. In some results, the measured potentials were converted with reference to the reversible hydrogen electrode (RHE) using the equation $E_{\text{RHE}} = E_{\text{Ag/AgCl}} + 0.0591 \times \text{pH} + 0.197$. The commercial platinum on carbon black (20 wt% Pt loading, Alfa Aesar) and iridium on Vulcan (20 wt% Ir loading, Fuel Cell Store) were used as reference samples for ORR and OER, respectively.

For preparation of the RDE working electrode, 4 mg catalyst and 40 μl Nafion solution (5 wt%) were added in 3 ml de-ionized water, followed by sonication for 60 minutes to achieve uniform dispersion of the catalysts in the solvent. Catalyst suspension (5.4 μl) was drop-cast on the RDE tip (3 mm diameter) and dried at 60 °C. For RRDE working electrode preparation, 4 mg catalyst and 40 μl Nafion solution (5 wt%) were added into a mixture of 3 ml de-ionized water and 1 ml ethanol absolute; and 25 μl catalyst suspensions were then drop-cast on the RRDE tip electrode (5.61 mm diameter for GC). The catalyst loading is ca. 0.1 mg cm⁻² for all samples including commercial platinum loaded carbon and iridium on Vulcan.

For RDE measurement, the electron transfer number (ETN, n) was calculated based on the Koutecky–Levich (K-L) equation (**Equation 3-1**):

$$\frac{1}{J} = \frac{1}{J_L} + \frac{1}{J_K} = \frac{1}{0.62nFC_0D_0^{2/3}v^{-1/6}\omega^{1/2}} + \frac{1}{J_K} \quad \text{Eq. 3-1}$$

where J is the measured current density, J_L and J_K are the diffusion limiting and kinetic

current density (mA cm^{-2}), F is the Faraday constant ($96485 \text{ s A mol}^{-1}$), C_0 is the bulk concentration of dissolved O_2 in 0.1M KOH ($1.2 \times 10^{-3} \text{ mol L}^{-1}$), D_0 is the diffusion coefficient of O_2 in 0.1M KOH ($1.9 \times 10^{-5} \text{ cm}^2 \text{ s}^{-1}$), ν is the kinematic viscosity of the electrolyte ($0.01 \text{ cm}^2 \text{ s}^{-1}$), and ω is the angular velocity (rad s^{-1}).¹⁹¹

For RRDE, the ETN was determined through **Equation 3-2**:

$$n = 4 \times \frac{I_d}{I_d + I_r/N} \quad \text{Eq. 3-2}$$

$n = 4 - \frac{I_d}{I_d + I_r/N}$ where I_d and I_r are the measured current for disk and ring electrode, and N is current collection efficiency of the Pt ring (0.37).¹⁹³

For Tafel plot, the diffusion corrected kinetic current density (J_K) was calculated on the basis of the K-L equation (**Equation 3-3**):¹⁹³

$$J_K = \frac{J \times J_L}{J_L - J} \quad \text{Eq. 3-3}$$

Electrochemical impedance spectroscopy (EIS) measurements were conducted under 1600 RPM and at the potential under which the current density reaches 3 mA cm^{-2} . The frequency range is 1 MHz to 0.01 Hz. The amplitude is 10 mV.

Chrono-amperometry measurement for ORR or OER stability was conducted in O_2 -saturated 0.1M KOH for 20 hours under 1600 RPM and at the potential under which the ORR or OER current density reaches 3 or 10 mA cm^{-2} , respectively. The potential cycling for ORR / OER durability was conducted between 0.2 and 1.2 V vs. RHE for ORR or between 1.2 and 2 V vs. RHE for OER, respectively, using a scan rate of 100 mV s^{-1} for 5000 cycles.¹⁹⁴

Electrode evaluation was conducted in 0.1 and 6M O_2 -saturated KOH electrode. The electrodes were prepared by spray-coating the corresponding catalysts on carbon fibre paper gas diffusion layer (GDL, Ion Power). The loading ratio was 0.7 mg cm^{-2} .

Chapter 4. Intercalated Graphene / Graphitic Carbon Nitride

4.1 Introduction

Metal-free ORR electrocatalysts, such as nitrogen-doped carbon and its derivatives, have attracted considerable interest due to their comparable catalytic activity, reduced cost and improved durability, compared with the existing counterparts.¹³⁷ It is commonly accepted that introducing nitrogen into a carbon matrix is a key step to synthesize highly active metal-free ORR catalysts.¹³⁸ Despite the controversy on the exact role of nitrogen heteroatom in ORR, both quantum mechanical calculations^{175, 195, 196} and experimental observations¹⁹⁷⁻²⁰⁰ reveal that incorporation of nitrogen, especially the graphitic and/or pyridinic species, induces a positive charge on the adjacent carbon, which can facilitate oxygen adsorption and subsequently weaken the O=O bond in the adsorbed oxygen molecules. In this regard, graphitic carbon nitride (GCN) – stacked two dimensional (2D) heptazine (C₆N₇) sheets connected by tertiary amines – may serve as a promising metal-free ORR catalyst owing to its high nitrogen content (60.9 wt% in theory and mainly of pyridinic / graphitic nature) and stable molecule structure.²⁰¹⁻²⁰³

Unfortunately, the electrocatalytic activity of pristine GCN is restricted by its semi-conductive nature ($< 10^{-2}$ S cm⁻¹), which obstructs electron transfer during the ORR process.²⁰⁴ Thus introducing electron-conductive carbon materials as substrates should be a general strategy to improve the ORR performance of GCN. First-principle

studies on the ORR capability of GCN have shown that if sufficient electrons are available in the GCN-O₂ system, the ORR could occur via a direct four-electron (4e⁻) pathway, rather than the two-step two-electron (2e⁻) pathway for the pristine GCN.²⁰⁵ The first experimental attempt of carbon-supported GCN composites was to mechanically blend GCN with carbon black (CB).²⁰⁶ The GCB/CB composites showed much improved onset potential and reduction current density, compared with pristine GCN, as a result of the increased conductivity and surface area derived from carbon black support.²⁰⁶ To further clarify the role of substrates, ordered porous carbon materials, such as CMK-3, were then adopted as their morphology and structures were easy to control. It was shown incorporation of GCN into CMK-3 led to a direct 4e⁻ pathway, in accordance with the theoretical prediction.²⁰⁵ However, the small mesopores in CMK-3 may not be capable of fast mass exchange during ORR and the catalytic activity of GCN@CMK-3 was thus worse than that of the commercial Pt/C. From this point of view, uniform GCN embedded porous carbon (GCN/C) composites with tuneable pore size have been prepared.²⁰⁷ The ORR activity of macroporous GCN/C with pore size of 150 nm was shown superior to that of the mesoporous GCN/C with pore size of 12 nm obtained via the similar synthesis route. The macroporous GCN/C facilitated the oxygen diffusion, and led to a much smaller Tafel slope value in the high overpotential region than that of the mesoporous sample. However the overall electron transfer number for this macroporous composite was only three, indicating a combined 2e⁻ and 4e⁻ reaction pathway, which was probably due to the low specific surface area and the lack of exposed active sites.²⁰⁷ Up to now, none of the aforementioned carbon-supported GCN composites can show both fast ORR kinetics

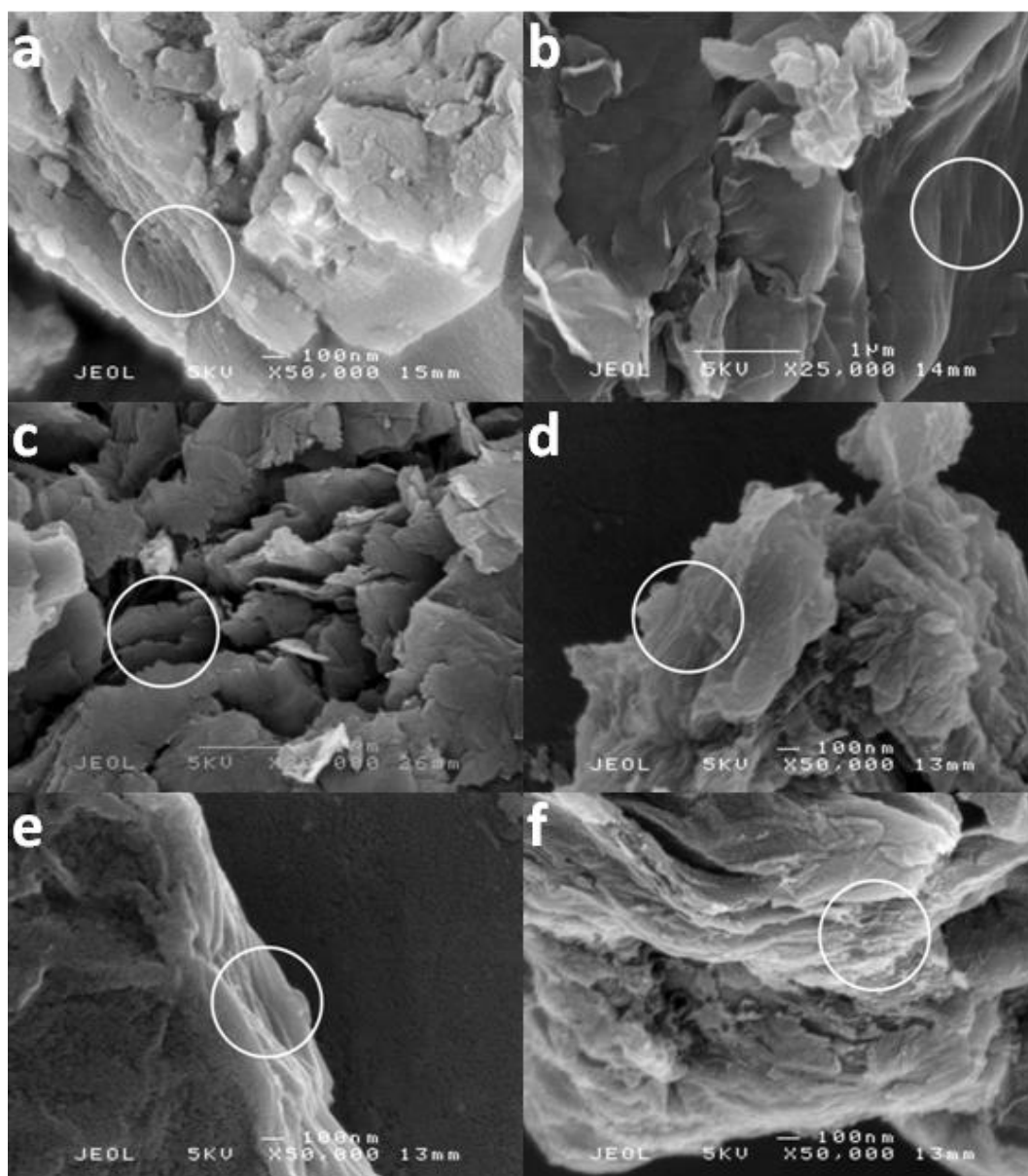
and excellent selectivity towards a $4e^-$ transfer pathway.

Compared with carbon-based supports, 2D graphene sheets (GS) are expected to be a better substrate, given the excellent electron collection and transport properties of GS and its structural similarity to GCN.²⁰⁸ One theoretical investigation demonstrated that the π - π interaction at the interface of hybrid GS/GCN composites could force electrons to transfer from GS to GCN and accumulate on the active sites in GCN, which was predicted to significantly enhance the ORR catalytic activity.²⁰⁹ However the early investigation of immobilizing GCN on GS only showed limited improvement – the ORR occurred via a $3e^-$ pathway with reduction current density slightly lower than that of the home-made platinum-loaded graphene composite.²⁰⁴ Such an improvement was below expectation because only the effect of conductivity was considered and the GCN loading ratio (amount of active materials) was low (ca. 10 wt% nitrogen). In addition, the layered morphology was unfavourable for ORR due to the limited active sites exposure and the inefficient mass transport and access.²⁰⁴

Inspired by that, here for the first time, I experimentally synthesized GS/GCN intercalated composites with hierarchical porosity. The ORR activity was first optimised by balancing two intrinsic parameters – active sites and conductivity. After further taking into account of mass transport, the hierarchically porous GS/GCN intercalated composites obtained showed fast reduction kinetics and 100% catalytic selectivity towards the four-electron transfer pathway, with better long-term stability and stronger tolerance against methanol than the commercial Pt/C catalysts. To the best of my knowledge, such excellent catalytic activities outperformed the other GCN-based ORR catalysts.^{204-207, 210}

4.2 Results and Discussion

The morphology of GS/GCN composites is first studied by scanning electron microscopy (SEM). It can be seen in **Figure 4-1** that all GS/GCN composites possess layered structures (as highlighted by the white circles), which are similar to that of pristine GCN (**Figure 4-1a**) and GS (**Figure 4-1b**). High resolution transmission electron microscopy (HRTEM) image of GS/GCN_2x in **Figure 4-1h** further confirms the above observation. The layered structure of GSGCN_2x is clearly shown from its cross sectional image and the inter-layer distance is calculated to be 0.33 nm (or 3.3 Å).



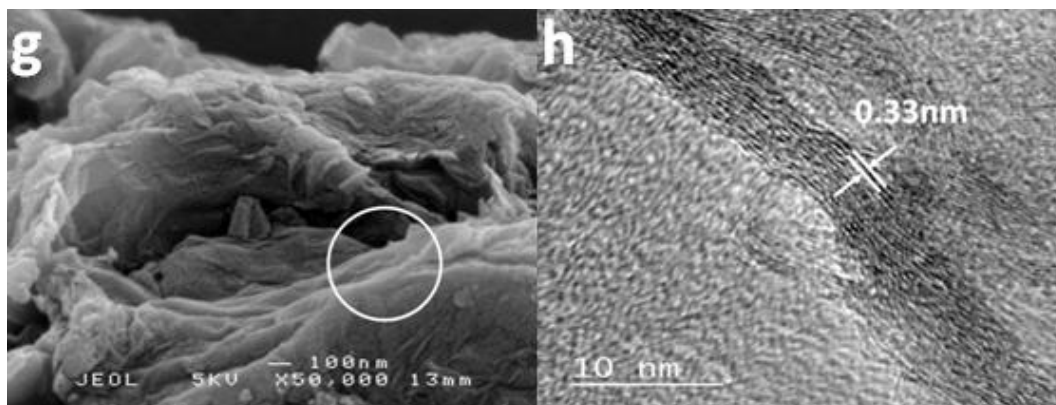


Figure 4-1. Electron microscope images of GCN, GS and GSGCN composites. SEM images of (a) GCN, (b) GS, (c) GSGCN_1x, (d) GSGCN_1.5x, (e) GSGCN_2x, (f) GSGCN_2.5x and (g) GSGCN_3x; and (h) HRTEM image of GSGCN_2x. White circles in (a-g) highlight the layered structures of GCN, GS, and GSGCN composites.

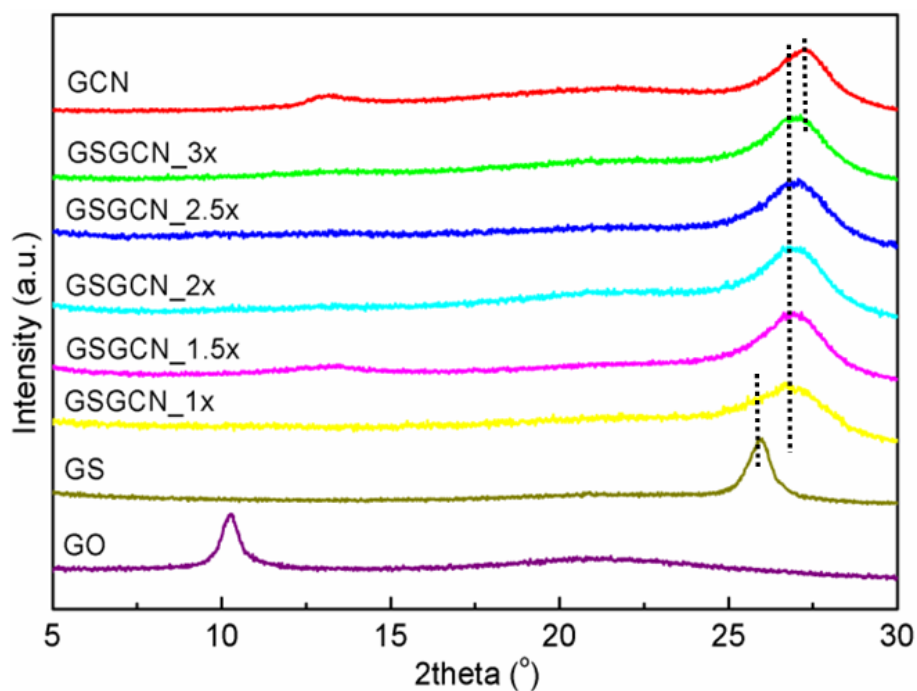


Figure 4-2. XRD of GO, GS, GCN and GS/GCN intercalated composites. Those three straight lines exhibit the difference in the peak positions of GS, GCN and GS/GCN composites.

It is displayed in the X-ray diffraction patterns (XRD, **Figure 4-2**) that graphite oxide (GO) possess an intensive diffraction peak round 10° , similar to the previous reports.¹⁹⁰ The

diffraction peak position indicates an interlayer distance of ~ 8.5 Å for GO, more than double the value for graphite powder (~ 3.3 Å),²⁰⁴ as a result of the oxygen functional groups between layers and the intercalated water. The peak positions of GS/GCN composites are at 26.9° , corresponding to an interlayer distance of 3.31 Å, which is in accordance with the value obtained from the HRTEM image shown above (**Figure 4-1h**). The interlayer distances for GS and GCN are 3.27 and 3.44 Å, according to the peak positions at 25.9° and 27.3° respectively. Note that the XRD peak positions of GS/GCN composites are between those of GS and GCN (highlighted by the straight lines in **Figure 4-2**). Hence, the change in the interlayer distance suggests successful intercalation of GS into GCN layers.²⁰⁴

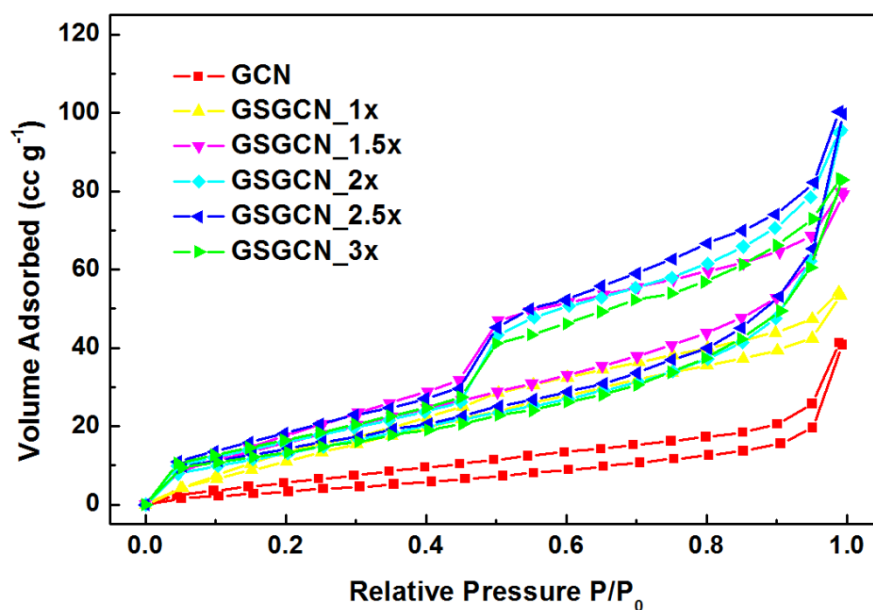


Figure 4-3. Nitrogen isotherms for GCN and GS/GCN intercalated composites at 77K.

Nitrogen isotherms at 77 K (**Figure 4-3**) are used to investigate the microstructures of GCN and GS/GCN intercalated composites. The Brunauer-Emmett-Teller specific surface area (BET SSA) of GS/GCN composites derived from the nitrogen isotherm are

within the range of 50-75 $\text{m}^2 \text{g}^{-1}$ (**Figure 4-4**), with a slight rise from GSGCN_1x to GSGCN_1.5x then drop as the GCN content in the composites further increases. The SSA of the intercalated GS/GCN composites is lower than the previously reported value for graphene-based materials^{170, 211, 212} due to the restacking of graphene sheets during the formation of intercalated layered structures. Nevertheless, the BET SSA of any GS/GCN composite is significant higher than that of GCN (ca. 15 $\text{m}^2 \text{g}^{-1}$).

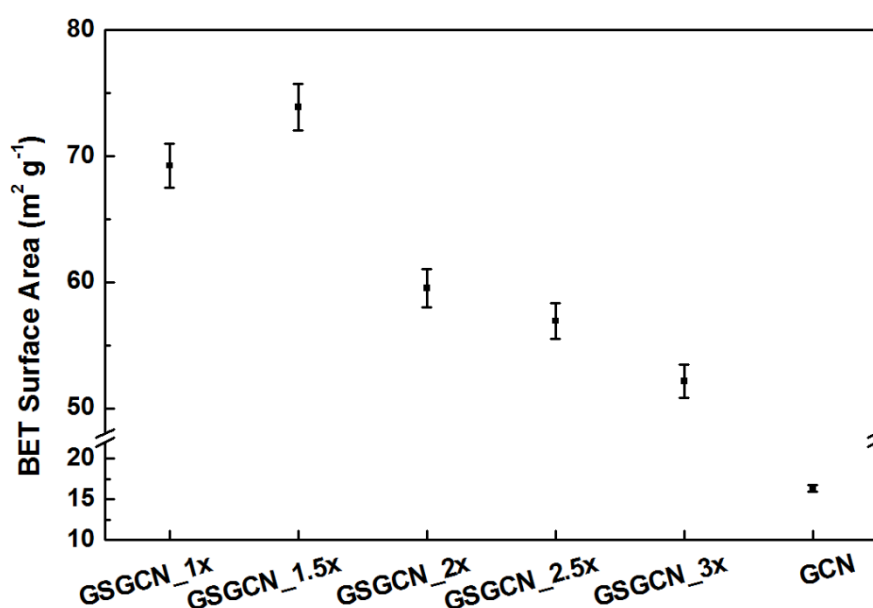


Figure 4-4. BET specific surface area of GCN and GS/GCN intercalated composites, derived from N₂ isotherms at 77 K (**Figure 4-3**).

Chemical constitutions of the intercalated GS/GCN composites are then examined by the Fourier transform infrared spectroscopy (FTIR). Results (**Figure 4-5**) show that the out-of-plane bending vibration characteristics of heptazine rings ($\sim 800 \text{ cm}^{-1}$, highlighted by the ellipse) for GCN are preserved in all GS/GCN intercalated composites, while the typical stretching vibration modes of heptazine-derived repeating units (~ 1200 - 1650

cm^{-1} , highlighted by the straight lines in the inserted small plot) appear in GSGCN_2x, GSGCN_2.5x and GSGCN_3x but are not evident in GSGCN_1x and GSGCN_1.5x, implying either an incomplete polymerization or partial decomposition of GCN component for the latter two composites.²¹³⁻²¹⁶ What's more, it is noticed that GO has been successfully reduced to GS via thermal annealing as the non- sp^2 carbon bonds (i.e. C-O, C=O and O-C=O) of GO significantly diminish in all GS/GCN composites²¹⁷ (highlighted by the straight lines in the main plot), which could be further supported by the X-ray photoelectron spectroscopy (XPS) results.

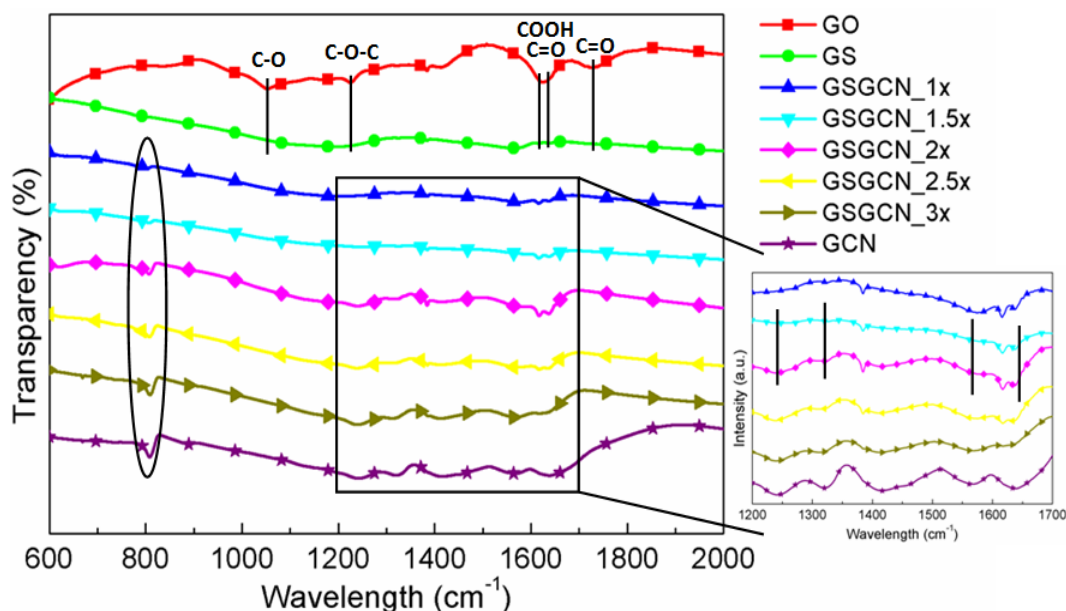


Figure 4-5. FTIR of GO, GS, GCN and GS/GCN intercalated composites. The ellipse and box (and also the lines in the inserted plot) represent the stretching mode of GCN; those lines in the main plot represent the vibration modes of epoxides, hydroxyls, carboxyls and ketones, respectively.

It is shown in XPS C1s spectra (**Figure 4-6**) that the intensities of C-O bond (~ 286.5 eV) and C=O bond (~ 288 eV) are largely reduced in GS and GS/GCN composites and the

atomic ratio of C_{sp2}/C_{sp3} increases from 0.9 for GO to 2.7 for GS.²¹⁸ Also the N-C=N bond (~288.3 eV) from GCN could hardly be observed in GSGCN_1x and GSGCN_1.5x, in line with the FTIR results. It's worth noting that the C-C bond (~284.7 eV in GS/GCN) and N-C=N bond (~288.1 eV in GS/GCN, if applicable) of GS/GCN composites show a right/left shift of ca. 0.1 eV compared with that of the pure GS and GCN respectively (highlighted by the dash lines in **Figure 4-6**), which should be attributed to the strong electron transfer between the intercalated GS/GCN interfaces.²⁰⁸ The relative ratios of pyridinic nitrogen bonding (~399 eV)²¹⁹ derived from XPS N1s spectra for the GSGCN_1x and GSGCN_1.5x are much lower than that of pure GCN (**Figure 4-7**), confirming the incomplete polymerization or partial decomposition of GCN discovered in the FTIR.

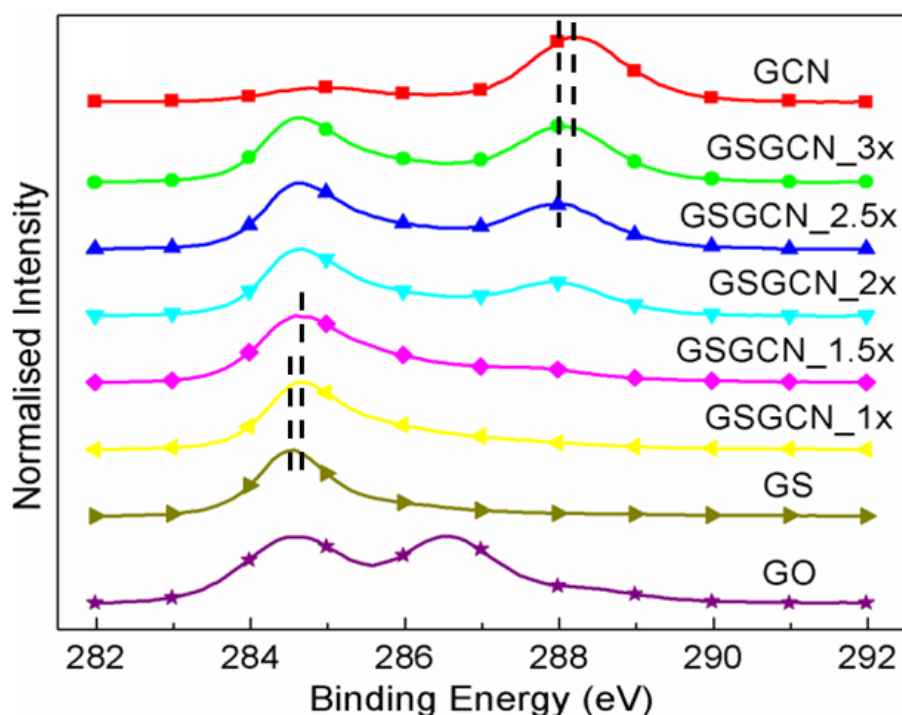


Figure 4-6. XPS C1s spectra for GO, GS, GCN and GS/GCN composites.

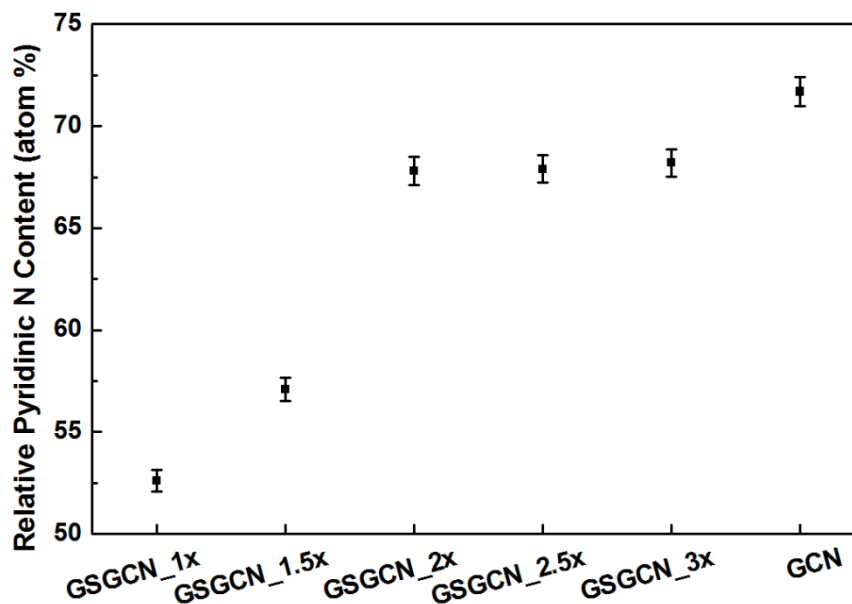


Figure 4-7. Relative pyridinic nitrogen content in GCN and GS/GCN intercalated composites derived from XPS N1s spectra.

The residual mass of the GS/GCN composites after thermogravimetric (TG) analysis (**Figure 4-8**) could be used to estimate the mixing ratio of GS/GCN in the composites²²⁰, since GCN has almost completely decomposed after heating at 800 °C while no significant weight change could be detected for GS. The decrease of the GS content in the composites, from GSGCN_1x to GSGCN_3x, is in agreement with the increasing nitrogen content derived from the XPS (**Figure 4-9**). Note that the intercalation of GCN into GS layer lowers the GCN decomposition temperature of 30 °C (**Figure 4-9**), indicating this intercalated hybrid structure decreases the decomposition temperature of GCN. Hence the lack of GCN pattern in GSGCN_1x and GSGCN_1.5x should be attributed to the partial decomposition of GCN.

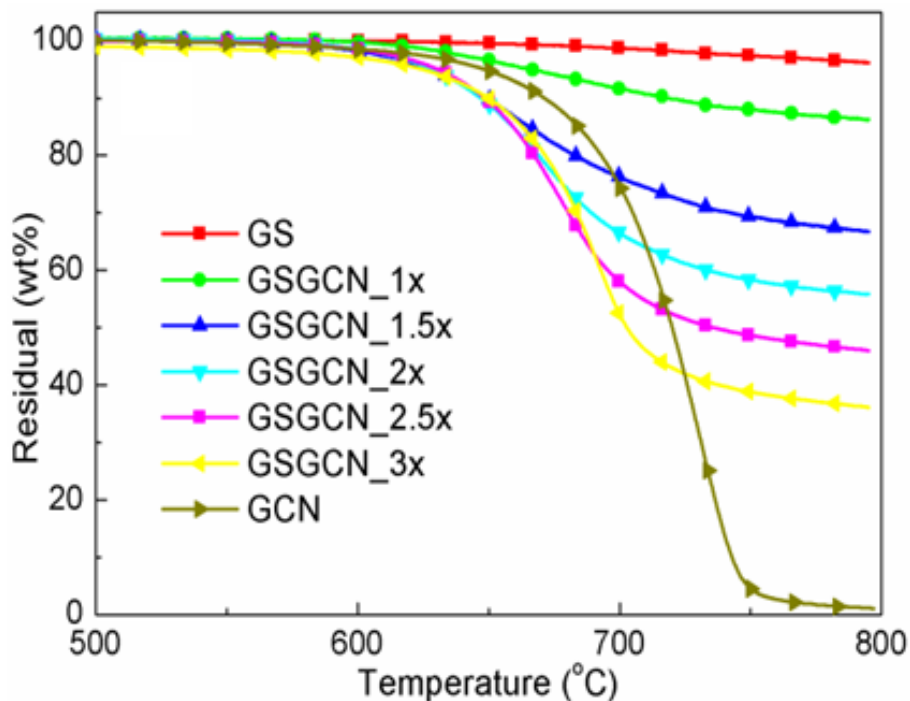


Figure 4-8. TG patterns for GS, GCN and GS/GCN intercalated composites in a flowing N_2 environment, from room temperature to $800\text{ }^\circ\text{C}$, with a ramping rate of $3\text{ }^\circ\text{C min}^{-1}$.

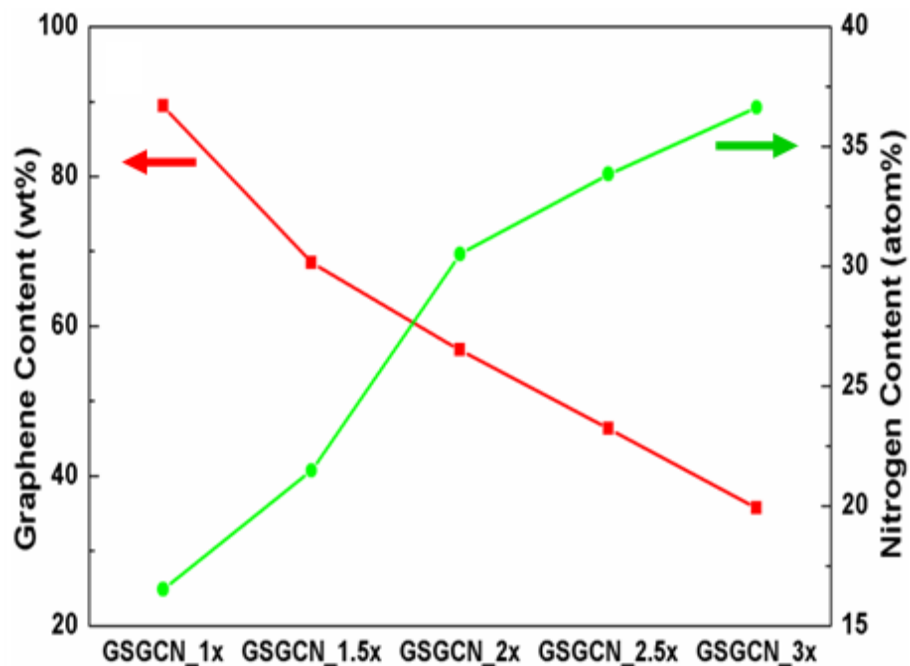


Figure 4-9. GS content in GS/GCN intercalated composites derived from the TG results and nitrogen content derived from XPS.

The electrocatalytic behaviours of intercalated GS/GCN composites are examined by cyclic voltammetry (CV) and the current density presented here equals the measured current divided by the geometric surface area of GC electrode. As shown in **Figure 4-10** that the ORR performances of all the GS/GCN composites with different GCN ratios are superior to that of pure GCN, in terms of both onset/peak reduction potential and current density. More importantly, as the GCN content in the composites increases initially, from GSGCN_1x to GSGCN_2x, the reduction current density increases while the onset/peak reduction potential remains the same; but when GCN content further increases, from GSGCN_2x to GSGCN_3x, both the reduction current density and potential decrease considerably and gradually show a pattern similar to that of pure GCN. Such phenomena could also be confirmed by linear sweep voltammetry (LSV) measurement (**Figure 4-11**).

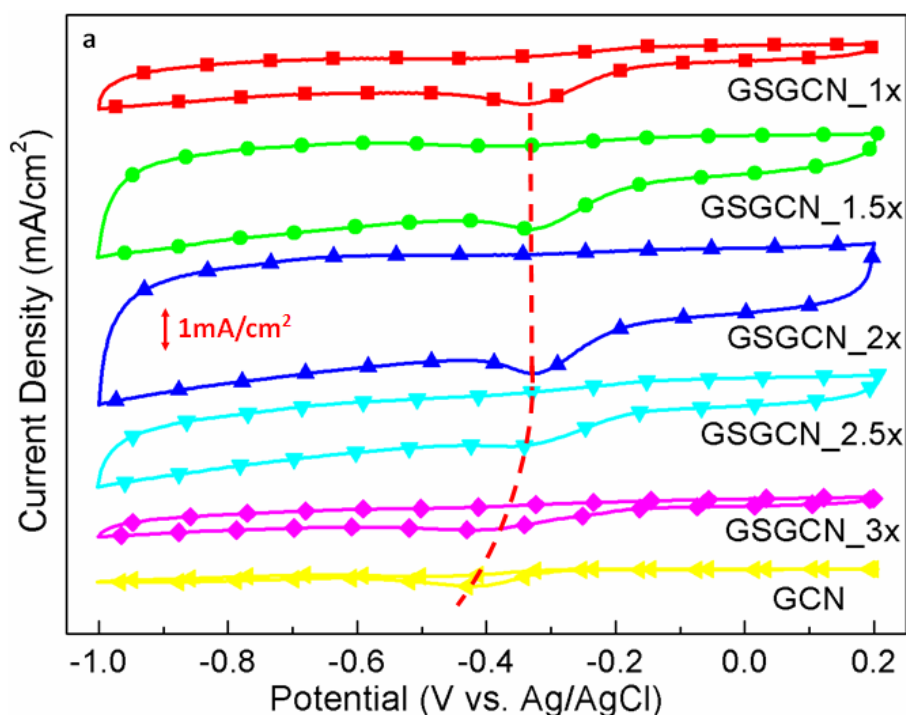


Figure 4-10. CV of GCN and GS/GCN intercalated composites (scan rate is 100 mV s^{-1}). The red curve highlights the shift of peak reduction potential in CV.

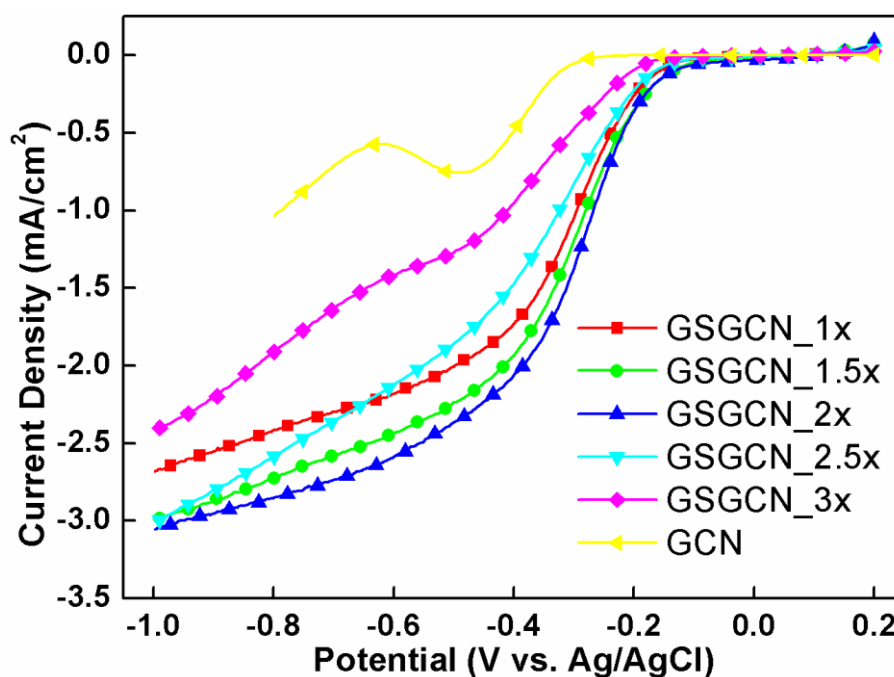


Figure 4-11. LSV of GCN and GS/GCN intercalated composites at 2000 RPM (scan rate is 10 mV s^{-1})

To explain the above observations on the ORR properties of GS/GCN intercalated composites, both structural characteristics and chemical composition need to be considered. Particularly, the BET SSA (m^2/g) and total nitrogen content from XPS (atom%) should be taken into account, as the surface nitrogen heteroatom is the origin of ORR catalytic activity. Here a new parameter called 'effective-SSA' (E-SSA) is introduced, which is defined as the product of SSA and nitrogen content. In this sense, E-SSA could represent the amount of active sites, and E-SSA normalized peak reduction current thus represents the conductivity, assuming no major difference in the mass transport capability for GS/GCN composites as they all possess layered structures, the similar macro-morphology. Note that little micro-pores can be observed in GS/GCN composites according to N_2 isotherms at 77 K (**Figure 4-3**), their double-layer capacitance (DLC) should mostly be proportional to the BET SSA in this

case. Hence, the influence of DLC on E-SSA normalised peak current density should also have been eliminated. It is shown in **Figure 4-12**, when the GCN content in the composites is low, the E-SSA normalized current is almost a constant, indicating sufficient conductivity supplied by the intercalated GS. As a result, the ORR performances, similar reduction potential but increasing current density from GSGCN_1x to GSGCN_2x, are dependent on the amount of active sites. However when the GCN content is in excess, though the E-SSA of GSGCN_2.5x and GSGCN_3x is similar to that of GSGCN_2x, the E-SSA normalized current decreases significantly, in accordance with the rapid decline in both reduction potential and peak current density. This suggests the amount of GS in the composites no longer affords to provide enough conductivity and the ORR activity turns into conductivity dependent. Accordingly, GSGCN_2x shows the best ORR performance among all five GS/GCN intercalated composites because it possesses the largest amount of active sites while remains sufficient conductivity. The increase in electrical conductivity, which is led by the intercalation of GS into GCN layers, is one of the key requirements for the improved ORR activities. Such an enhancement can be confirmed by the four-probe conductivity measurement (**Table 4-1**). Typically, the powder conductivity for GCN is under the detection limitation of the instrument, and thus must be smaller than $10^{-2} \text{ S cm}^{-1}$, similar to the previous report.²⁰⁴ For GS/GCN intercalated composites, the conductivity is about 0.5-4.5 S cm^{-1} , i.e. 3.06 S cm^{-1} for GSGCN_2x, at least two orders of magnitude greater than that of pristine GCN.

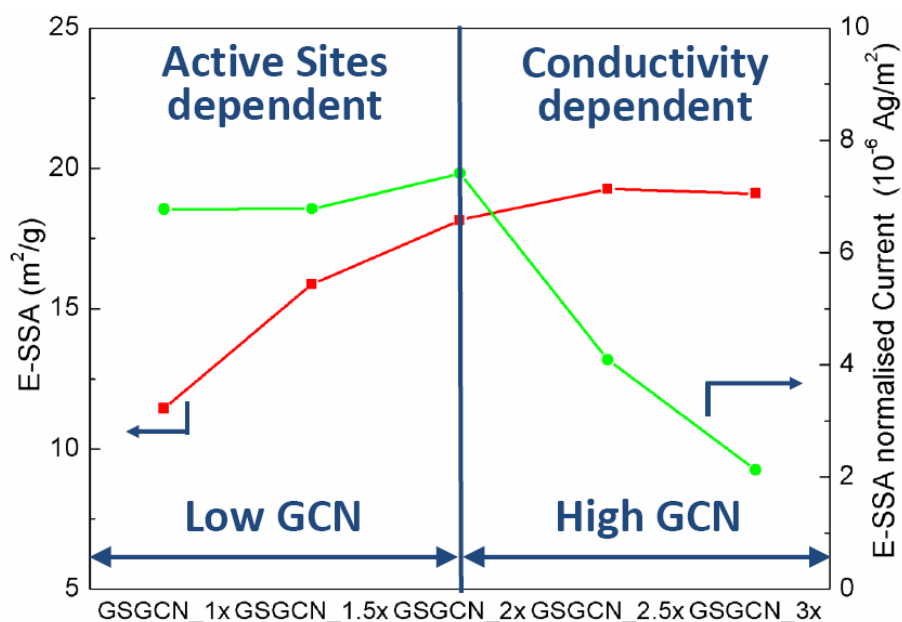


Figure 4-12. E-SSA and E-SSA normalized peak current for GS/GCN intercalated composites, calculated from the CV, BET and XPS nitrogen content.

Sample	S/cm
GCN	out of range
GSGCN-3x	0.53
GSGCN-2.5x	1.46
GSGCN-2x	3.06
GSGCN-1.5x	3.59
GSGCN-1x	4.37
GS	11.7

Table 4-1. Electrical conductivities of GCN, GS and GS/GCN intercalated composites.

Mass transport is another crucial factor for ORR besides active sites and electrical conductivity. Though macropores are capable of fast oxygen exchange during ORR, the relatively low surface area leads to a lack of exposed active sites.²²¹ It is thus expected hierarchical porosity with combined macropores and mesopores may solve the dilemma

of both high accessibility and high surface area, as macropores can promise efficient mass transport while mesopores offer sufficient accessible active sites. Here I demonstrate such a hierarchically porous GS/GCN intercalated composite (hp-GSGCN_2x) can be easily fabricated by the addition of excess silica nanospheres before the polymerization of GCN. The macroporosity of the hp-GSGCN_2x obtained is confirmed by SEM (**Figure 4-13**) and the mesopores with an average size close to the diameter of individual silica sphere template (ca. 10 nm) are shown under HRTEM (**Figure 4-14**). Note that the interlayer spacing of hp-GSGCN_2x (~0.33 nm, as shown in HRTEM) is close to that of GSGCN_2x, which means the hp-GSGCN_2x also remains the intercalated structure. The XPS patterns of hp-GSGCN_2x are similar to those of GSGCN_2x with a slight decrease in nitrogen content, but the SSA of hp-GSGCN_2x is ~50% greater than that GSGCN_2x, giving the overall E-SSA roughly 30% higher.

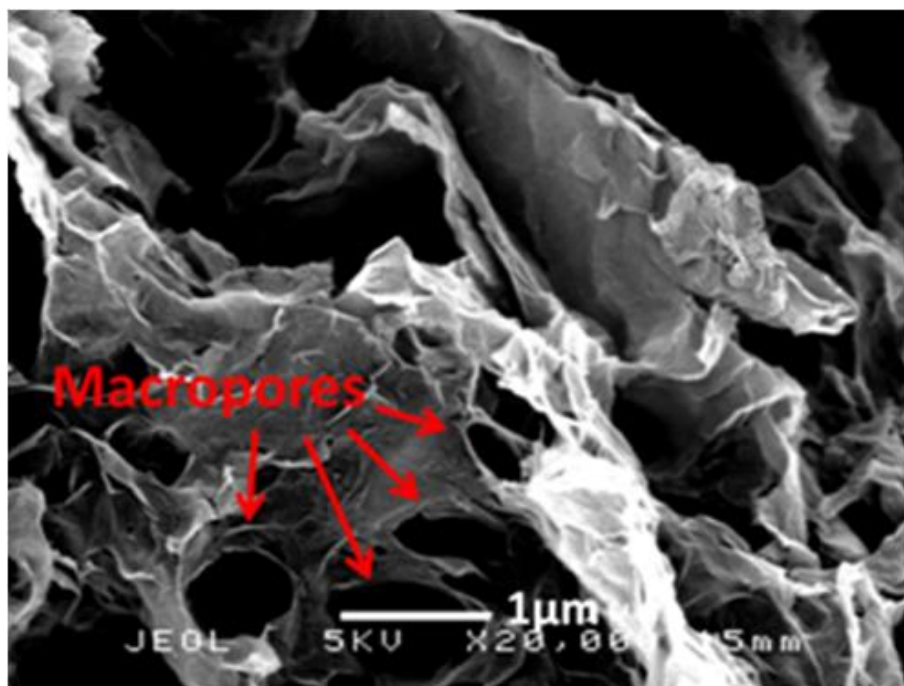


Figure 4-13. SEM image of hp-GSGCN_2x. The red arrows show the macropores.

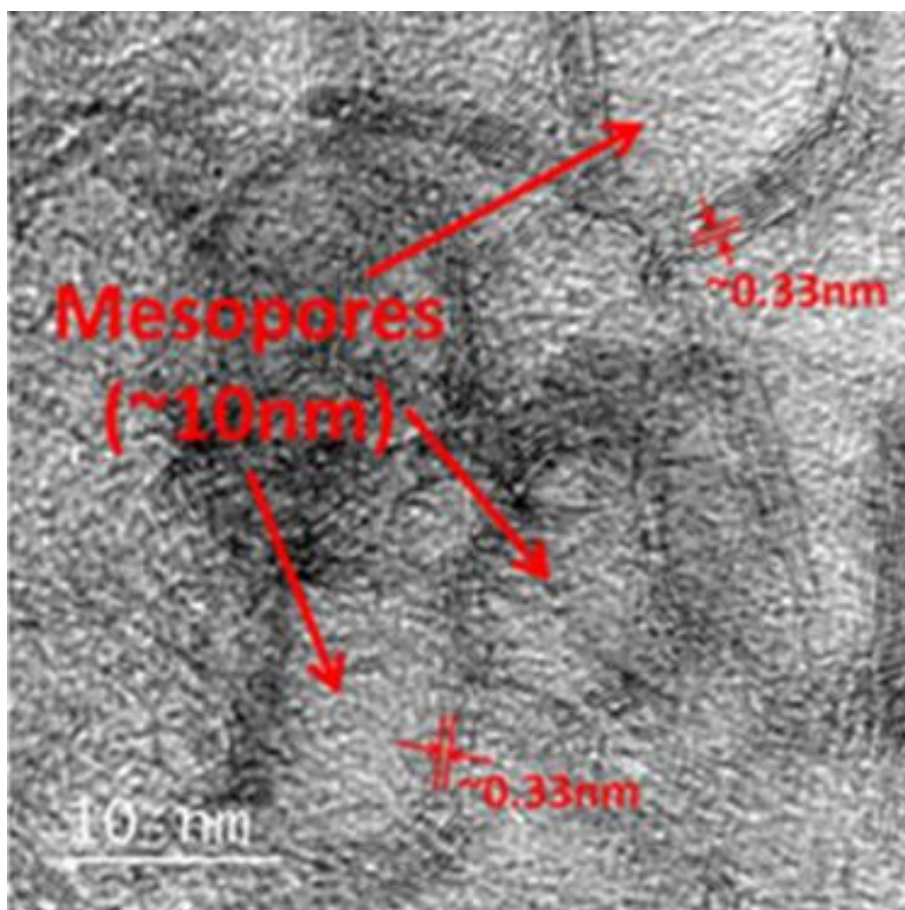


Figure 4-14. HRTEM image of hp-GSGCN_2x. The red arrows show the mesopores close to the size of silica sphere (ca. 10 nm). The inter-layer distance of GS/GCN composites is further confirmed to be 0.33 nm.

The ORR activities of hp-GSGCN_2x are first assessed by CV. As shown in **Figure 4-15**, the peak current density of hp-GSGCN_2x is almost 1.5 times higher than that of GSGCN_2x and the onset/peak reduction potential also increases by ~30 mV, which is further confirmed by LSV (**Figures 4-16 and 4-17**). Surprisingly, though the onset reduction potential of hp-GSGCN_2x is still lower than that of Pt/C, the current density surpasses Pt/C at a potential of only -0.24 V vs. Ag/AgCl and the half wave potential is only 90 mV lower. The electron transfer numbers for GSGCN_2x and hp-GSGCN_2x are calculated by the Koutecky-Levich equation.²²² It is shown in **Figure 4-18** that the

K-L plot of h-GSGCN_2x at -0.4 V vs. Ag/AgCl is parallel to the straight line for theoretical $4e^-$ pathway, and the electron transfer number is calculated to be 3.98 (**Figure 4-19**); on the other hand, the electron transfer number for GSGCN_2x is only 2.25, close to an indirect $2e^-$ pathway. In addition, the efficient $4e^-$ transfer for hp-GSGCN_2x can also be observed within a broad potential range from -0.3 to -0.6 V vs. Ag/AgCl, as shown in the **Figure 4-19**. Note that it is difficult for the adsorbed O_2 to be directly dissociated on carbon surface, the observed ' $4e^-$ transfer' via RDE measurement should be mostly referred to an associative $4e^-$ pathway, or in other word, the indirect '2+2' pathway.⁸⁸ Nevertheless, the excellent catalysis selectivity and fast ORR kinetics of hp-GSGCN_2x at a relatively high potential region should be attributed to the synergistic effect of the balanced active sites and electrical conductivity and so as the pre-designed hierarchically porous structure, especially those macrospores for facile mass transport. The enhancement in ORR performance derived from the hierarchical porosity can be further confirmed by the significantly reduced Tafel slope at the high potential range of -0.15 to -0.2 V vs. Ag/AgCl (70.6 and 108.9 mV dec⁻¹ for hp-GSGCN_2x and GSGCN_2x respectively, **Figure 4-20**). As far as I know, none of the existing metal-free GCN-based ORR catalysts possesses both the aforementioned excellent catalysis selectivity and fast ORR kinetics at such a relatively high potential region.¹⁹¹

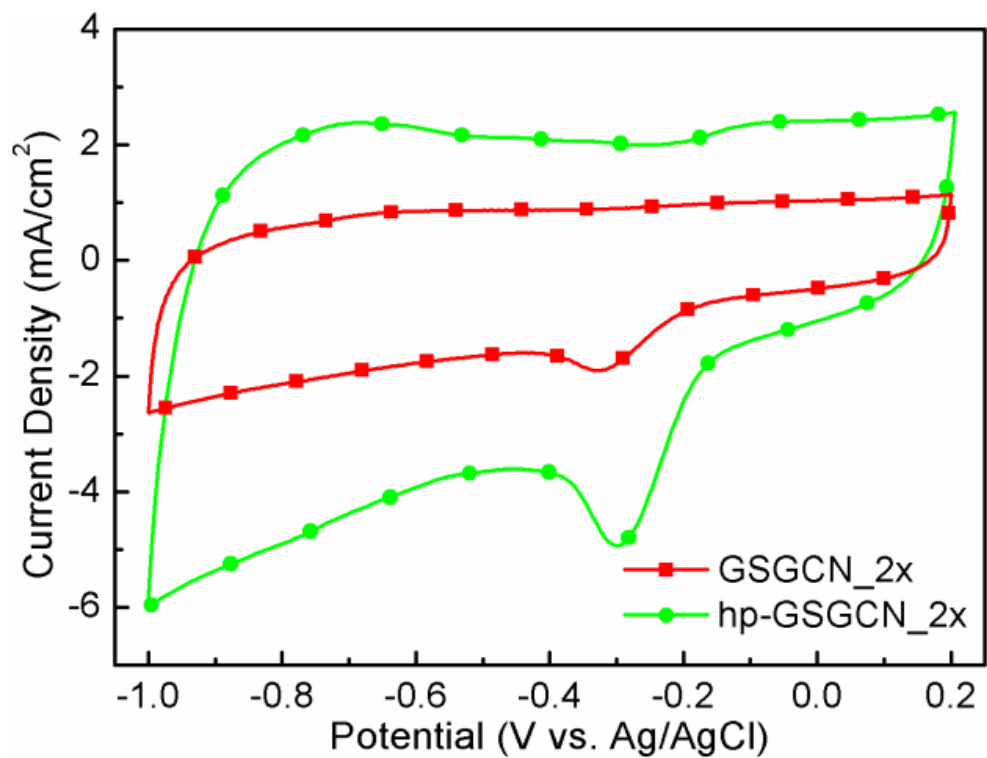


Figure 4-15. CV of GSGCN_{2x} and hp-GSGCN_{2x} (scan rate is 100 mV s⁻¹).

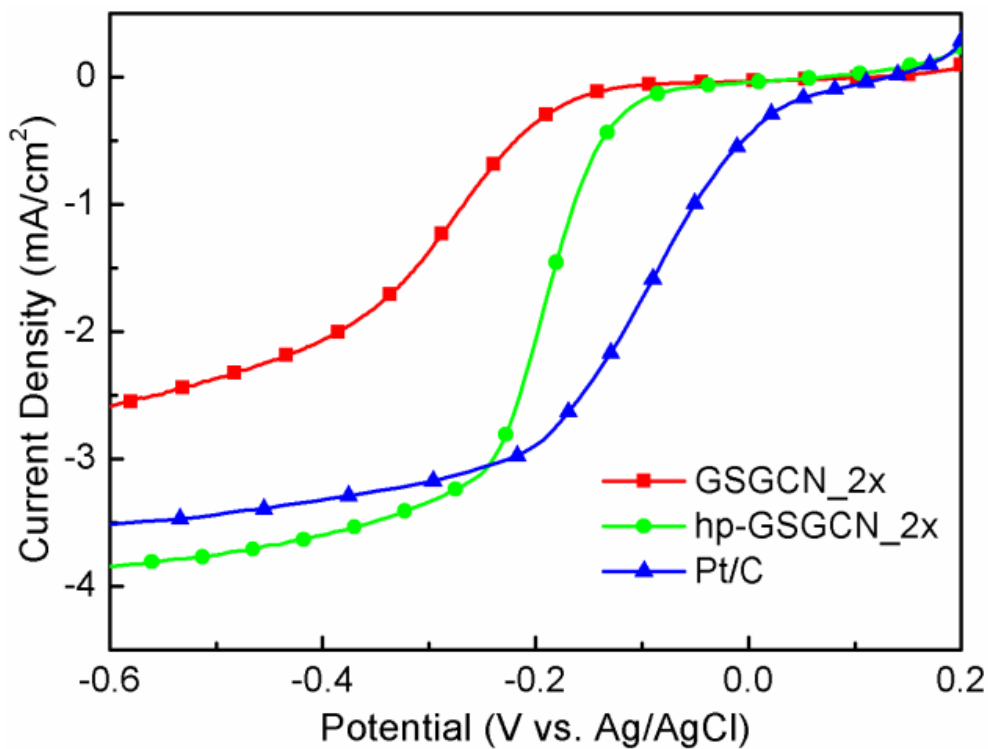


Figure 4-16. LSV of GSGCN_{2x}, hp-GSGCN_{2x} and Pt/C at 1500 RPM (scan rate is 10 mV s⁻¹).

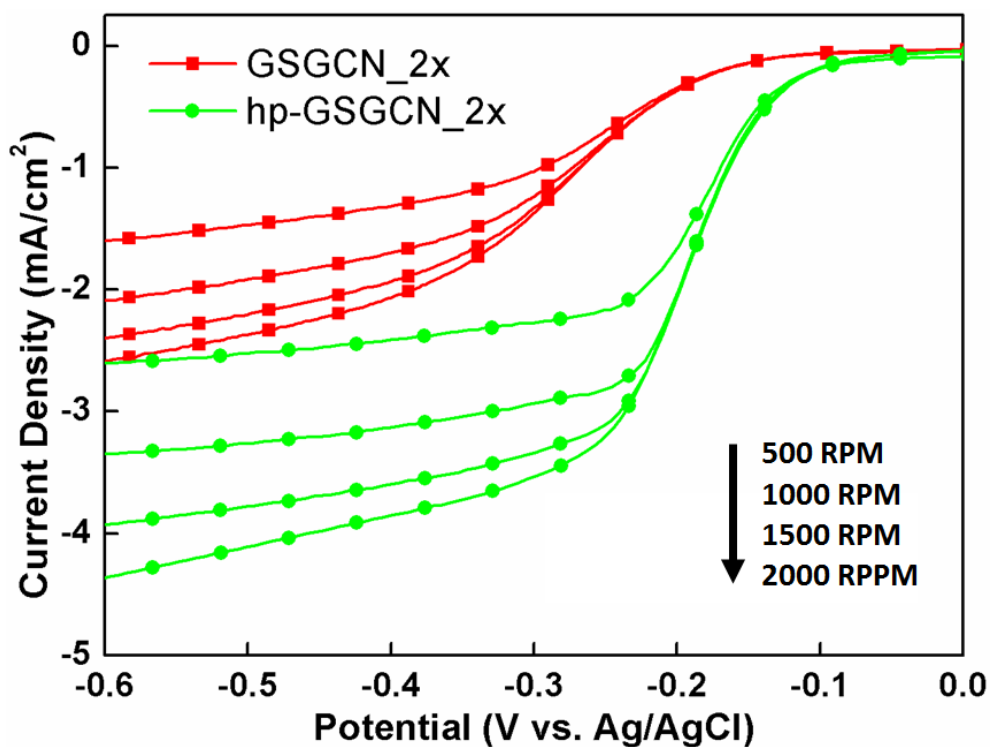


Figure 4-17. LSV plots of GSGCN_2x and hp-GSGCN_2x (scan rate is 10 mV s⁻¹).

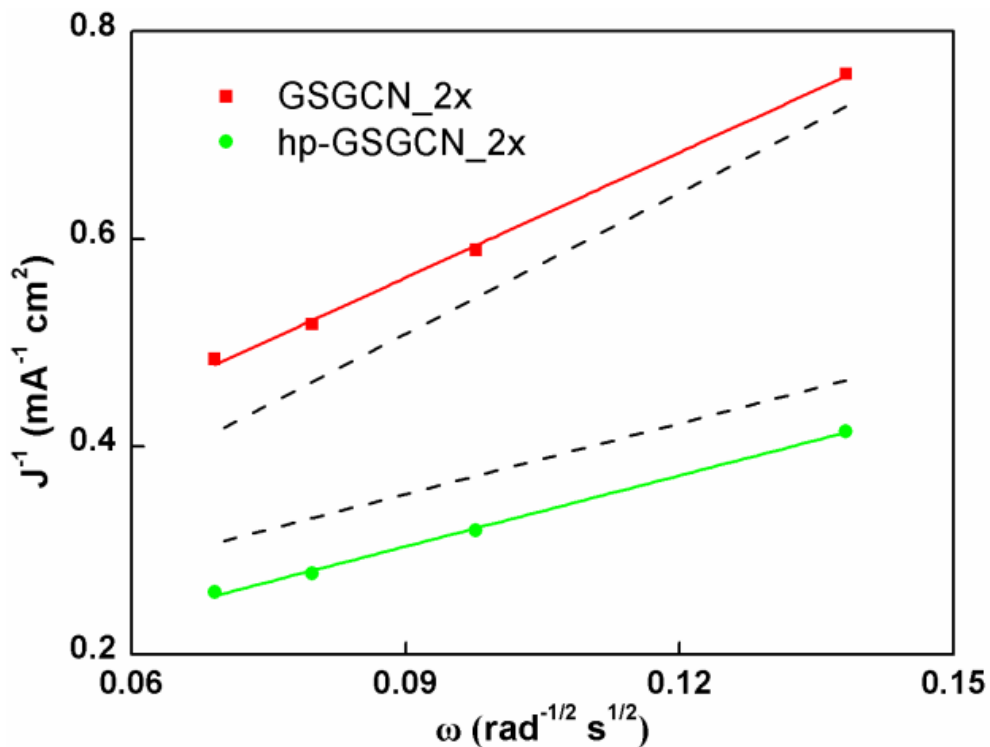


Figure 4-18. K-L plots of GSGCN_2x and hp-GSGCN_2x at -0.4 V (dashed lines represent the K-L plots for the theoretical 2e⁻ and 4e⁻ pathway).

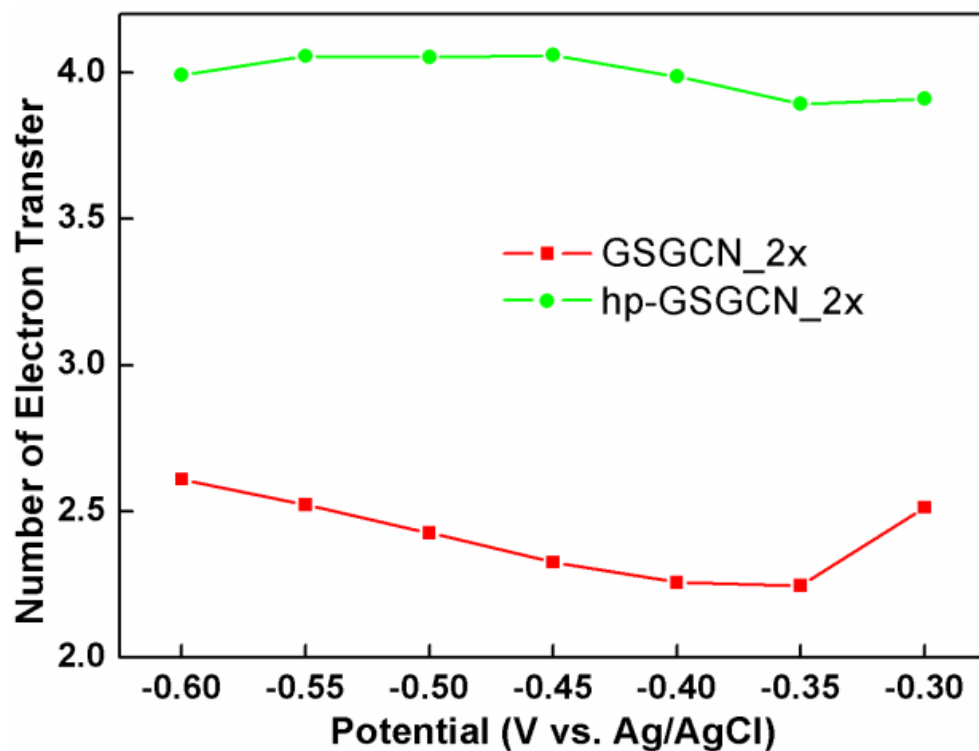


Figure 4-19. Number of electron transfer for GSGCN_2x and hp-GSGCN_2x at -0.3 to -0.6 V.

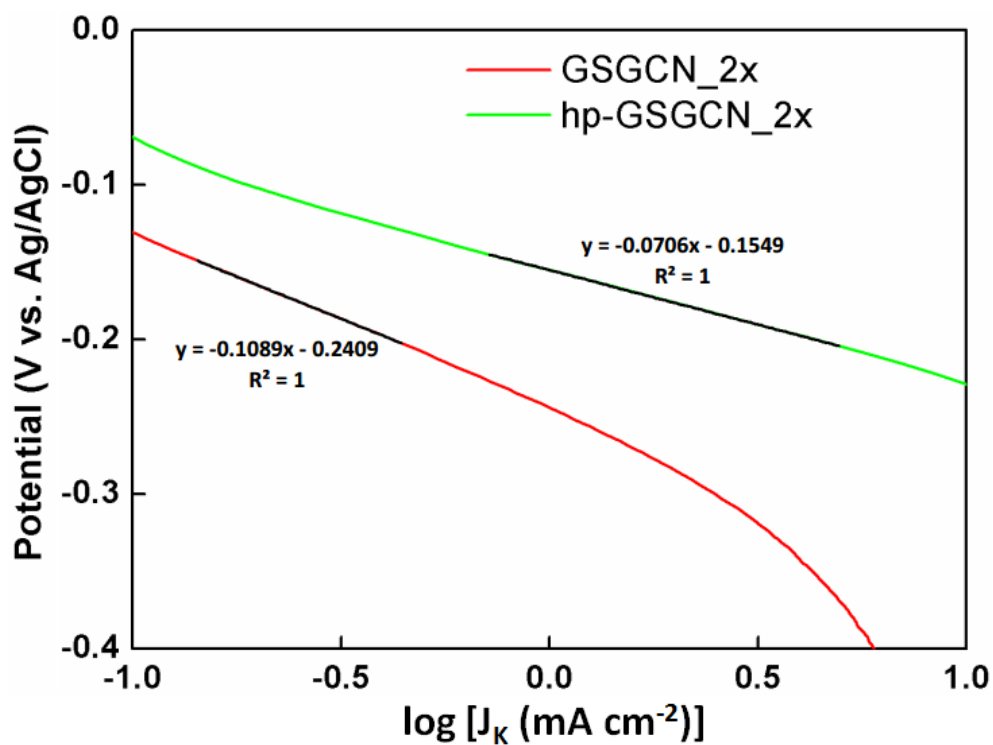


Figure 4-20. Tafel plots of GSGCN_2x and hp-GSGCN_2x, derived from LSV at 1500RPM. The linear fitting range is within the potential range of -0.15 to -0.2 V vs. Ag/AgCl.

Since safety is the first priority to the widespread application of electric vehicles, the tolerance against the methanol crossover effect should be of particular importance to the direct methanol fuel cells (DMFC), and so as the long-term durability. The methanol tolerance is evaluated by the current-time response at -0.3 V vs. Ag/AgCl. Oxygen is purged into the electrolyte from 500 s and 3M methanol is added in after 3500 s. It is shown in **Figure 4-21** that the ORR of Pt/C switches to a methanol oxidation reaction (MOR) after the addition of 3M methanol, as indicated by the shift to a positive current density,²²³ however the ORR activity of hp-GSGCN_2x is almost unaffected. The long-term durability of hp-GSGCN_2x and commercial Pt/C is also assessed through the chronoamperometric response at -0.3 V vs. Ag/AgCl. The ten-hour test (**Figure 4-22**) only causes a slight activity loss for hp-GSGCN_2x, whereas Pt/C loses nearly 40% of its initial activity. These two measurements confirm that the hp-GSGCN_2x in this work is much more stable in the alkaline electrolyte and against the methanol cross-over effect, compared with the commercial Pt/C.

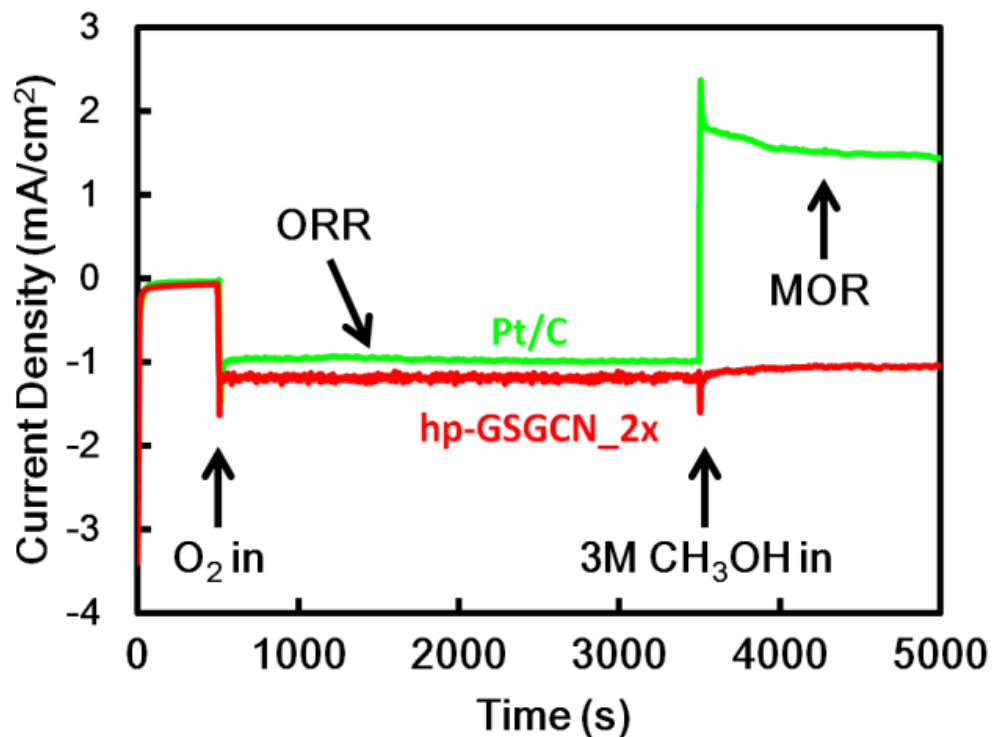


Figure 4-21. Chronoamperometric response of hp-GSGCN_2x and Pt/C in O₂-saturated 0.1M KOH + 3M CH₃OH, under 1600 RPM, at -0.3 V vs. Ag/AgCl for methanol tolerance.

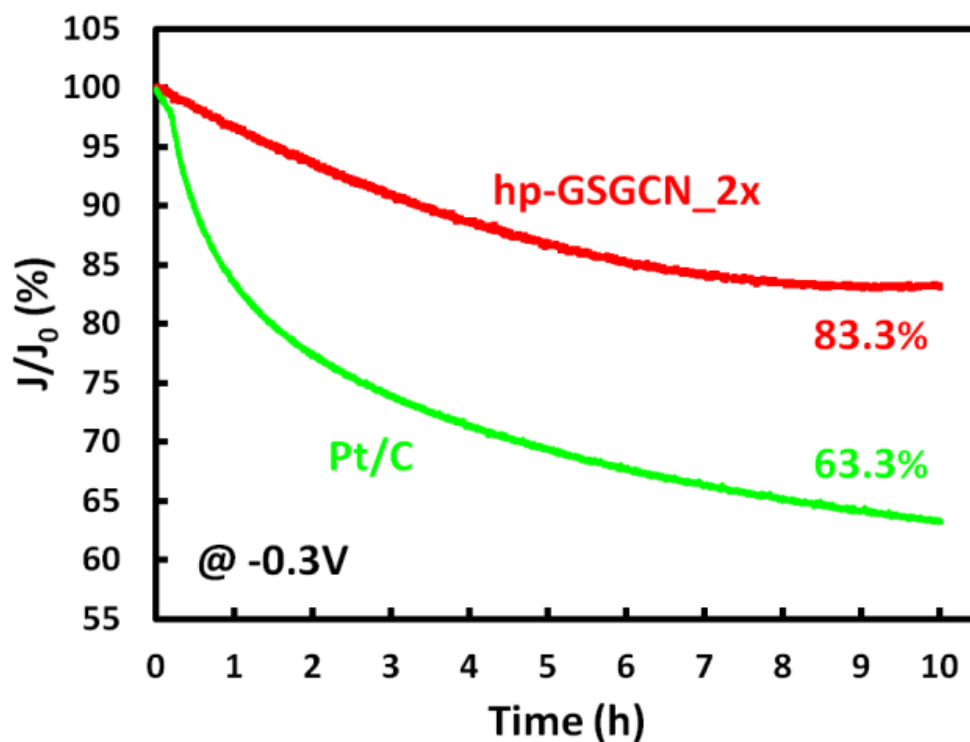


Figure 4-22. Chronoamperometric response of hp-GSGCN_2x and Pt/C CA in O₂-saturated 0.1M KOH, under 1600 RPM, at -0.3 V vs. Ag/AgCl for long-term stability.

4.3 Summary

In this work, a facile synthesis method of hierarchically porous GS/GCN intercalated composites is presented, and the composites display much better ORR activities than the existing GCN-based catalysts and also improved durability and methanol tolerance compared with commercial Pt/C.

However, it is noted that the onset overpotentials of the hp-GSGCN_2x are still larger than that of the commercial Pt/C, despite the fact that a comparable reduction current density can be achieved. Hence, in the next chapter, non-precious metal catalysts with higher onset reduction potential (i.e. iron based compounds) will be introduced to the heteroatom doped graphene framework. It is expected that the strong interaction between the metal / metal oxide and doped carbon obtained, as well as the synergistic effect of two different active sites, can lead to significantly reduced overpotentials while retaining the excellent catalysis selectivity and fast kinetics.

Chapter 5. Maghemite Embedded Nitrogen Doped Graphene Framework

5.1 Introduction

The best-known non-precious metal (NPM) ORR catalysts consist of nitrogen, carbon and transition metals, such as Fe (Fe/N/C).¹²⁶ Progress has been made towards the synthesis methods of Fe/N/C catalysts and the understanding of their ORR characteristics, including the recognition of the essential role of a thermal treatment step and the strong dependence of ORR activity on the type of precursors and their concentrations to achieve the Fe/N/C system.²²⁴ The strong interaction between iron compounds and nitrogen doped carbon substrates is also found beneficial to enhance the stability and reduction potential.²²⁵

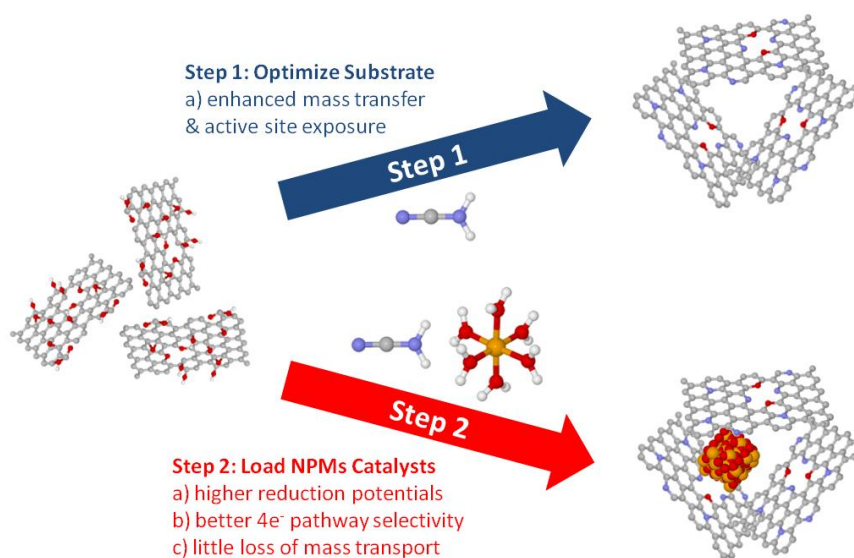
However, in spite of the above achievements, a key challenge remains that most of the reported activities of such NPMs catalysts are yet to match all the performance indicators of the equivalent PtC.¹⁹³ On the other hand, apart from the cost issue, the current PtC catalysts also suffer from several weaknesses: 1) poor mass transfer owing to the non-optimized carbon substrate;²²⁶ 2) reduced number of electrons transferred in the mixed kinetic-diffusion region as a result of peroxide (HO_2^-) formation on surface oxide;²⁹ and 3) structural instability leading to dissolution of Pt during ORR.²²⁷

Given that both chemical composition and structure are critically important for ORR, a rational design of facile NPMs must consider both properties. An ideal NPM catalyst

should consist of: 1) an optimized hierarchical substrate to ensure sufficient mass transfer and catalytic sites exposure; 2) active NPM catalytic sites with strong HO_2^- binding to promote four electron ($4e^-$) transfer pathway, and with comparable oxygen adsorption kinetics to Pt for enhanced onset reduction potential; and 3) strong and stable interaction between NPMs and the substrate for prolonged lifetime. In this regard, I propose a two-step design process for such highly efficient NPM catalysts: 1) hierarchical porosity of the supporting substrate is formed and optimised in advance, especially to achieve high total pore volume for rapid mass transfer; and 2) a suitable amount of NPM precursor is introduced into the optimal substrate to form well dispersed nanoparticles, so as to boost the reduction potential while maintaining the hierarchical nanostructure.

Based on this design principle, herein I report a successful example of forming and confining phase-pure maghemite nanoparticles ($\gamma\text{-Fe}_2\text{O}_3$) into a hierarchically porous nitrogen-doped graphene framework (**Scheme 5-1**). A porous graphene framework (GF_800) was adopted as the baseline substrate since the hydrothermal self-assembly of graphene oxide can readily form a hierarchical nanostructure, with a substantial amount of micro- / meso- pores (i.e. < 6 nm) and large interconnected voids (i.e. > 1 μm). Such hierarchical porosity is optimized by adjustment of the concentration of a nitrogen precursor (GF+N2_800), and can be largely preserved after the addition of a small quantity of an iron precursor (GF+N2+Fe1_800). Furthermore, the nitrogen doping is expected to facilitate the anchoring and fixation of the more active iron compound on the substrate and thus to improve the stability of the proposed catalysts. The resulting porous graphene-framework confined maghemite system, GF+N2+Fe1_800, surpasses

the performance of the equivalent commercial PtC, in terms of more positive half-wave reduction potential, significantly lower peroxide formation ratio, more than triple the kinetic current density, smaller Tafel slope, and better durability. To the best of my knowledge, the activity of this nanoconfined maghemite system is among the best of all the existing Fe-based ORR catalysts. More importantly, the same synthesis approach was applied to confine Pt nanoparticles and the resulting material, GF+N2+Pt1_800, shows nearly identical ORR behaviours with the nanoconfined γ -Fe₂O₃ (GF+N2+Fe1_800). This indicates that the proposed design principle should have wide applicability for optimization of graphene supported NPM catalysts for ORR.



Scheme 5-1. The proposed two-step design principle for one-pot synthesis of highly efficient NPM ORR catalysts: Step 1 is to optimize in advance the conditions of N-doping and hydro-thermal synthesis, to achieve a highly porous “support-structure” with an optimum N content; and, Step 2 uses the optimized conditions to optimize the Fe precursor content, where the Fe precursor was added to the optimized “support-structure” precursors in Step 1 (but not to the prior-formed structure!). The overall synthesis of the catalyst system is in “one pot” under the optimized conditions, followed by high temperature calcinations.

5.2 Results and Discussion

5.2.1 Formation of Highly Porous N-doped Graphene Framework

As the first-step of the synthesis approach is to produce an optimized porous substrate, characteristics of the porosities of the synthesized samples were first compared from the scanning electron microscopy images (SEM), **Figures 5-1 to 5-4**. An evident hierarchical structure (pore size ranging from ca. 0.5-1.5 μm) is shown in the SEM image of GF (**Figure 5-1**), but such porous characteristics can hardly be seen in GF+N2 (**Figure 5-2**). After thermal annealing, no apparent difference is observed between the morphology of GF and GF_800 (**Figure 5-3**), implying the high temperature treatment changes little of their macroscopic porosity. However, GF+N2_800 exhibits a more hollow structure with larger interconnected voids (ca. > 2 μm , **Figure 5-4**) after thermal annealing. The distinct morphology of GF+N2 and GF+N2_800 suggests that during hydrothermal reaction, the nitrogen precursors are 'attached' to graphene surface and block most of the pores; such nitrogen species are partially removed from and partially doped into the graphene framework in the following thermal treatment, during which the structure of graphene framework is severely etched.

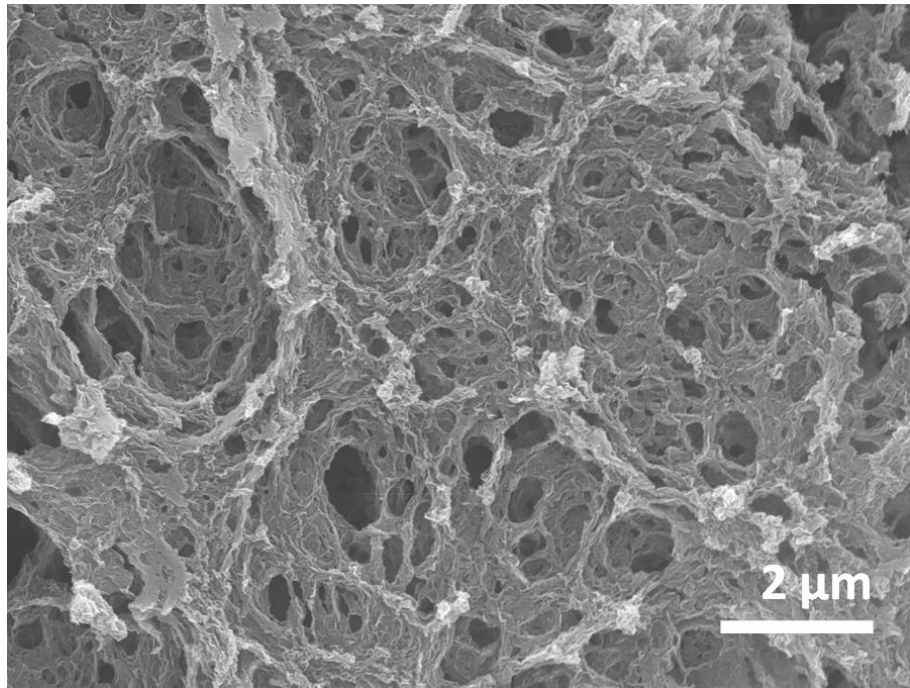


Figure 5-1. SEM image of GF.

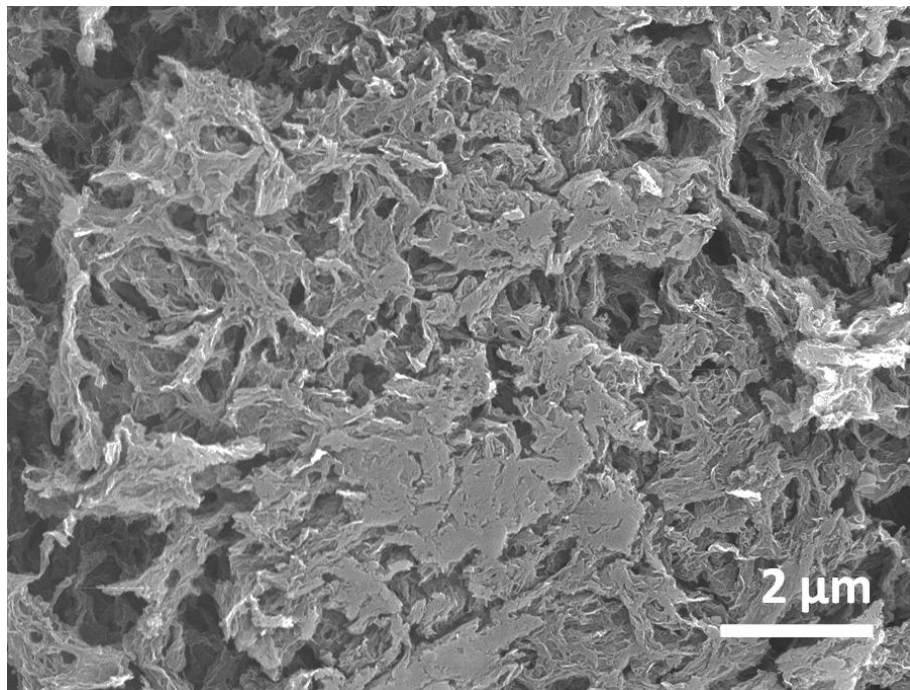


Figure 5-2. SEM image of GF+N2.

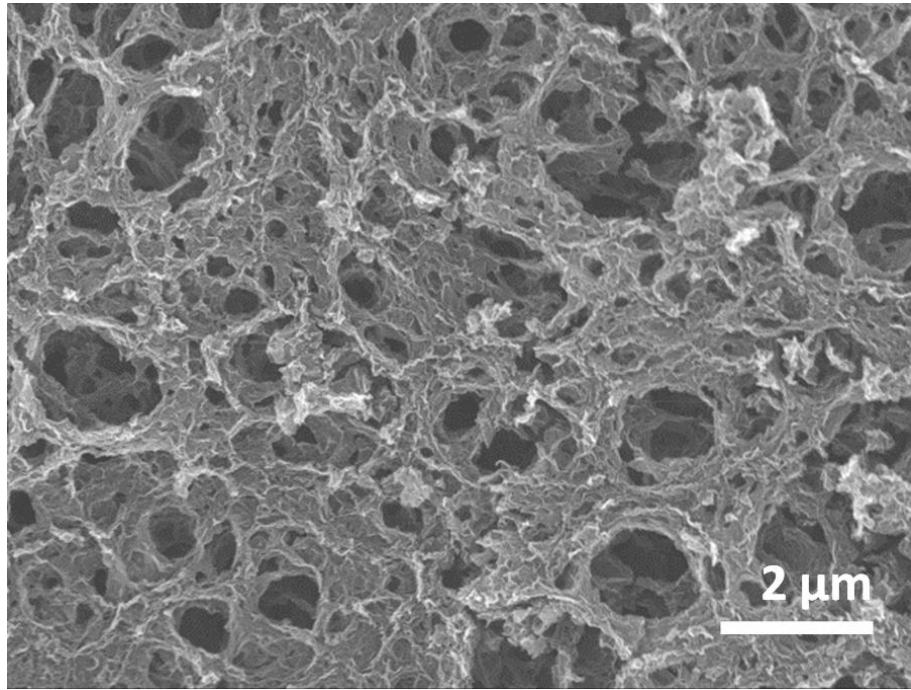


Figure 5-3. SEM image of GF+800.

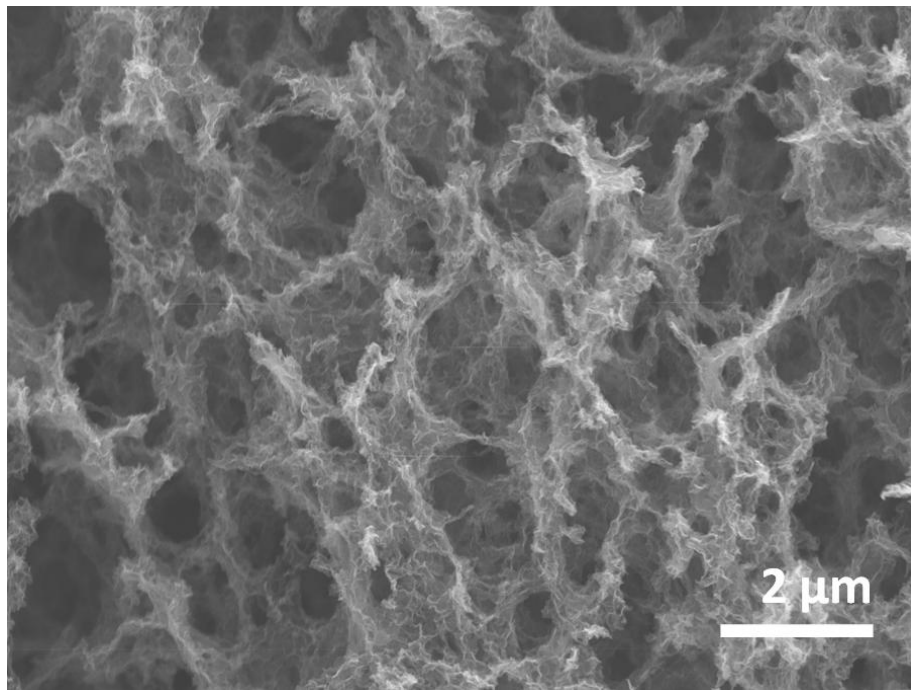


Figure 5-4. SEM image of GF+N2_800.

The removal of attached nitrogen species was probed by thermal gravimetric analysis (TGA), **Figure 5-5**. It is seen that an extra sharp decrease of mass occurs between 230 and 350 °C for GF+N₂, compared with the continuous but slow mass loss for GF as temperature increases. The nitrogen doping process was demonstrated through the transformation from the predominantly graphitic N of GF+N₂ to the pyridinic N of GF+N₂_800, as shown by X-ray photoelectron spectroscopy (XPS), **Figure 5-6**. Both the concentration and the type of doped-N sites influence the electrochemical properties of the materials. Despite the debate on the exact role of N-doped sites, pyridinic N is generally regarded as responsible for the catalytic ORR activity, especially for the onset reduction potential; while graphitic N is believed to be beneficial to the electrical conductivity. Since those GF+N_800 samples show similar nitrogen content and binding configurations (**Table 5-1**), it is reasonable to attribute the major improvement in performance to their different porous structures.

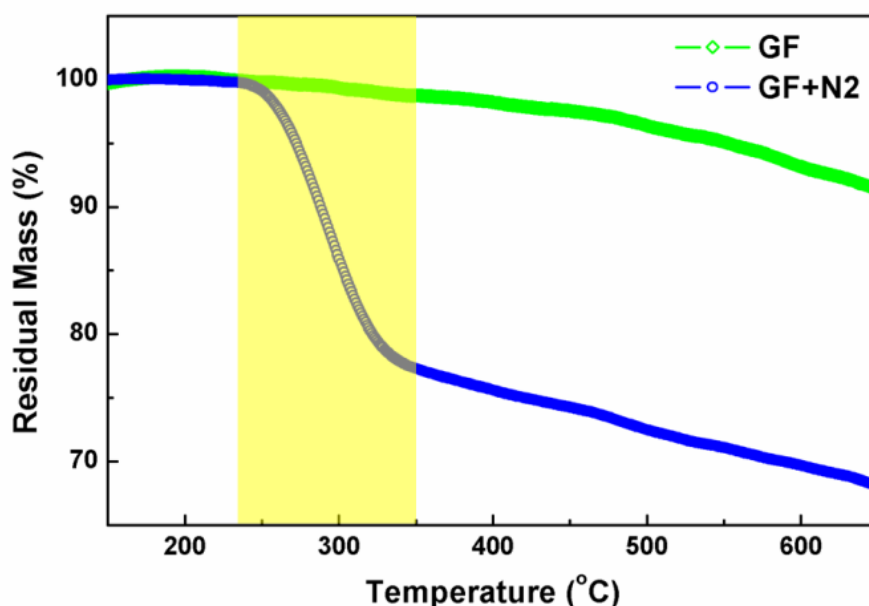


Figure 5-5. TGA of GF and GF+N₂ under N₂ gas environment with a ramping rate of 3 °C min⁻¹.

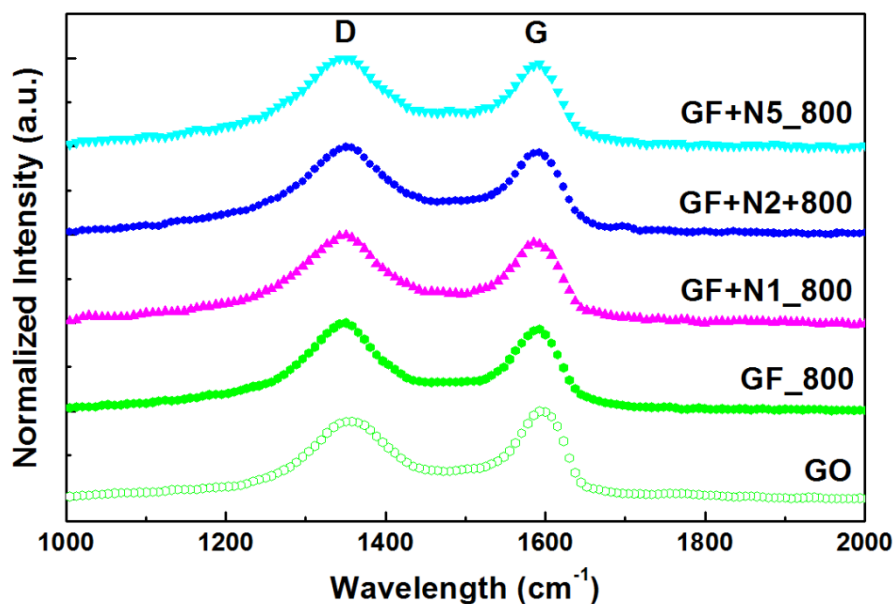


Figure 5-6. Raman spectra of GO, GF_800, GF+N1_800, GF+N2_800, and GF+N5_800.

The porosity of each substrate was further investigated by nitrogen adsorption / desorption isotherms at 77K, **Figures 5-7 and 5-8**. It is shown that all the GF+N and GF+N_800 possess a hierarchically porous nanostructure, featuring an initial adsorption for micropores (i.e. $P/P_0 < 0.01$), a hysteresis loop for mesopores (i.e. $P/P_0 > 0.4$), and long 'tail' for large macropores / voids (i.e. the highest P/P_0). It is also seen that the N_2 sorption for GF+N is generally lower than that for GF, while GF+N_800 possess higher sorption than GF_800. The corresponding pore size distribution (PSD, **Figures 5-9 and 5-10**) calculated by the QSDFT (Quenched Solid Density Functional Theory) model illustrates that for GF and GF_800, the thermal 'etching' (as confirmed in TGA) removes the residual oxygen functional group on graphene surface and turns those small micropores (0.8-1 nm) into relatively large ones (1-2 nm) and even meso-pores (3-6 nm). With regard to the GF+N and GF+N_800, the addition of nitrogen precursors during hydrothermal reaction blocks most of the micro- / meso-pores as discussed above; the

following thermal annealing not only re-opens those pores but also generate a large number of new structural defects.

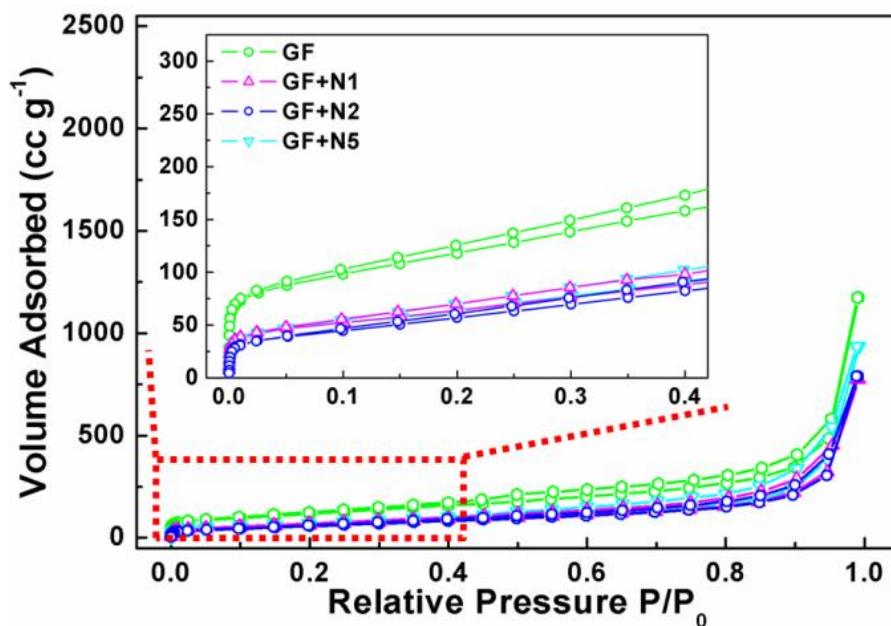


Figure 5-7. N₂ adsorption / desorption isotherms at 77K for GF+N.

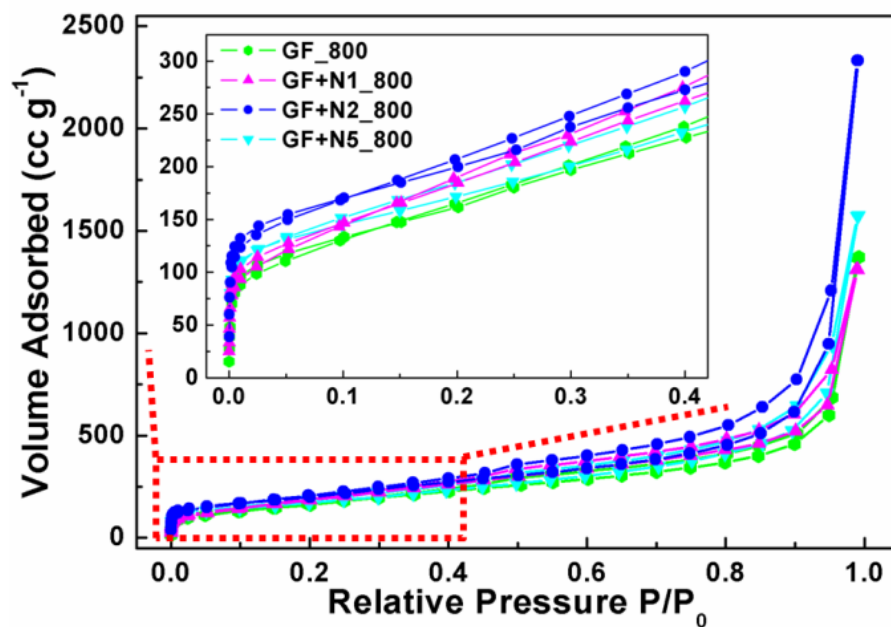


Figure 5-8. N₂ adsorption / desorption isotherms at 77K for GF+N₈₀₀ materials.

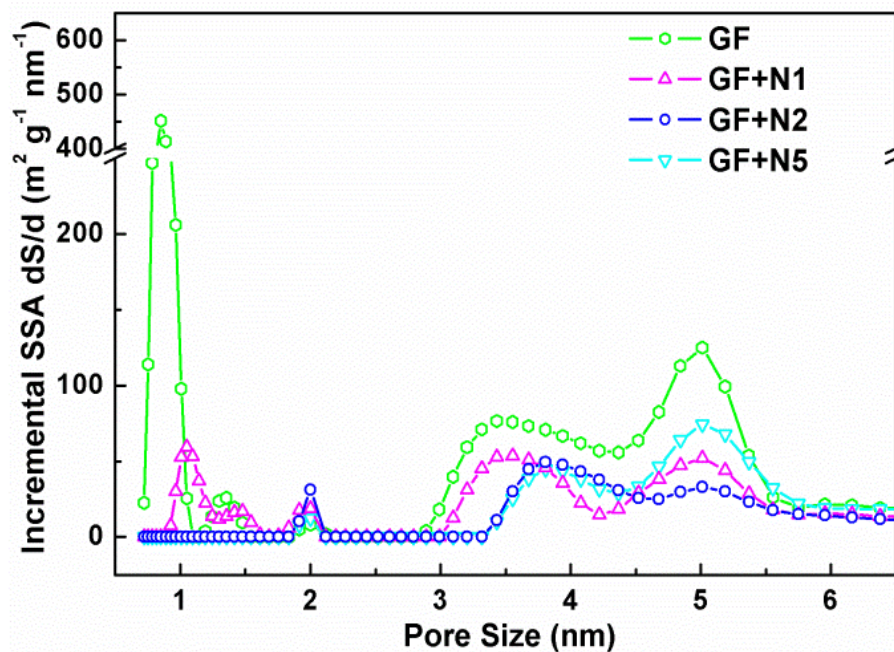


Figure 5-9. PSD of GF+N derived from N₂ isotherms at 77 K, calculated by the QSDFT model.

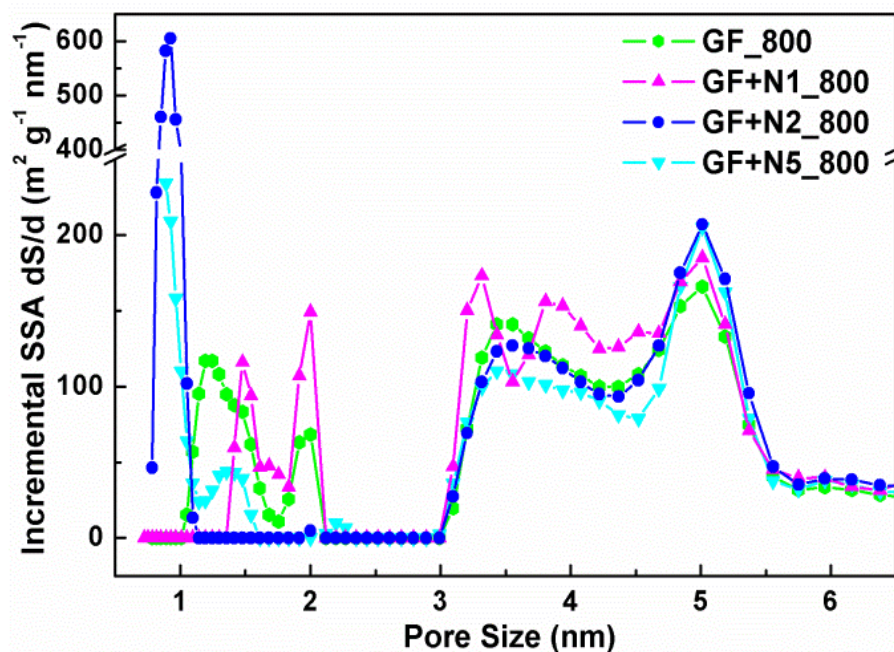


Figure 5-10. PSD of GF+N₈₀₀ derived from N₂ isotherms at 77 K, calculated by the QSDFT model.

The GF+N₈₀₀ generally show a higher Brunauer–Emmett–Teller specific surface area (BET SSA) and/or total pore volume (PV) than GF₈₀₀ (**Table 5-1**). It is noted that the

concentration of the nitrogen precursor is crucial to optimize the hierarchical porosity: when too low, it cannot block all the attachable sites during hydrothermal reaction; but when too high, it hampers the subsequent thermal etching (**Figures 5-9 and 5-10**). Therefore GF+N2_800, with an intermediate concentration of the nitrogen precursor, possesses the highest BET SSA of 741.2 m² g⁻¹ and PV of 3.62 cc g⁻¹. The surprisingly large total PV (almost double the value of the rest of the GF+N_800) is believed to be favourable for rapid mass transfer during ORR.

Sample	BET		Elemental (at %)			C1s (at %)			N1s (at%)		
	SSA (m ² g ⁻¹)	PV (cc g ⁻¹)	C	N	O	C=C	C-C	C-O/C-N	Pyridinic	Graphitic	Oxidised
GF+N0	437	1.82	85.3		14.8	71.4	17.4	11.2			
GF+N1	244	1.20	75.2	12.3	12.5	59.5	19.2	21.4	16.8	83.2	
GF+N2	229	1.22	71.7	15.0	13.3	56.9	21.0	22.1	23.1	76.9	
GF+N5	258	1.45	67.0	19.6	13.4	63.6	19.9	26.4	33.2	66.8	
GF+N0_800	598	2.13	94.4		5.7	80.2	15.8	4.0			
GF+N1_800	729	2.03	90.5	4.4	5.1	78.0	18.4	3.6	46.9	44.1	9.0
GF+N2_800	741	3.62	88.4	5.5	6.1	75.7	18.8	5.6	43.3	49.1	7.6
GF+N5_800	627	2.44	90.4	4.4	5.2	64.0	27.2	8.9	43.9	47.6	8.5

Table 5-1. Summary of BET SSA, total pore volumes, elemental ratios, XPS C1s / N1s binding configurations for GF+N and GF+N_800.

5.2.2 Nano-confinement of Maghemite Catalysts

The second step of the proposed design principle is to load an appropriate amount of NPM catalysts in the optimized substrate. The influence of NPM concentration on the overall porosity was studied through N₂ sorption isotherms, **Figure 5-11**, and it is shown that the N₂ sorption for GF+N2+Fe_800 decreases as the Fe ratio increases. The large reduction in the micro- / meso-porosity of GF+N2+Fe_800 (**Figure 5-12**) confirms most of the Fe compounds have been successfully confined into the porous GF+N2_800. What's more, adding the same amount of Fe compound into the GF+N1_800 ends up

with considerably smaller SSA and PV of GF+N1+Fe1_800 than those of GF+N2+Fe1_800 (Table 5-2), clearly pointing out the importance of a pre-optimized substrate for the nanostructure of the final GF+N+Fe_800.

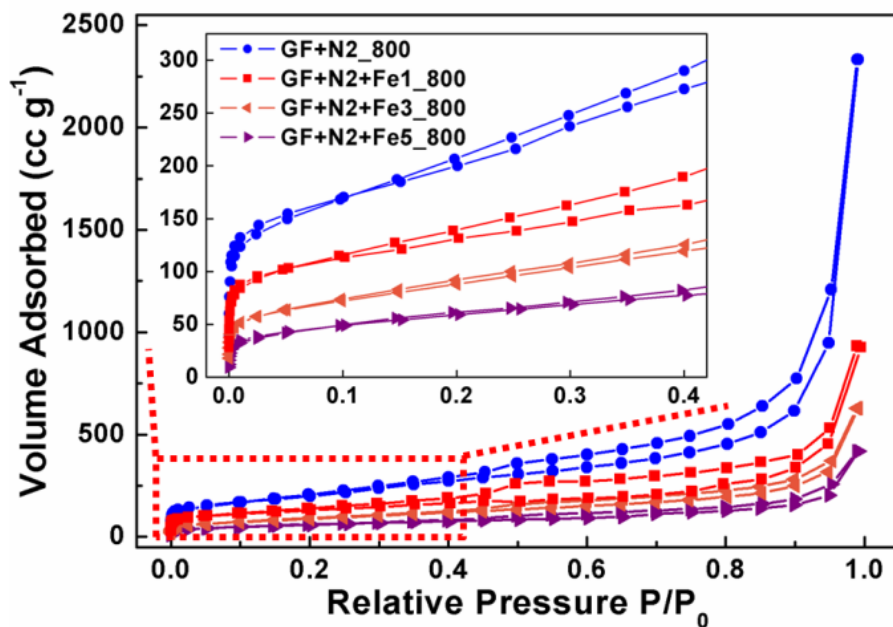


Figure 5-11. N₂ adsorption / desorption isotherms at 77K for GF+N+Fe₈₀₀ materials.

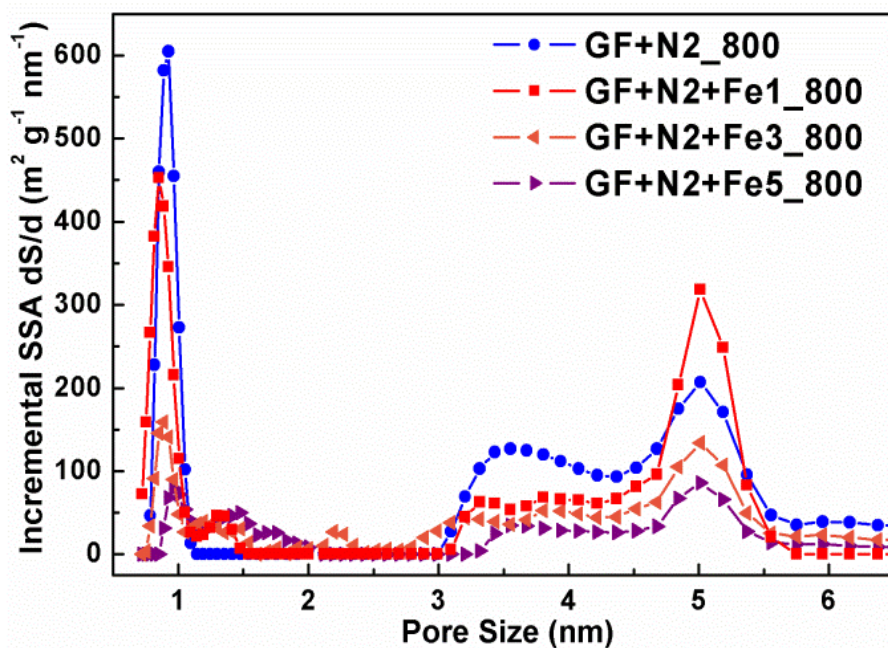


Figure 5-12. PSD of GF+N+Fe₈₀₀ derived from N₂ isotherms at 77 K, calculated by the QSDFT model.

Samples	BET SSA (m ² g ⁻¹)	Total PV (cc g ⁻¹)
GF+N2+Fe1_800	450	1.43
GF+N2+Fe3_800	357	1.05
GF+N2+Fe5_800	217	0.65
GF+N1+Fe1_800	352	1.19

Table 5-2. BET SSA and total PV of GF+N+Fe_800.

The chemical composition of the Fe-containing species was first characterized by X-ray diffraction (XRD), **Figure 5-13**, and it is shown that the XRD pattern of the GF+N2+Fe1_800 fits perfectly with the standard γ -Fe₂O₃ reference. Note that maghemite has almost the same crystal structure as magnetite (Fe₃O₄), X-ray photoelectron spectroscopy (XPS) was further adopted to differentiate those two phases. It is shown in the XPS Fe2p spectrum of the GF+N2+Fe1, **Figure 5-14**, the peaks centred at 710.8 and 724.3 eV represent Fe(III) 2p_{3/2} and 2p_{1/2}, respectively, and no Fe(II) or metallic Fe peak is observed (i.e. 709.6 or 706.7 eV for Fe(II) or Fe(0) 2p_{3/2}). In addition, the satellite Fe 2p_{3/2} peak at 718.8 eV is characteristic of Fe₂O₃, while for Fe₃O₄ the satellite peak is generally within ca. 715-716 eV. Therefore, it is evident that γ -Fe₂O₃ is the only iron compound in the GF+N+Fe_800, from both XRD and XPS observations. Moreover, the peak position of pyridinic N in GF+N2+Fe_800 is ca. 0.2 – 0.3 eV more positive than that for GF+N2_800, **Figure 5-15**, which indicates the interaction between γ -Fe₂O₃ and nitrogen doped graphene framework.

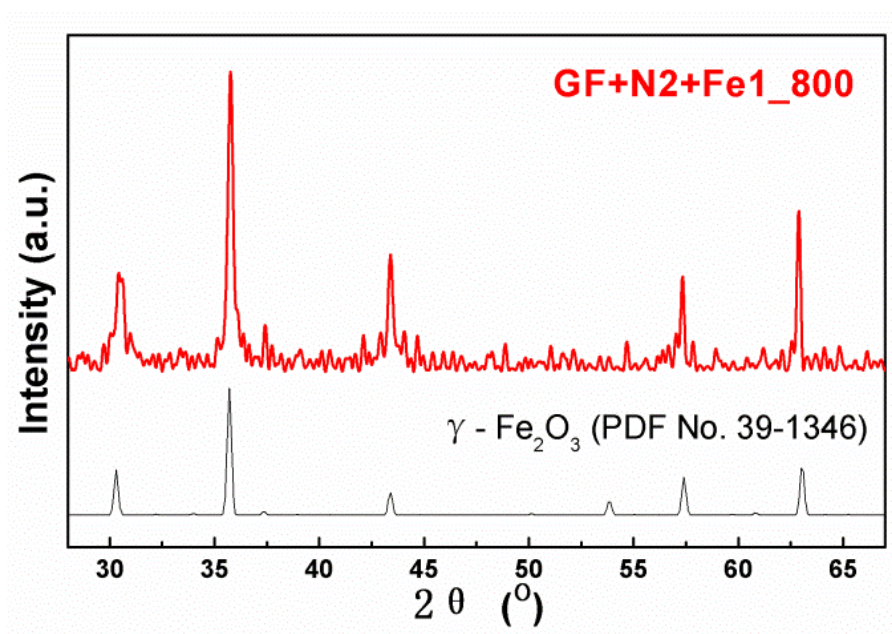


Figure 5-13. XRD pattern of GF+N2+Fe1_800, in comparison with the standard γ -Fe₂O₃ reference.

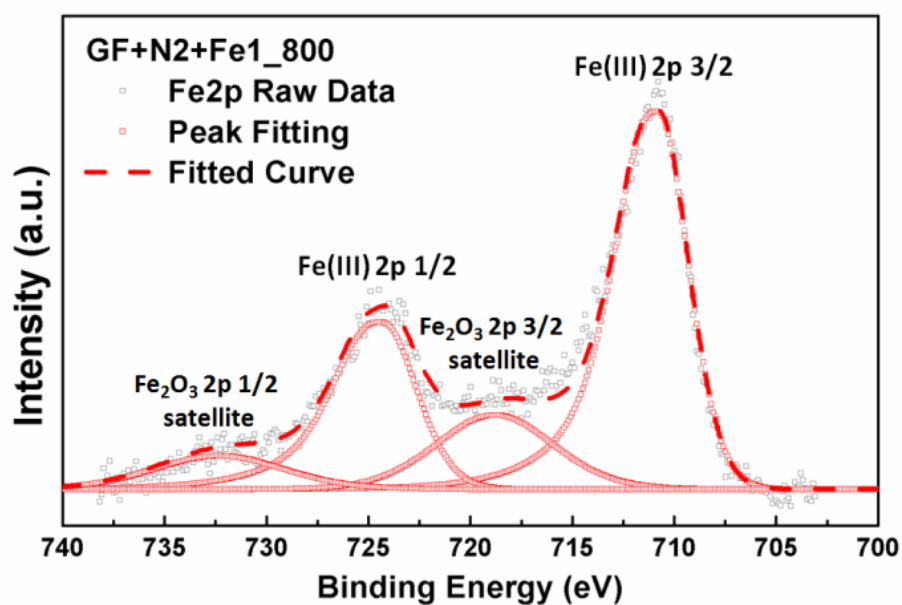


Figure 5-14. XPS Fe2p spectrum of GF+N2+Fe1_800.

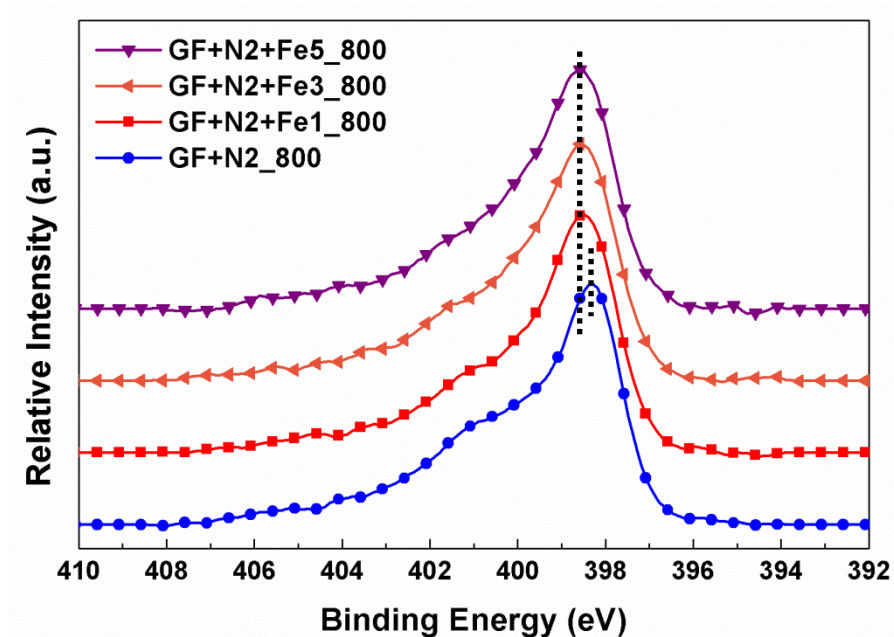


Figure 5-15. XPS N1s spectra of GF+N2+Fe_x_800.

The morphology of the γ -Fe₂O₃ nanoparticles were studied transmission electron microscopy (TEM), **Figures 5-16 and 5-17**. It is seen in the TEM image of GF+N2+Fe1_800 (**Figure 5-16**) that the γ -Fe₂O₃ nano-spheres with an average particle size of 2.6 ± 0.5 nm are uniformly dispersed over the nitrogen-doped graphene. The nano-particles in the high-resolution TEM image (**Figure 5-17**) display a d-spacing of ~ 2.5 Å, in well agreement with that of the (311) planes of the γ -Fe₂O₃ phase (corresponding to the XRD peak position at $2\theta = 35.4^\circ$, **Figure 5-13**).

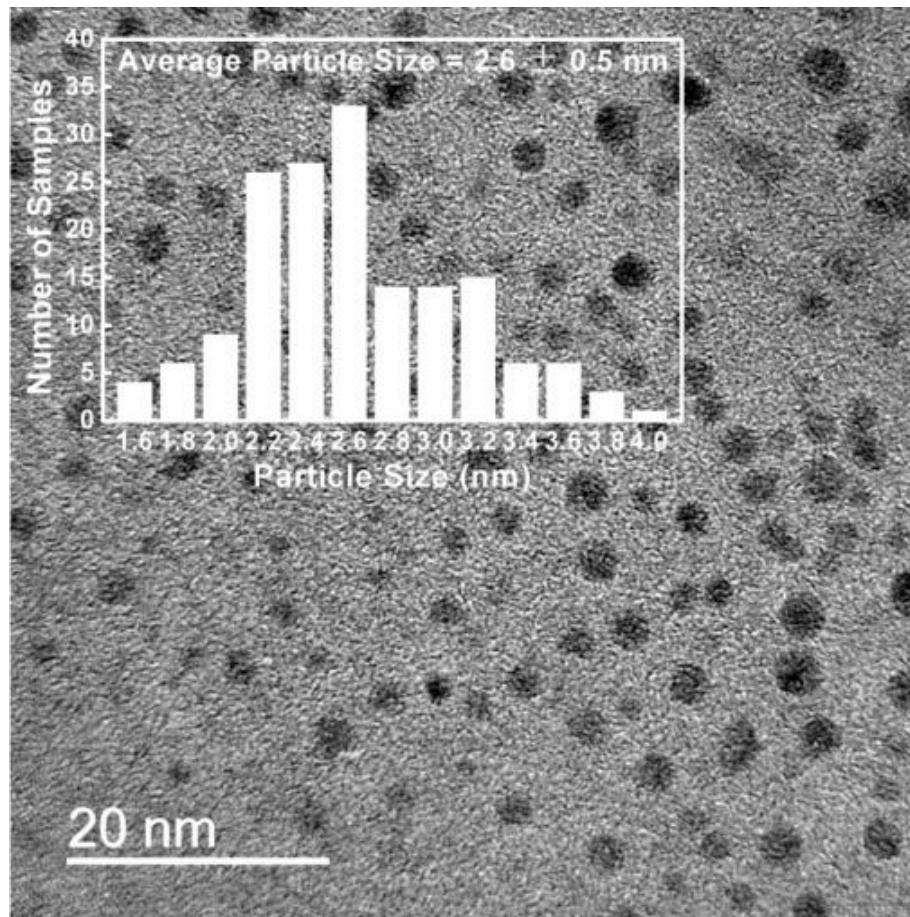


Figure 5-16. TEM image of GF+N2+Fe1_800. Insert is the particle size distribution of γ -Fe₂O₃.

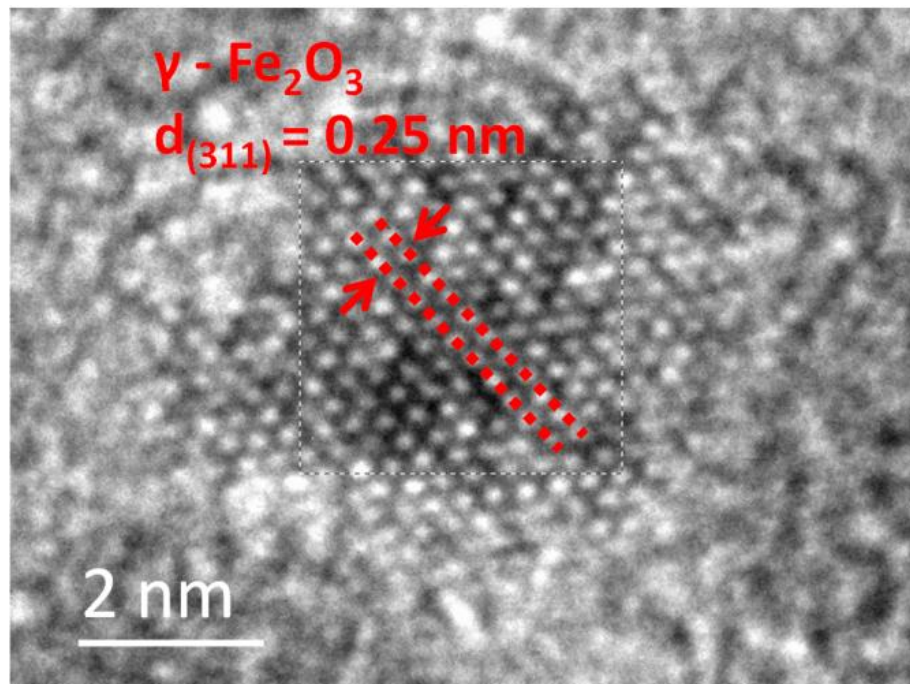


Figure 5-17. HRTEM image of GF+N2+Fe1_800.

5.2.3 Comparison of Catalytic Activities.

The catalytic ORR activities were studied through the linear sweep voltammetry (LSV) at 1600 RPM using the rotating disk electrode technique (RDE), **Figures 5-18 to 5-20**.

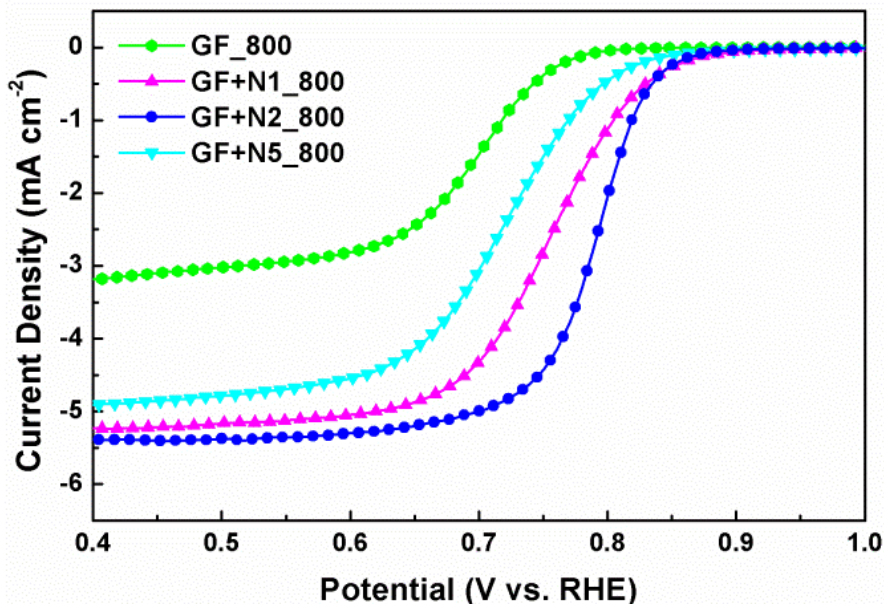


Figure 5-18. RDE LSV plots of GF+N₈₀₀ under 1600 RPM to demonstrate the effect of nitrogen precursor concentration for substrates.

The performance of different substrates was first compared, **Figure 5-18**, and it is seen that the onset reduction potentials of GF+N₈₀₀ are 70 – 100 mV higher than that of GF₈₀₀. In addition, the limiting current densities of GF+N1₈₀₀, GF+N2₈₀₀ and GF+N5₈₀₀ reach 5.24, 5.40, and 4.91 mA cm⁻² respectively, indicating a 4e⁻ transfer pathway; while GF₈₀₀ possess a value of 3.18 mA cm⁻², which is closer to the 2e⁻ pathway. The improved reduction potentials and 4e⁻ pathway selectivity of GF+N₈₀₀ demonstrate their better oxygen and peroxide adsorption capability derived from the nitrogen doping.²³⁴ Note that GF+N2₈₀₀ shows similar onset but superior half-wave reduction potential, compared with GF+N1₈₀₀, which should be attributed to the rapid

mass transfer as a result of the ultra-large pore volume of GF+N2_800. The slightly smaller onset potential and limiting current density of GF+N5_800 than those of the other two GF+N_800 is due to its lower conductivity (lower sp² carbon ratio, **Table 5-1**).

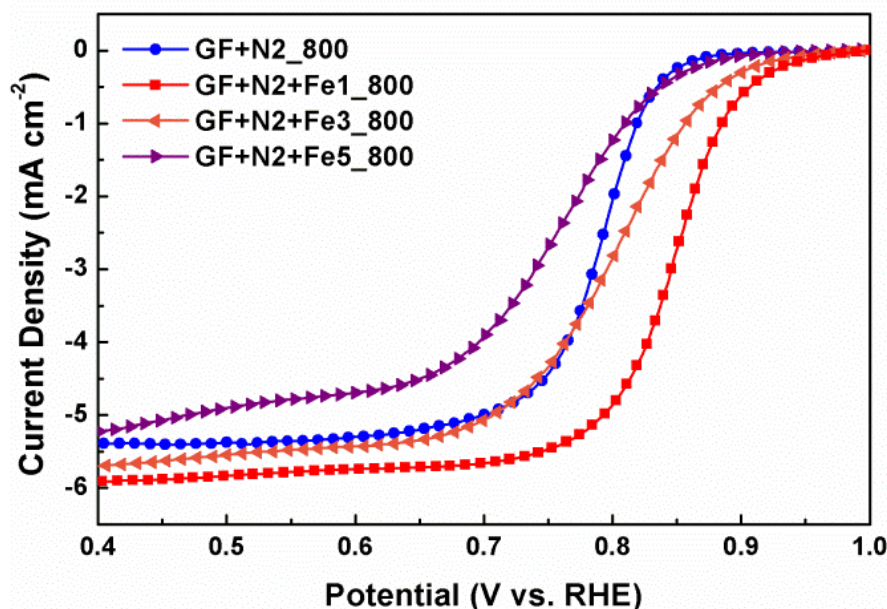


Figure 5-19. RDE LSV plots of GF+N2+Fe₈₀₀ under 1600 RPM to demonstrate the effect of iron precursor concentration on the optimised substrate.

The effect of γ -Fe₂O₃ loading ratio was then investigated by the confinement of three different concentrations of γ -Fe₂O₃ on the best substrate, GF+N2_800, **Figure 5-19**. The GF+N2+Fe1_800 shows a similar onset but much improved half-wave reduction potential, compared with the GF+N2+Fe3_800. This can be explained by the better mass transfer of GF+N2+Fe1_800, since the higher loading of γ -Fe₂O₃ affects more the overall porosity. A further increase of γ -Fe₂O₃ loading even reduces the onset potential (i.e. GF+N2+Fe5_800), suggesting that no more γ -Fe₂O₃ can be confined in the porous structure of GF+N2_800 and those extra one are merely attached on the surface. The almost identical gap between the onset and half-wave potential of GF+N2+Fe1_800

and GF+N2_800 demonstrates that nanoconfinement of controllable amount of NPMs into a hierarchical substrate causes affordable reduction of its porosity, leading to considerable improvement in reduction potential but negligible loss of its mass transfer capability.

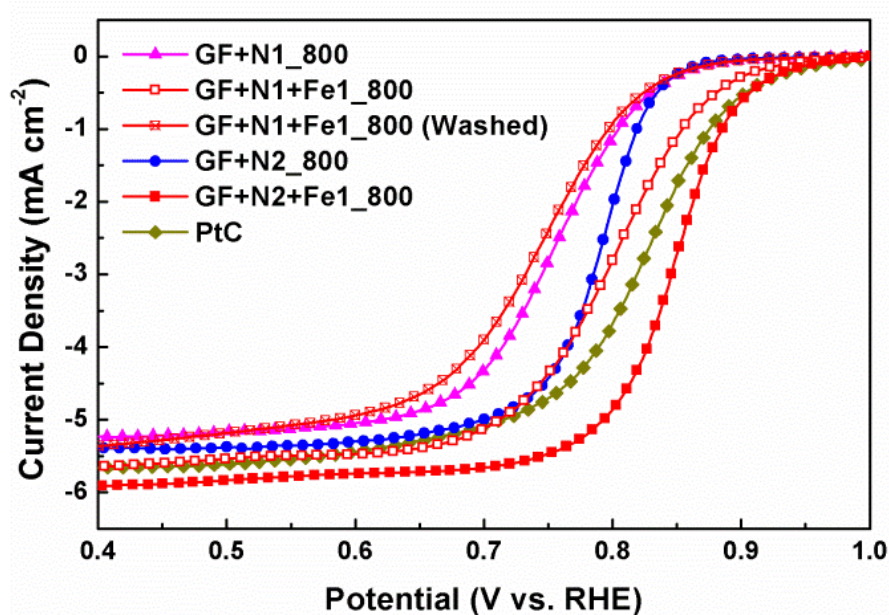


Figure 5-20. RDE LSV plots of GF+N+Fe₈₀₀ under 1600 RPM, in comparison with commercial PtC, to demonstrate the effect of substrates / NPMs.

To further demonstrate the significance of a pre-optimized hierarchically porous substrate, the optimal amount of γ -Fe₂O₃ was loaded into different substrates, **Figure 5-20**. It can be seen that the distinction between the ORR activities of GF+N2+Fe1₈₀₀ and GF+N1+Fe1₈₀₀ follows the same pattern between GF+N2₈₀₀ and GF+N1₈₀₀, revealing the enhancement in activity should be mainly because of the better substrate. Moreover, the similar performances between GF+N1+Fe1₈₀₀_W (γ -Fe₂O₃ is removed by acid washing) and GF+N1₈₀₀ prove that γ -Fe₂O₃ must be responsible for the better onset potential. As a result, the GF+N2+Fe1₈₀₀ obtained shows a higher reduction

potential than the commercial PtC (i.e. +27 mV at 3 mA cm⁻²).

All the GF+N_800, GF+N+Fe_800 and PtC unsurprisingly possess an electron transfer number (ETN) of 4 at 0.65V vs. RHE, calculated from the Koutecky-Levich (K-L) plot (**Figure 5-21**). However their kinetics current densities J_k at the same potential (also derived from the K-L plots) and the half-wave potential (V vs. RHE at 3 mA cm⁻²) are quite distinct (**Figure 5-22**), which is due to a combined effect of different porous substrates and γ -Fe₂O₃/Pt catalysts. Note that at 0.65V vs. RHE, not only the J_k of GF+N2+Fe1_800 (454.55 mA cm⁻²) is five times higher than that of PtC (71 mA cm⁻²), GF+N2+Fe3_800 (94.34 mA cm⁻²) and GF+N1+Fe1_800 (99.90 mA cm⁻²) can also surpass PtC at this potential, clearly pointing out the influence of rapid mass transfer achieved by a hierarchical substrate.

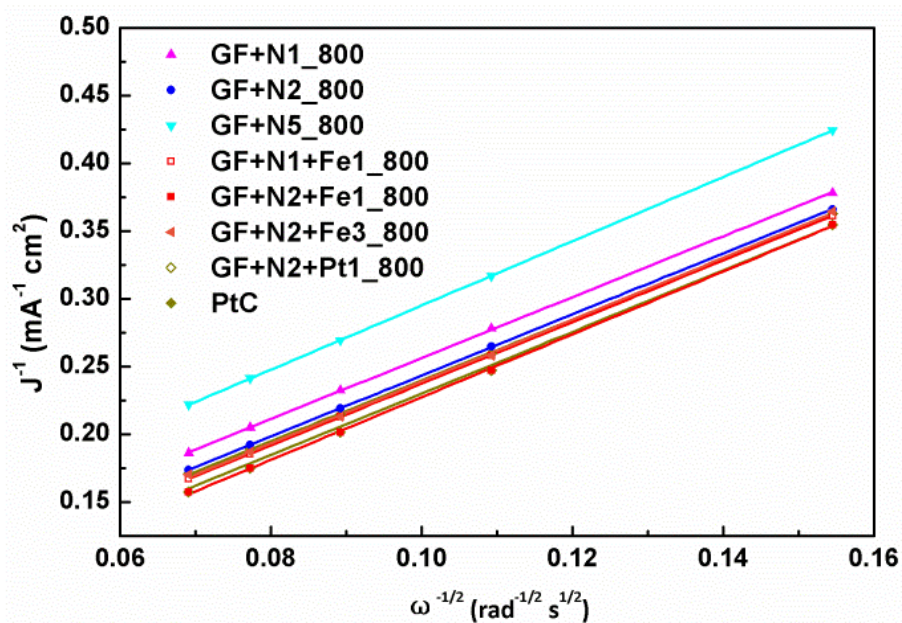


Figure 5-21. Comparison of K-L plots at 0.65 V vs. RHE.

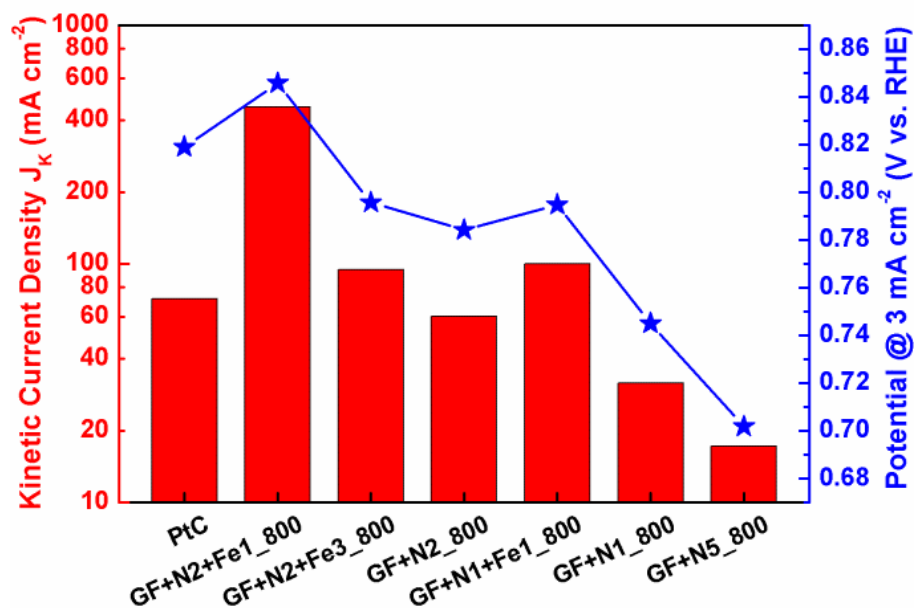


Figure 5-22. Comparison of kinetic current densities J_k at 0.65 V vs. RHE and reduction potentials at 3 mA cm⁻².

The Rotating Ring Disk Electrode (RRDE) technique was applied to investigate the reaction pathway of GF+N2+Fe1_800, **Figure 5-23**. As shown in the plot of peroxide formation ratio (**Figure 5-24**), a peak value of 4.57% is observed at 0.8 V vs. RHE, which is due to the oxide substructure of Pt surface and is characteristic of the out-sphere reaction for Pt in an alkaline electrolyte.^{28, 29} GF+N2+Fe1_800, however, forms much reduced amount of intermediate during ORR (i.e. 0.31% at 0.8 V vs. RHE), indicating that the embedded γ -Fe₂O₃ nanoparticles can effectively enhance the HO₂⁻ binding and thus feature an improved selectivity towards the associative 4e⁻ transfer pathway over the potential range of operation. The broad peak of peroxide formation of GF+N2_800 and GF+N2+Fe1_800, when potential is lower than 0.7 V vs. RHE, can be assigned to the reduction of specifically absorbed oxygen on substrate.

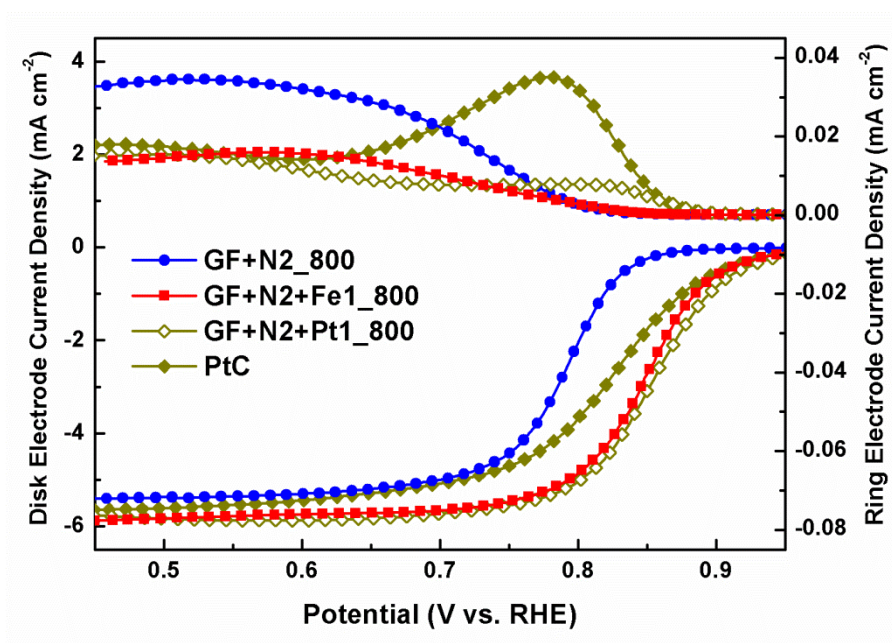


Figure 5-23. RRDE measurement of GF+N2_800, GF+N2+Fe1_800, GF+N2+Pt1_800 and PtC.

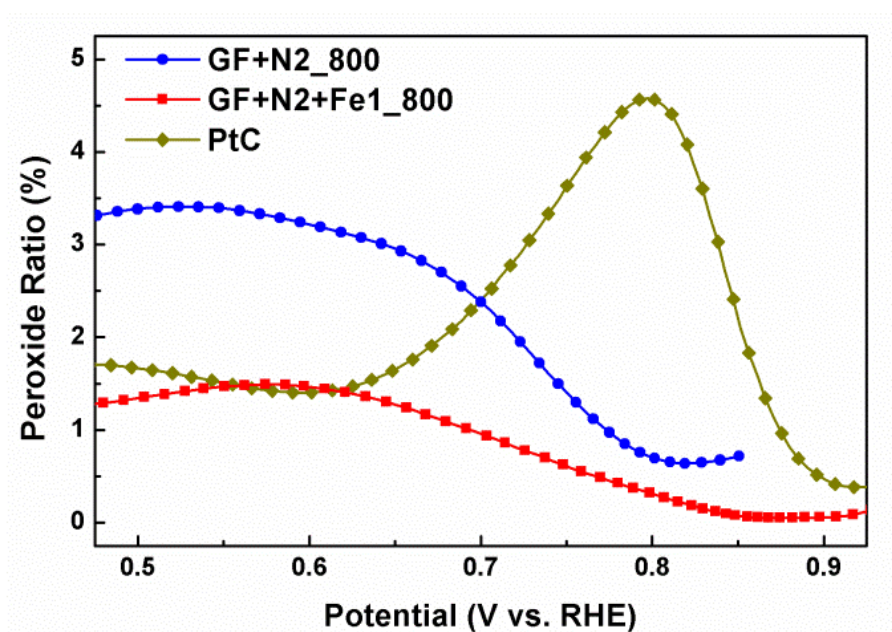


Figure 5-24. Peroxide formation ratios of GF+N2_800, GF+N2+Fe1_800 and PtC.

Based on the ETN values derived from RRDE measurement, the corresponding diffusion corrected kinetic current density (J_k) was calculated and presented in the Tafel plots (Figure 5-25). It is shown that the GF+N2+Fe1_800 possesses a similar onset

potential (i.e. J_K reaches 0.5 mA cm^{-2}) as PtC, but a much smaller Tafel slope (66.3 vs. 83.5 mV dec^{-1} for GF+N2+Fe1_800 and PtC), which results in a three times higher J_K than PtC at 0.8 V vs. RHE ($34.3 \text{ vs. } 10.96 \text{ mA cm}^{-2}$).

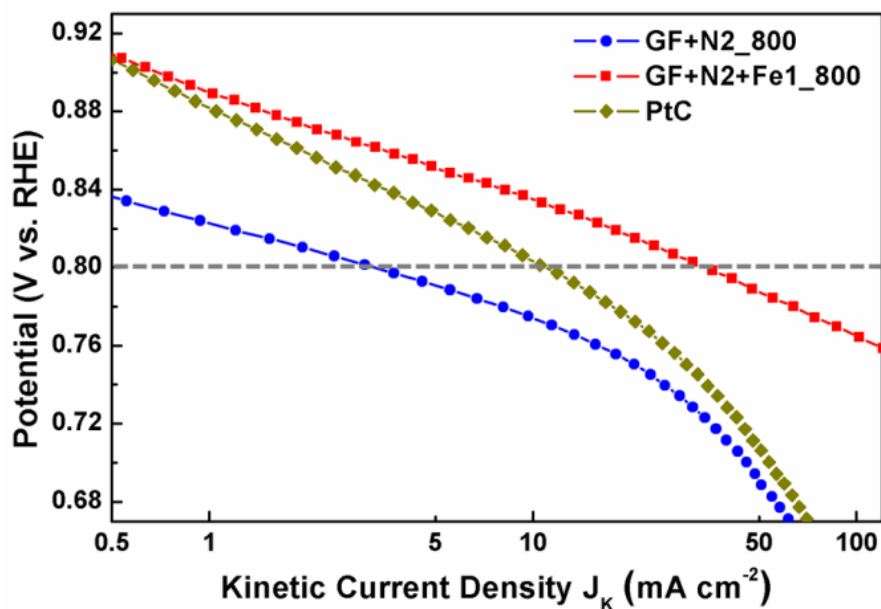


Figure 5-25. Tafel plots of GF+N2_800, GF+N2+Fe1_800 and PtC.

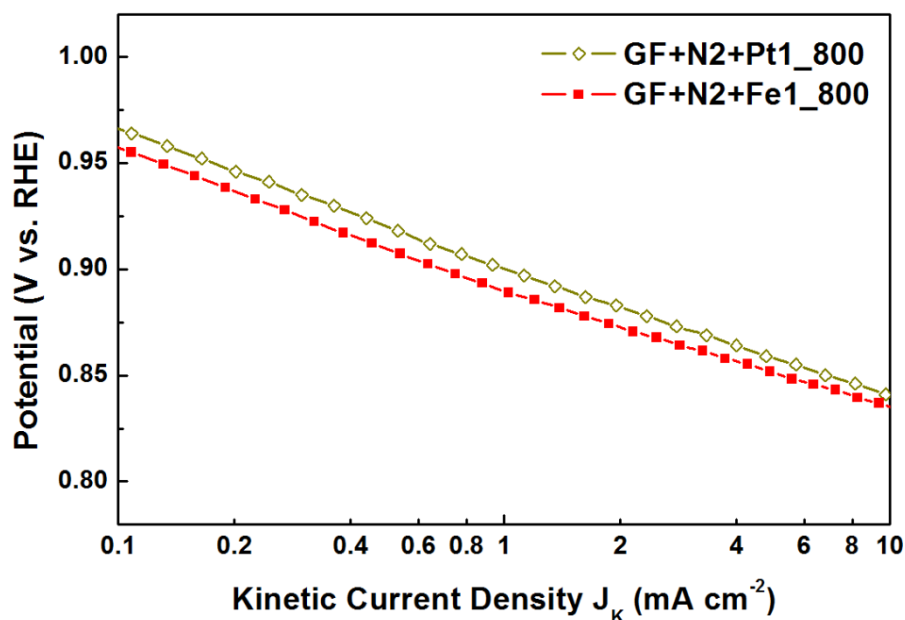


Figure 5-26. Tafel plots of GF+N2+Pt1_800 and GF+N2+Fe1_800, derived from Figure 5-23.

It is also noted in **Figure 5-26** that the Tafel plots of GF+N2+Fe1_800 and GF+N2+Pt1_800 (same synthesis route expect using a Pt precursor) are almost parallel, derived from the RRDE measurement in **Figure 5-23**, with a potential shift of less than 10 mV. Such an observation confirms that the superior ORR kinetics of GF+N2+Fe_800 is achieved by the combined effect of both γ -Fe₂O₃ with comparable oxygen adsorption capability to Pt and the hierarchically porous GF+N2_800 substrate with rapid mass transfer (Tafel slope of GF+N2_800 is only 47.9 mV dec⁻¹).

To further elucidate the ORR activity of GF+N2+Fe1_800, electrical impedance spectroscopy (EIS) was employed. The equivalent circuit of RDE (insert in **Figure 5-27**) consists of an uncompensated impedance (I_U) including (a) the resistance of the electrolyte R_E , and (b) the interface of RDE thin film (R_{TF}) partly reflecting the electrical conductivity of the catalysts; and also reaction related components (I_R) such as (c) the kinetics controlled process R_K and (d) the diffusion controlled process R_D of the catalytic oxygen reduction process. EIS is measured at the half-wave potential of each catalyst, since at this point, current density increases fastest and the overall impedance reaches its smallest value under a RDE system. Since the uncompensated impedance I_U is almost the same for each catalyst and thus is subtracted from the Nyquist plot (**Figure 5-27**). It is clearly seen that both kinetics (the first semi-circle) and diffusion (the second semi-circle) affect the ORR process at this potential (the mixed kinetic-diffusion region). As expected, GF+N2+Fe1_800 and GF+N2_800 possess similar overall impedance of 250 Ω , while PtC shows a much larger value of 360 Ω . It is also shown that GF+N2+Fe1_800 shows a R_K of ca. 120 Ω , slightly higher than that of GF+N2_800 (95 Ω), but smaller than the value of PtC (160 Ω). The order of R_K is in well agreement with

the trend in Tafel slope ($\text{GF+N}_2\text{_{800}} < \text{GF+N}_2\text{+Fe}_{1\text{_{800}}} < \text{PtC}$), further confirming that the confinement of a suitable amount of NPMs on a highly hierarchical substrate can large preserve its rapid mass transport.

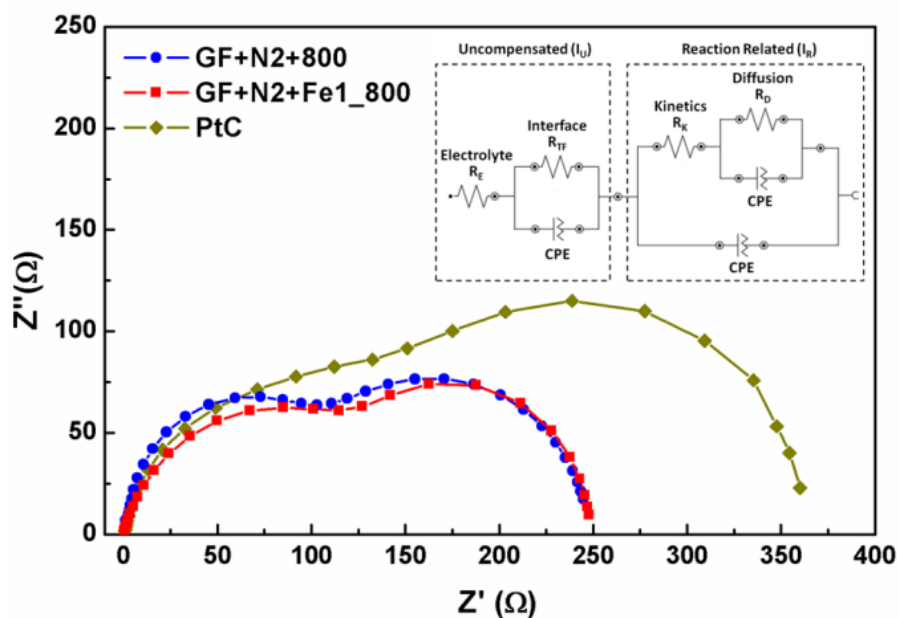


Figure 5-27. EIS Nyquist plots of GF+N₂_800, GF+N₂+Fe₁_800 and PtC.

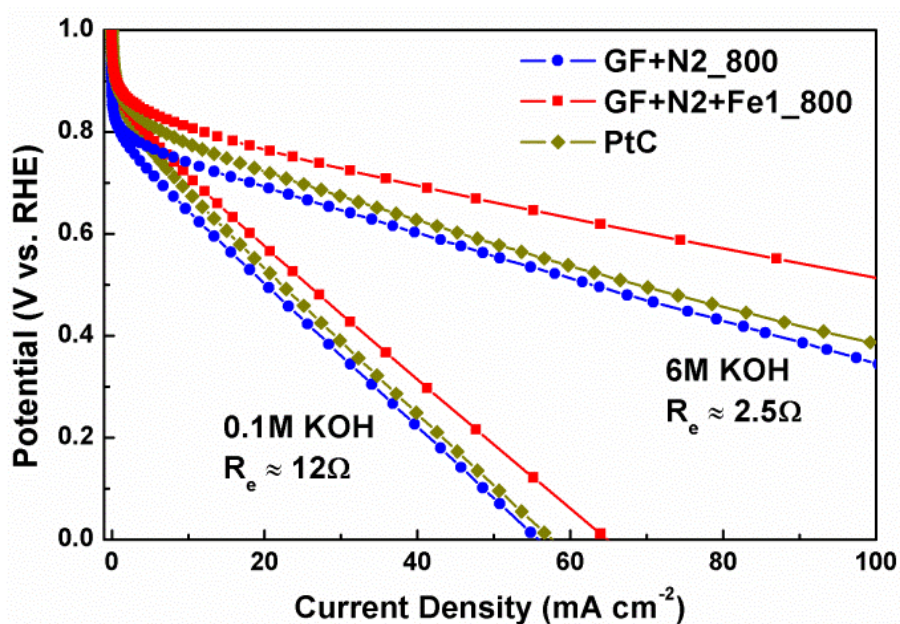


Figure 5-28. The electrode performance of GF+N₂_800, GF+N₂+Fe₁_800 and PtC in 0.1M and 6M KOH. Catalyst loading is 0.7 mg cm^{-2} .

The consistency of the superior ORR activity for GF+N2+Fe1_800 was verified by analysing its corresponding electrode performance through the polarization curves ($V-i$) in 0.1M and 6M KOH (**Figure 5-28**). It can be seen that the ORR catalytic activities follow the exactly the same trend, in spite of the fact that the internal impedance is significantly reduced after loading the catalysts on hydrophobic carbon paper and the resistance of the electrolyte decreases as the concentration of alkaline electrolyte increases (12 and 2.5 Ω for 0.1 and 6M KOH respectively).

The stability of GF+N2+Fe1_800 was evaluated using a chrono-amperometry method. The current response is measured under 1600 RPM and at the potential when the current density of GF+N2+Fe1_800 or PtC reaches 3 mA cm⁻². After 20 hours, the relative current of PtC drops ca. 25.2% while a small loss of 3.8% is observed for GF+N2+Fe1_800 (**Figure 5-29**). In addition, the durability of GF+N2+Fe1_800 was further assessed by cycling the catalysts between 0.2 and 1.2 V vs. RHE for 5000 cycles.^{14b,20} The LSV of GF+N2+Fe1_800 after the test shows a negligible shift of -3 mV for its half-wave potential at 1600 RPM (**Figure 5-30**). The excellent stability and durability of GF+N2+Fe1_800 should be ascribed to the successful confinement of γ -Fe₂O₃ into nitrogen doped graphene framework and the strong interaction between those two.¹⁵

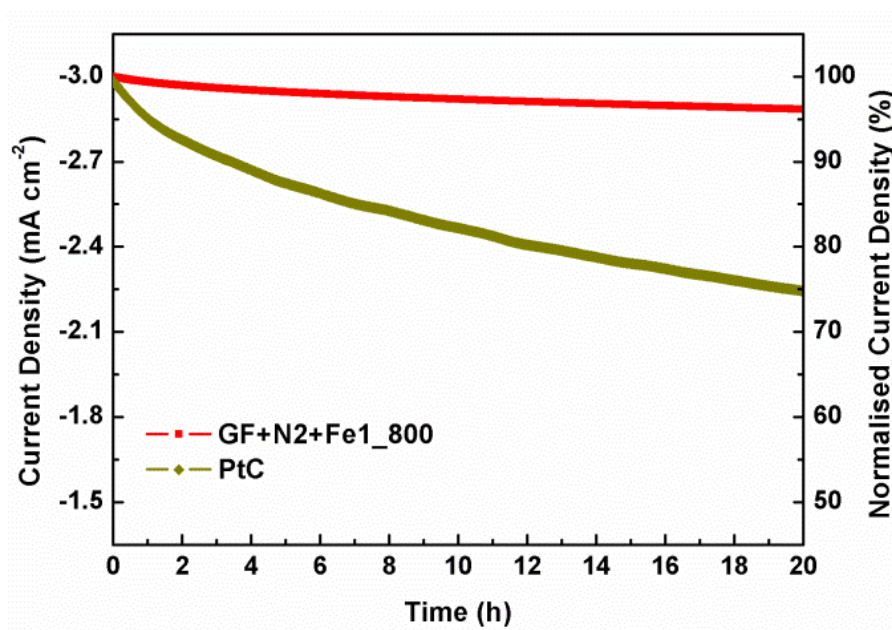


Figure 5-29. Chrono-amperometry of GF+N2+Fe1_800 and PtC in O₂-saturated 0.1M KOH, under 1600 RPM, at an initial ORR current of 3 mA cm⁻².

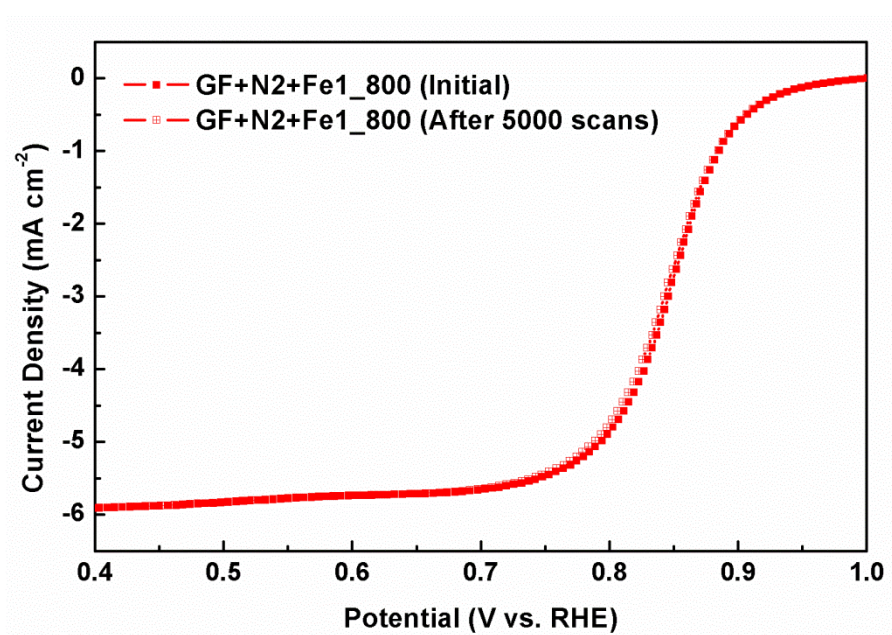


Figure 5-30. LSV of GF+N2+Fe1_800 before and after 5000 scans at 1600 RPM between 1.0 - 0.4 V vs. RHE, with a scan rate of 100 mV s⁻¹.

Finally, the activity of GF+N2+Fe1_800 is compared with other recently developed Fe based ORR catalysts in alkaline electrolyte.¹⁹³ The potentials of each catalyst at 0.5 and 3 mA cm⁻² (measured at 1600 RPM in RDE / RRDE) are plotted as the X- and Y- axis in **Figure 5-31**, and thus the gap between those two potentials of each catalyst (i.e. the intercept of red angled lines) can largely reflect its Tafel slope. It can be seen that, among more than 50 catalysts, only one of them²²⁸ shows a larger Tafel slope and two others^{229, 230} possess a higher potential at 3 mA cm⁻² than those of GF+N2+Fe1_800. This result clearly demonstrates that the ORR performance of GF+N2+Fe1_800 is among the best of existing Fe based ORR catalyst, despite the type of Fe-based active site has NOT been fully optimized yet.

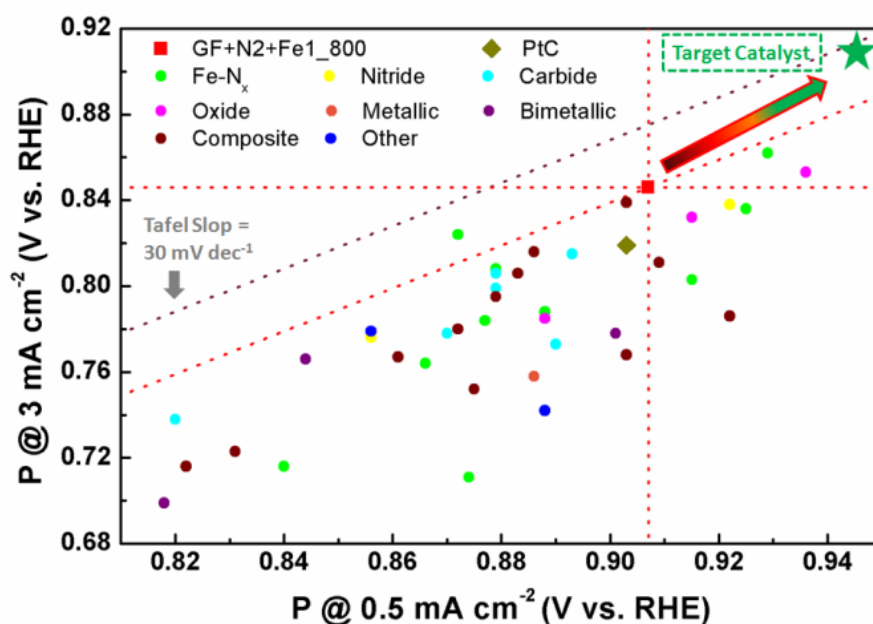


Figure 5-31. Comparison of the ORR potentials at the current densities of 0.5 and 3 mA cm⁻² for GF+N2+Fe1_800, PtC, and other recently reported Fe-based catalysts, measured by RDE under 1600 RPM.¹⁹³ Two slanting dash-lines reflect the Tafel slopes of GF+N2+Fe1_800 or the lowest theoretical limit value of 30 mV dec⁻¹.

5.3 Summary

A two-step design approach is suggested and implemented to achieve a highly efficient graphene supported NPM catalysts for ORR, nanoconfined maghemite in a hierarchical nitrogen-doped graphene framework, which outperforms the commercial PtC in an alkaline electrolyte. The scheme ensures that the hierarchical porosity of the substrate is generated and optimized first, to enhance the pore volume for rapid mass transfer; and then an appropriate amount of active NPM catalysts is introduced to the optimized substrate to enhance oxygen adsorption and inhibit intermediate peroxide formation, with little compromise of the overall mass transfer capability.

Due to a combined effect of the highly porous substrate and the active $\gamma\text{-Fe}_2\text{O}_3$ sites, the GF+N2+Fe1_800 displays superior performance to the commercial PtC, including a higher half-wave reduction potential, better $4e^-$ pathway selectivity, smaller Tafel slope, faster kinetic current density and longer lifetime. The superior activities of the GF+N2+Fe1_800 (also comparable with the Pt counterpart, GF+N2+Pt1_800) suggest the wide applicability of the above design principle and the great potential of developing cost-effective and durable $\gamma\text{-Fe}_2\text{O}_3$ based catalysts.

Chapter 6. Phosphorus / Nitrogen Co-doped Graphene Framework

6.1 Introduction

Excellent bifunctional catalytic activity requires ORR and OER overpotentials to be reduced simultaneously, which is very challenging to achieve since the optimal substrate-intermediate binding energies for the 'minimal' ORR / OER overpotentials are usually different on any given individual catalytic sites, due to the scaling relations among adsorption energies of the key reaction intermediates. Hence, one feasible strategy is to design catalysts containing two different types of active sites with the respective desirable substrate-intermediate binding energies for ORR / OER. Heteroatom-doped graphene can offer huge flexibility in accurate engineering of targeted catalytic sites, thus allowing them to be likely candidates for this purpose.

Phosphorus and nitrogen co-doped carbons have been recently reported to exhibit bifunctional ORR and OER activities, but the corresponding active sites are unclear. Note that the N-doping has been determined to promote the electron donation from the catalyst to the O₂ molecule, facilitating ORR, while the role of P-doping remains little understood. To address this issue, a large number of P-doping or P,N co-doping structures have been computationally screened by my colleague, Guo-Liang Chai, to theoretically identify the most promising ones for ORR or OER, **Figure 6-1**. Typically, the simulation process includes an initial short-listing of stable structures, calculation of

electronic property for possible active sites, and finally estimation of O₂ adsorption / desorption kinetic barriers and thermodynamic limiting potentials.

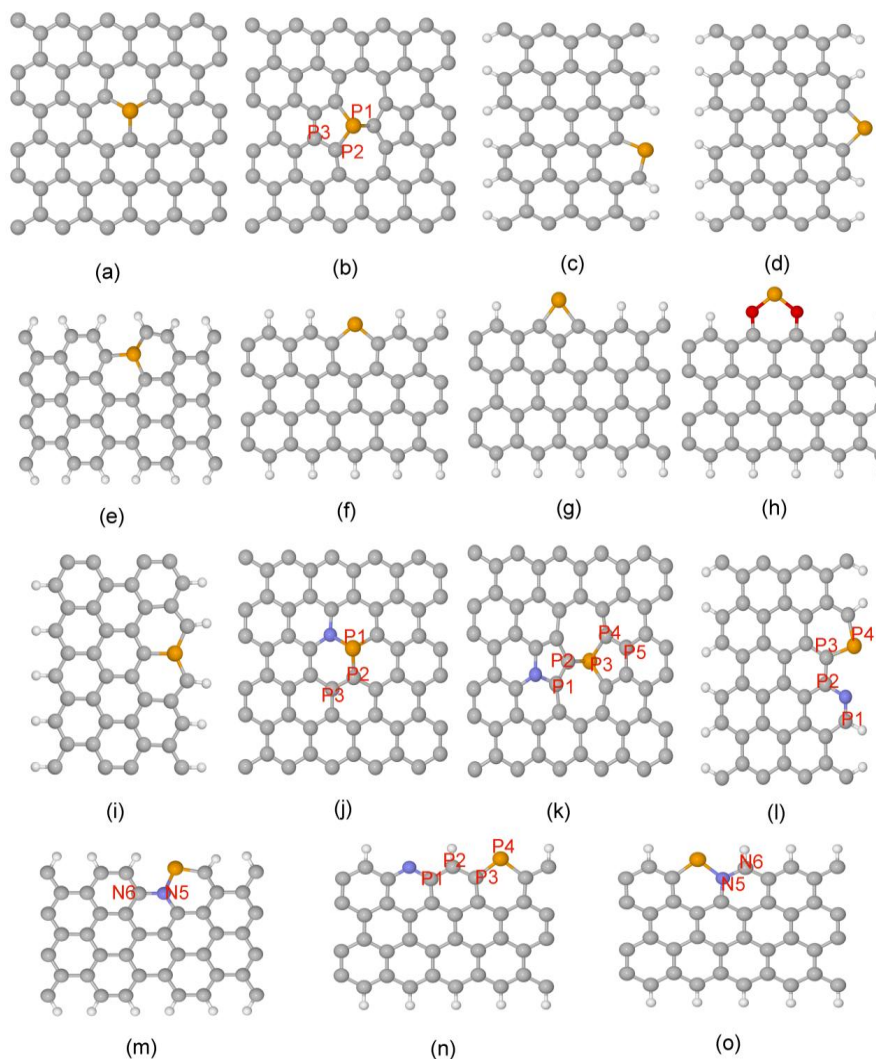


Figure 6-1. The structures of (a) G-P-1; (b) SW-P-1, SW-P-2, and SW-P-3; (c) A-P-1; (d) A-P-2; (e) A-P-3; (f) Z-P-1; (g) Z-P-2; (h) Z-P-3; (i) Z-P-4; (j) G-PN-1, G-PN-2, and G-PN-3; (k) SW-PN-1, SW-PN-2, SW-PN-3, SW-PN-4, and SW-PN-5; (l) A-PN-1, A-PN-2, A-PN-3, and A-PN-4; (m) A-PN-5 and A-PN-6; (n) Z-PN-1, Z-PN-2, Z-PN-3, and Z-PN-4; (o) Z-PN-5 and Z-PN-6. The white, grey, blue, red, and brown spheres denotes for H, C, N, O, and P atoms. The “A”, and “Z”, stand for Armchair and Zigzag edges, respectively. The “G” and “SW” denote for perfect and Stone-Wales defected graphene, respectively.

Modelling results show that an oxidised P,N co-doped local structure (Z-PN-5-OX2, **Figure 6-2a**) is particularly favourable for OER, while the formerly reported Stone-Wales N-containing structure (**Figure 6-2b**) still possesses a better ORR activity than any P-doping or P,N co-doping structures screened. The calculated OER and ORR limiting potentials of the above two structures are 1.68 and 0.8 V, **Figure 6-3**, which are roughly comparable to the experimentally measured OER / ORR potentials at the current densities of 10 or 3 mA cm⁻² by rotating disk electrode under 1600 RPM.

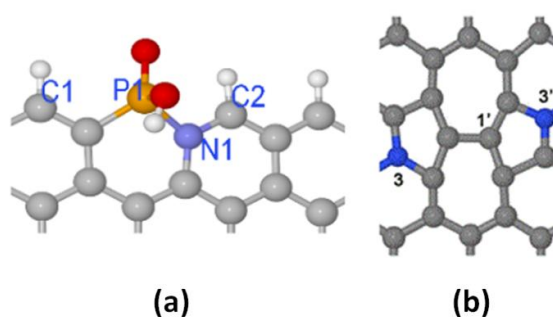


Figure 6-2. The structures of (a) Z-PN-5-OX2 and (b) Stone-Wales N-doping. The “Z” refers to zigzag edges, and the “OX2” indicates an oxidised structure. The white, grey, blue, red, and brown spheres denote for H, C, N, O, and P atoms.

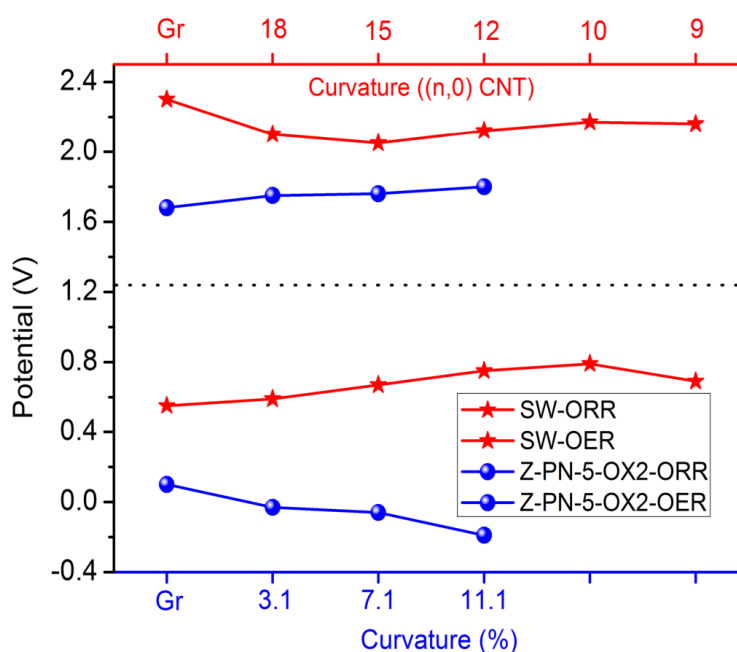


Figure 6-3. ORR / OER limiting potentials for Z-NP-5-OX2 and Stone-Wales defect structures.

Here in this chapter, I first experimentally formulated the P-N bond, together with the graphitic and pyridinic N (the major components of Stone-Wales N-doping structures), into P,N co-doped graphene frameworks (PNGF), so as to validate the computational predictions. After the proof-of-concept, I further intensified the concentration of P,N- and N-containing OER / ORR catalytic sites to promote the bifunctional activity of PNGF. The P,N co-doped graphene frameworks were prepared via a one-pot hydrothermal reaction using graphene oxide as the carbon source, and diammonium phosphate (DAP) or ammonium dihydrogen phosphate (ADP) as the phosphorus and nitrogen precursor, followed by freeze-drying and with / without high-temperature calcinations, as detailed in **Section 3.1.3**. The samples achieved were named as PNGF, with the suffix of ‘_DAP’ or ‘_ADP’ and w/o the suffix of ‘_800’, according to the specific synthesis conditions.

6.2 Results and Discussion

The X-ray photoelectron spectroscopy (XPS) P2p spectrum of the synthesized P,N co-doped sample PNGF_DAP, **Figure 6-4**, demonstrates the existence of the P-N bond (ca. 133.7 eV) apart from the P-O (ca. 134.2 eV) and P-C (ca. 133.2 eV) bonds; the P-N bond however has been completely removed in the PNGF_DAP_800 sample after the high temperature calcination. In addition, the peak values of the XPS P2p spectra are ca. 133.7 and 133.4 eV for the PNGF_DAP and the PNGF_DAP_800, respectively, in good agreement with the simulated Z-PN-5-OX2 structure of 133.45 eV.

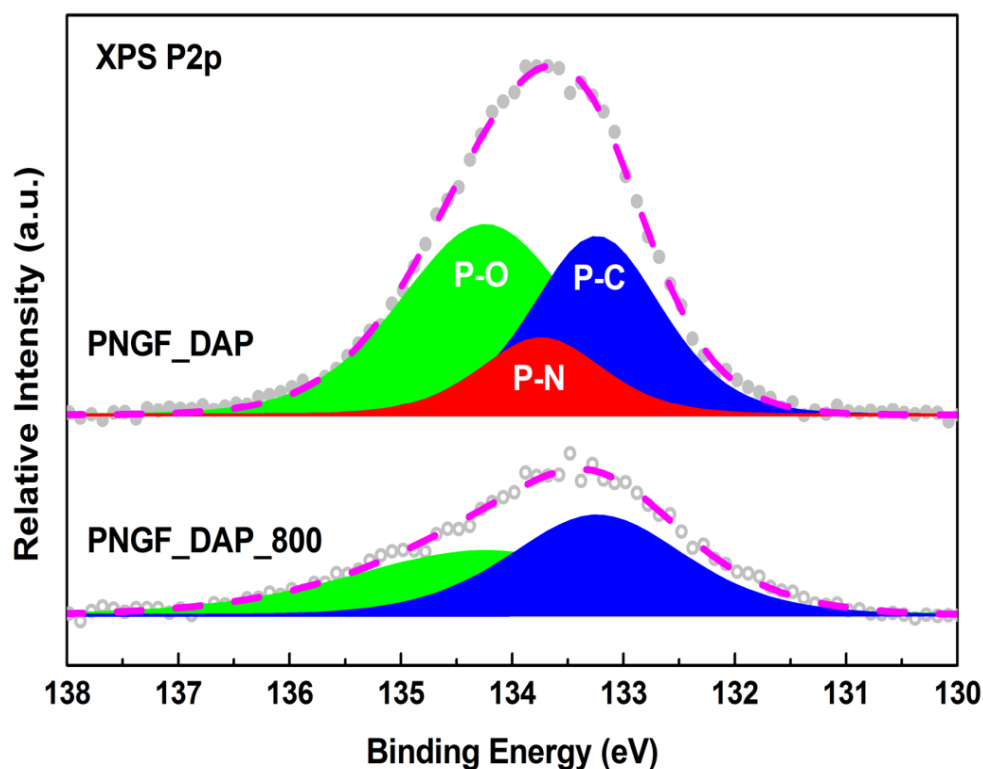


Figure 6-4. XPS P2p spectra for PNGF_DAP and PNGF_DAP_800.

At the same time, the XPS N1s spectra, **Figure 6-5** indicate that the amount of pyridinic nitrogen (6-N, ca. 398.2 eV) in the PNGF_DAP can be largely preserved after the thermal treatment at 800 °C, but the amount of graphitic nitrogen (g-N, ca. 401.2 eV) and amine (-NH₂, ca. 399.6 eV) groups has been significantly reduced in the PNGF_DAP_800. It is worth noting that the amount of graphitic nitrogen loss in PNGF_DAP_800 calculated from its XPS N1s spectrum is almost identical with the level of P-N bonds in PNGF_DAP (which will be totally eliminated in PNGF_DAP_800). Such an observation further supports the existence of P-N bonds in PNGF_DAP, since the Z-PN-5-OX2 structure is supposed to be thermally instable at high temperature of 800°C as well.

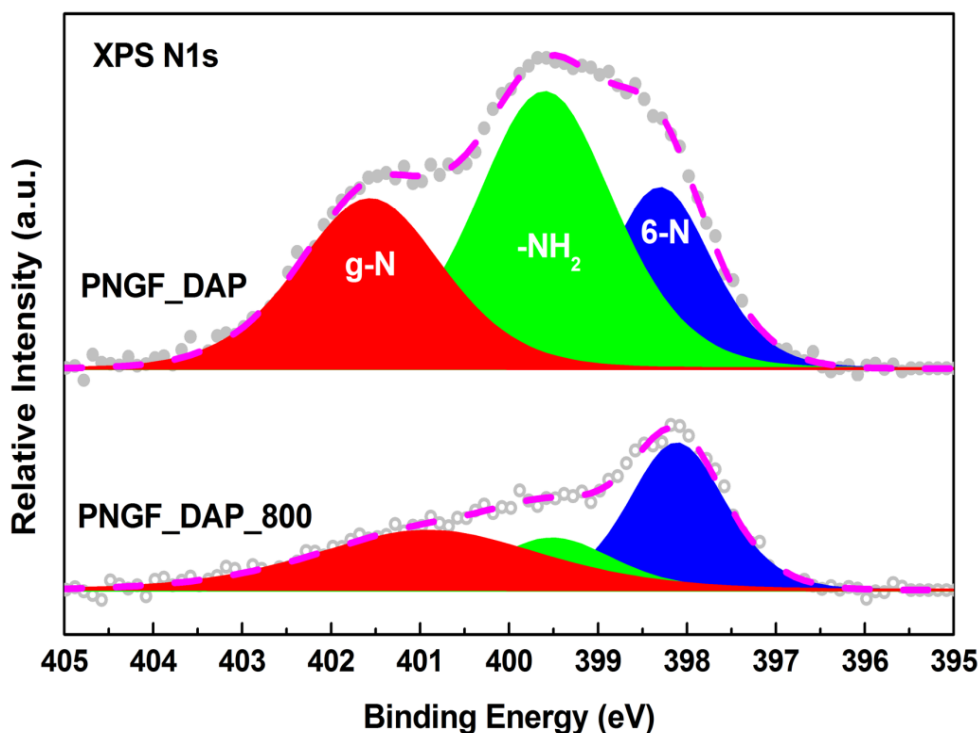


Figure 6-5. XPS N1s spectra for PNGF_DAP and PNGF_DAP_800.

As seen in **Figure 6-6** the PNGF_DAP shows a superior OER activity to its high-temperature calcined counterpart, and its ORR and OER potential gap at any given current is also significantly smaller than that of PNGF_DAP_800 (i.e. > 200 mV difference at 2 mA cm⁻²), although the latter shows slightly better reduction potential and current in ORR. It is worth noting that the electron transfer number (ETN or "n") during ORR at 0.6 V vs. RHE increases from 3.03 for the PNGF_DAP to 3.75 for the PNGF_DAP_800, **Figure 6-7**, indicating an enhanced selectivity towards the ORR associative 4e⁻ transfer pathway after thermal treatment. ETN is calculated from the respective LSV plots using the K-L equation, **Figures 6-8 to 6-10**. The enhanced ETN of PNGF_DAP_800 could be attributed to the fact that the -NH₂ group is more favourable for a 2e⁻ pathway, which can be easily formed when using DAP as precursors; and thus the removal of -NH₂ group in the PNGF_DAP_800 after high

temperature calcination should lead to a better selectivity in the $4e^-$ pathway. Through the above analysis, it is reasonable to state that the existence of P-N bond in PNGF is favourable for OER but not ORR, which is in good agreement with the calculated performance of the PN structure. The ORR activity of P,N co-doped metal-free catalysts should still be dominated by the nitrogen doping (i.e. graphitic and pyridinic N). In this case, it is imperative to deliberately tune the phosphorous and nitrogen binding configurations of PNGF so as to achieve the optimized bifunctionality.

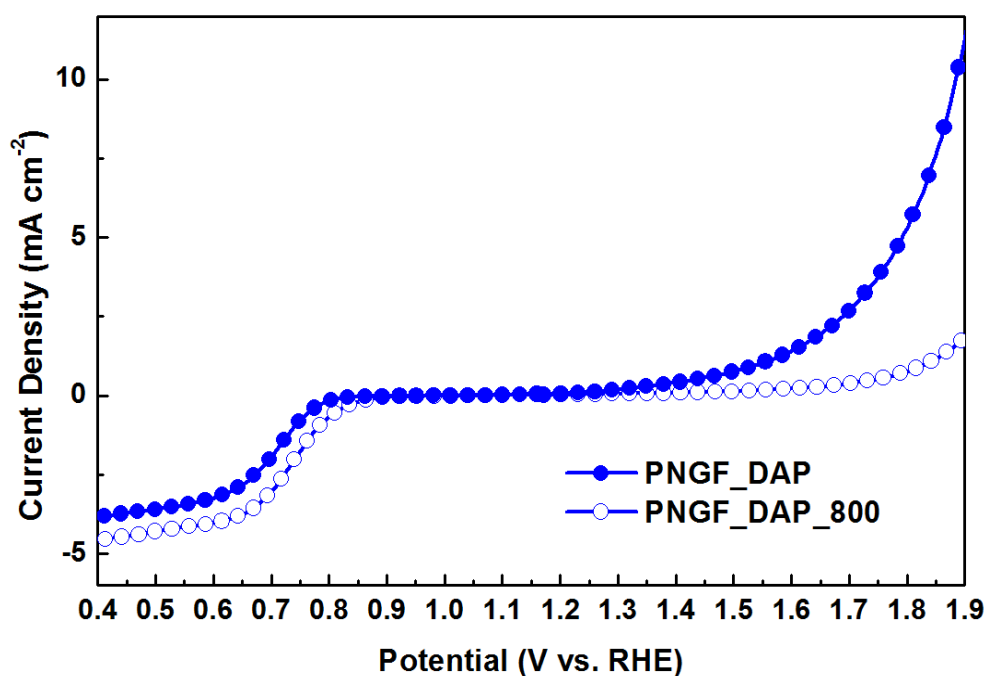


Figure 6-6. Bifunctional ORR / OER activities of PNGA_DAP and PNGF_DAP_800.

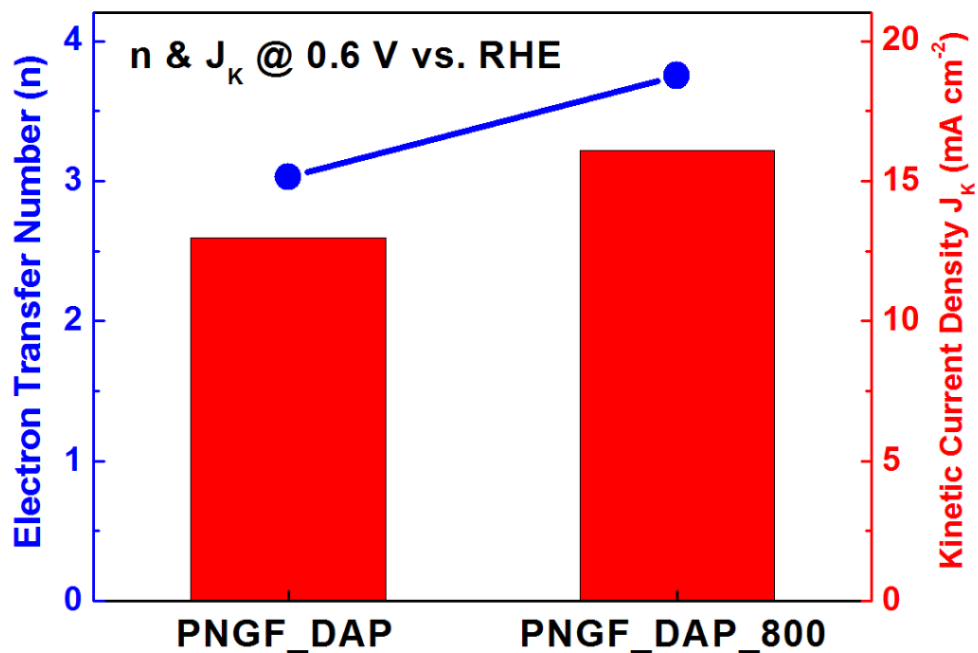


Figure 6-7. Electron transfer number and kinetic current density for ORR at 0.6 V vs. RHE.

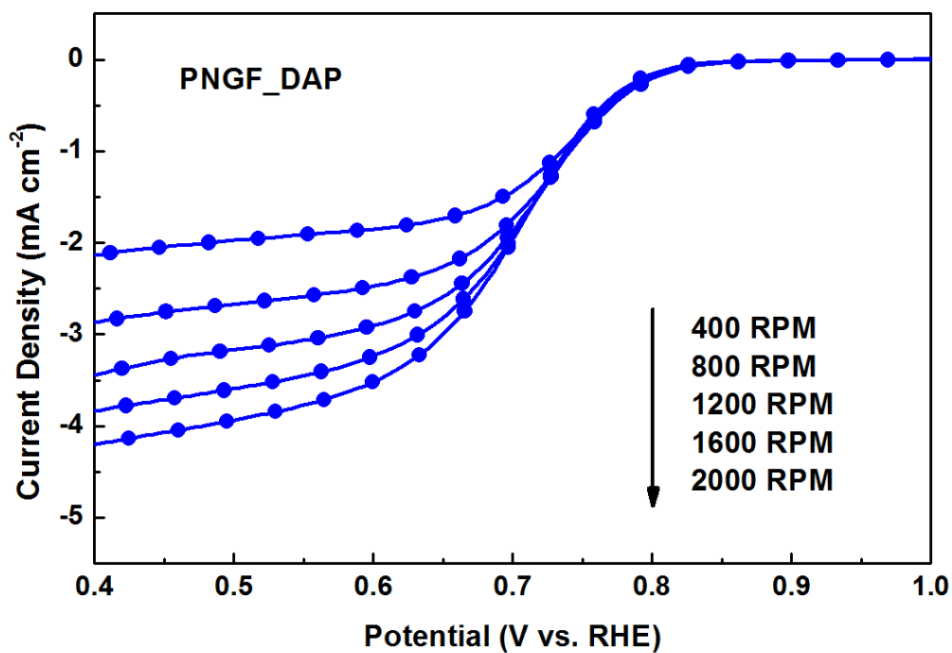


Figure 6-8. ORR LSV for PNGF_DAP in 0.1M O_2 -saturated KOH.

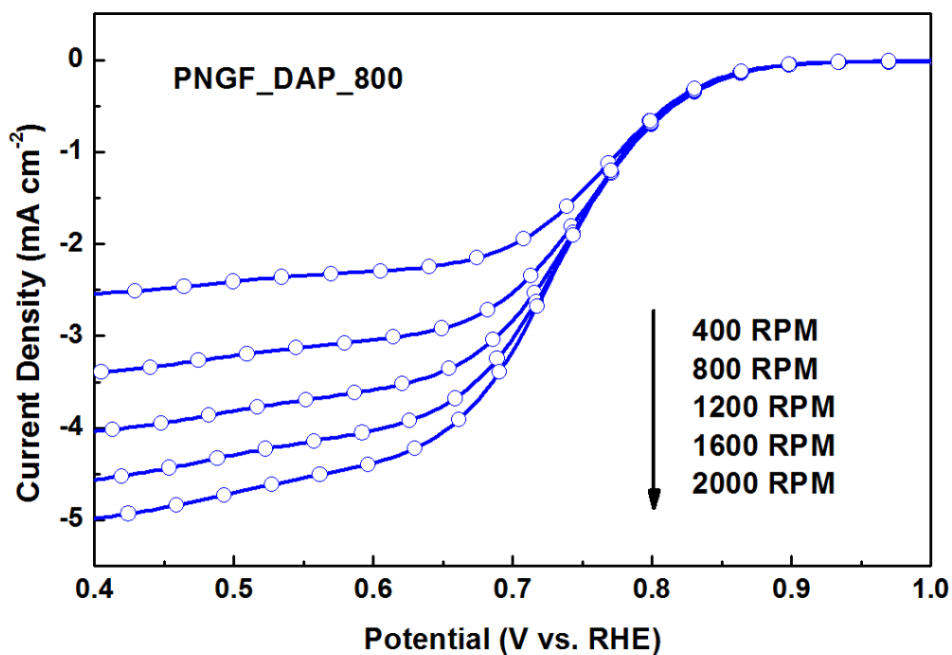


Figure 6-9. ORR LSV for PNGF_DAP_800 in 0.1M O₂-saturated KOH.

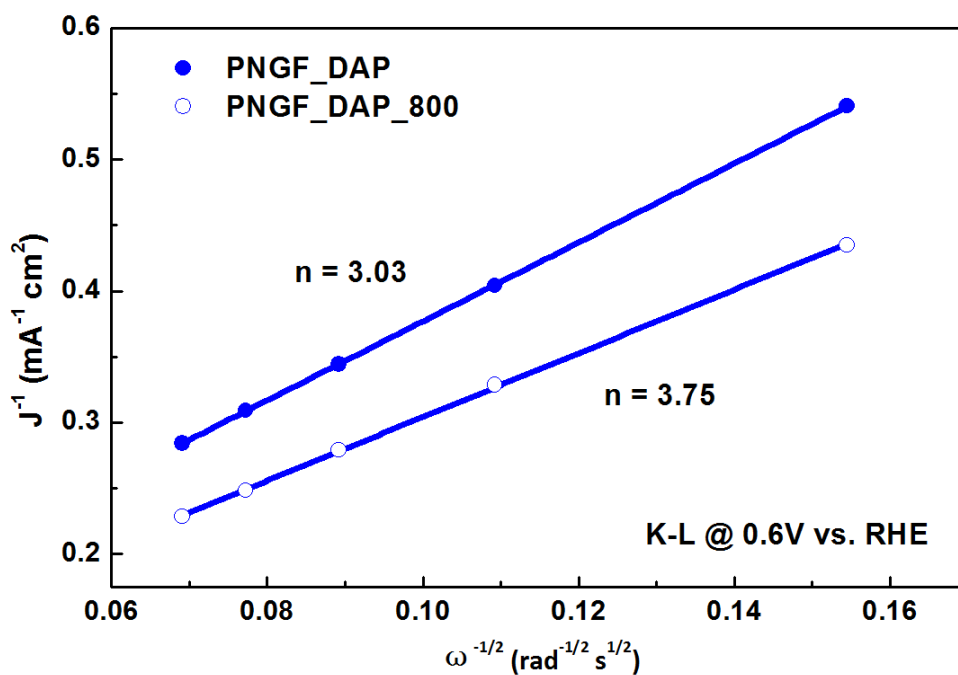


Figure 6-10. Koutecky-Levich plots of PNGF_DAP and PNGF_DAP(op) at 0.6 V vs. RHE.

Based on the above findings on the correlation between P/N binding configurations and ORR / OER activities, the key principle of optimizing the bifunctionality is to increase the

amounts of P-N bonds and graphitic / pyridinic N, respectively, while reduce the amount of -NH_2 . To further validate this notion, the previous P/N precursor, DAP, was replaced by ADP; the latter possesses a more balanced P/N ratio of 1:1 and may promote the formation of P-N bonds and prevent the formation of -NH_2 . In addition, the concentration of ADP precursor was further optimized as well and the obtained sample was named as PNGF_ADP(op). It has been confirmed by XPS (**Figures 6-11 and 6-12**) that the relative ratio of P-N bonds can rise to more than 50% in the optimal sample, PNGF_ADP(op), more than three times of that of PNGF_DAP, while the relative ratio of -NH_2 in PNGF_ADP(op) was effectively reduced by 50%, compared with PNGF_DAP.

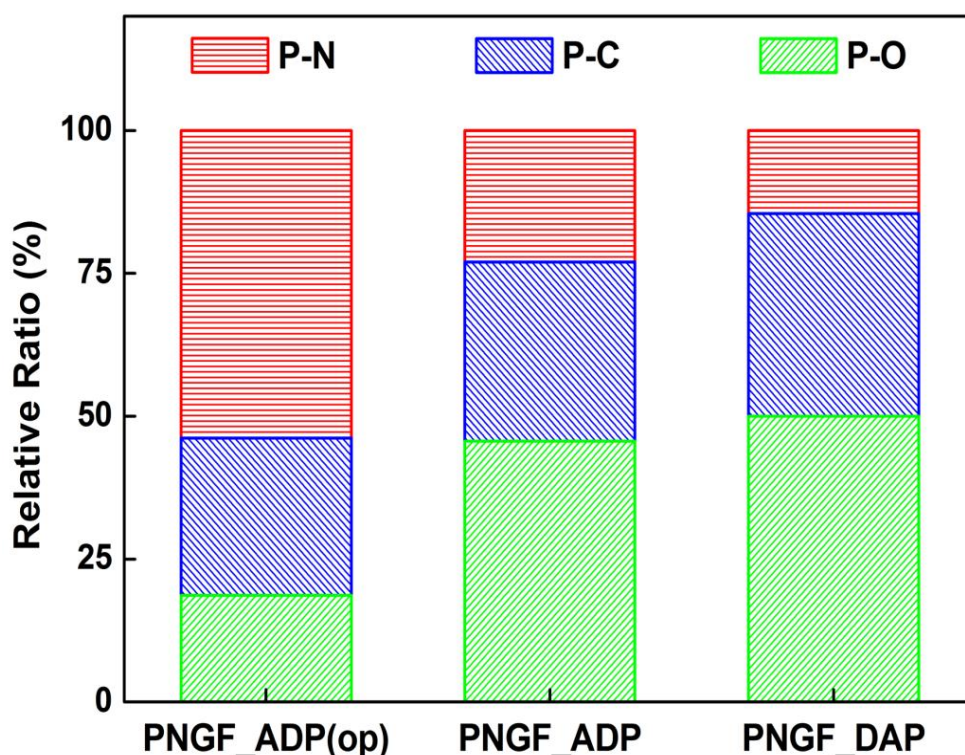


Figure 6-11. Relative ratio of P-N, P-C and P-O bonds in PNGF_DAP, PNGF_ADP and PNGF_ADP(op), derived from XPS P2p binding configurations in **Figure 6-18**.

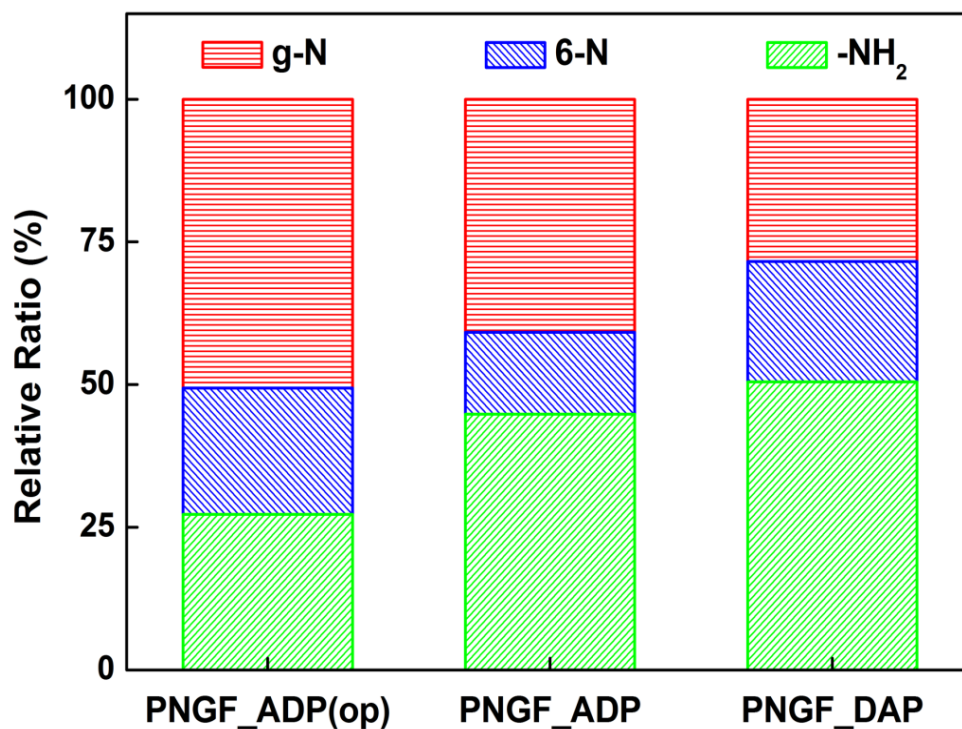


Figure 6-12. Relative ratio of g-N, 6-N and -NH₂ bonds in PNGF_DAP, PNGF_ADAP and PNGF_ADAP(op), derived from XPS N1s binding configurations in **Figure 6-13**.

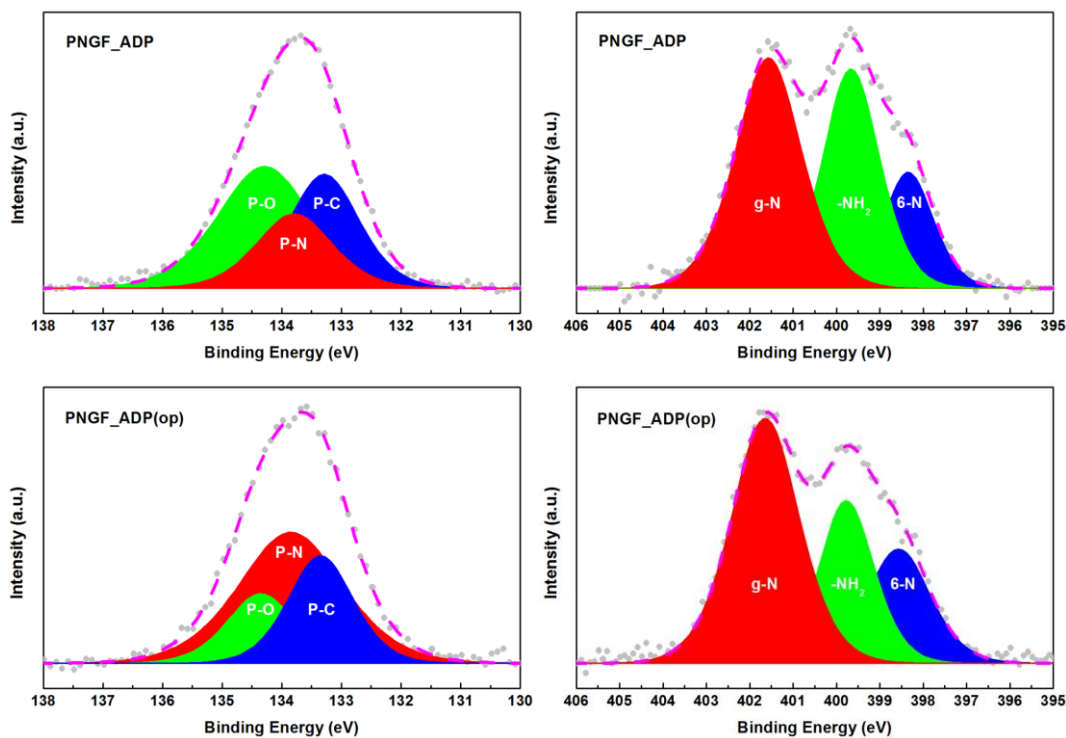


Figure 6-13. XPS P2p and N1s spectra for PNGF_ADAP and PNGF_ADAP(op).

As a result, it is demonstrated in **Figure 6-14** that the potential gap between 3 and 10 mA cm⁻² for ORR / OER, respectively, was reduced from 1,252 mV for PNGF_DAP, to 1,037 mV for PNGF_ADAP, and further to 795 mV for PNGF_ADAP(op). It is worth noting that the OER current density of the PNGF-based catalysts varies exponentially with the level of P-N bonds (alternatively, the logarithm of OER current and the amount of P-N bond are in a positive linear relationship, as shown in **Figure 6-15**). The OER Tafel slope can be greatly reduced from 344 to 143 mV dec⁻¹ (**Figure 6-16**) as the PN concentration increases from ca. 0.43 to 1.00 at%.

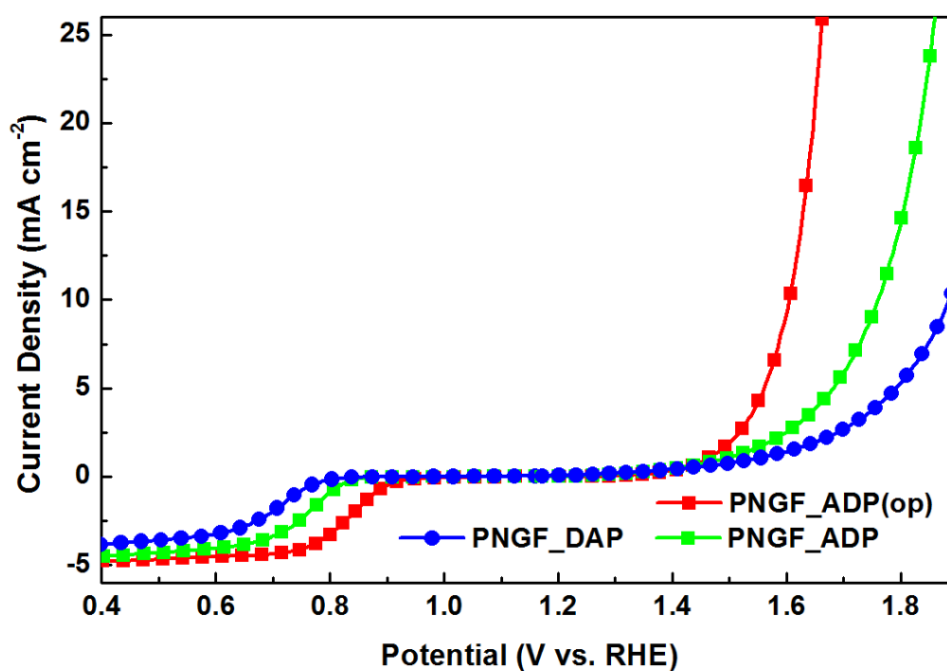


Figure 6-14. ORR / OER bifunctional activities of PNGF_DAP, PNGF_ADAP and PNGF_ADAP(op), measured by RDE at 1600 RPM, in 0.1M O₂-saturated KOH.

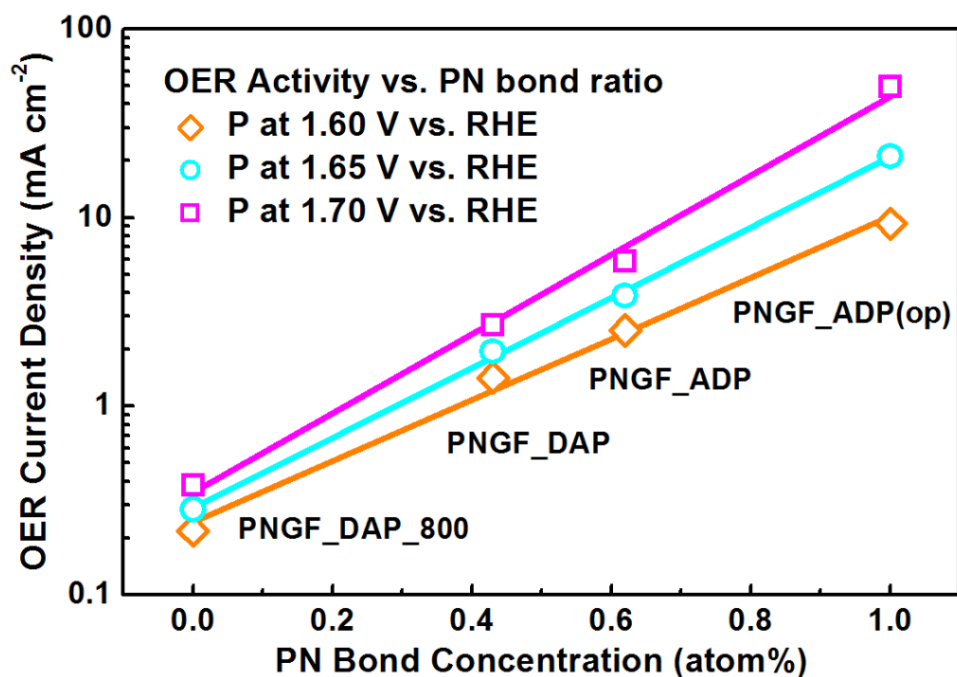


Figure 6-15. Correlation between the OER current densities at the potentials of 1.6 – 1.7 V vs. RHE and the PN bond concentrations.

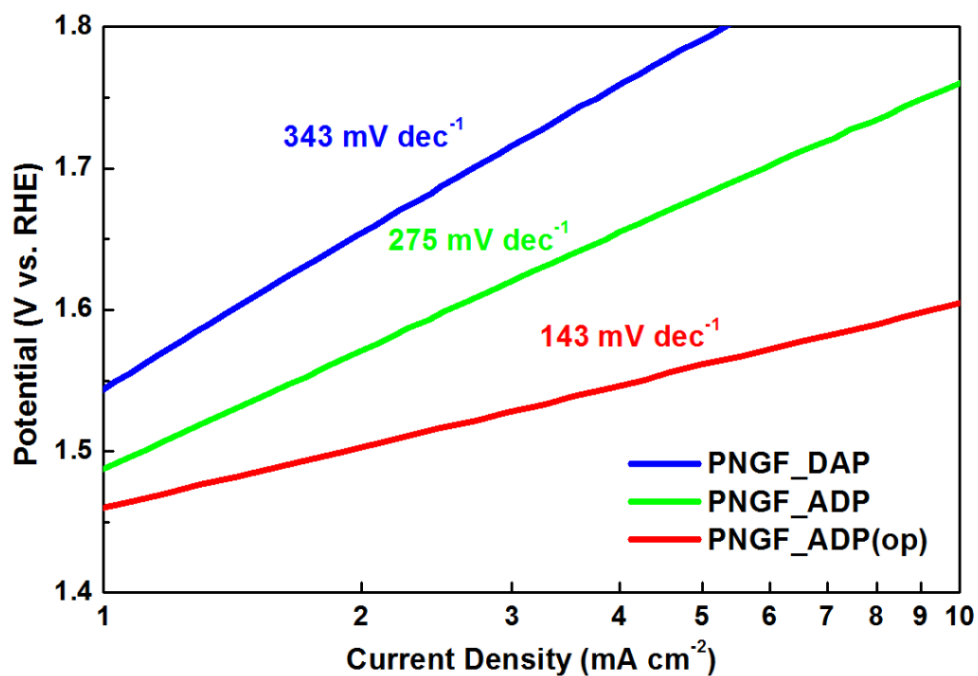


Figure 6-16. OER Tafel plots of PNGF_DAP, PNGF_ADAP and PNGF_ADAP(op), derived from the OER LSV in Figure 6-14.

The excellent catalytic activity of PNGF_ADOP(op) is even comparable to the commercial Pt/C for ORR and Ir/C for OER, respectively. As shown in **Figure 6-17**, the ORR / OER potentials at the current densities of 3 and 10 mA cm⁻² are almost identical for PNGF_ADOP(op) and the noble metal counterparts. Moreover, both the durability (performance loss during potential cycling, **Figure 6-17**) and stability (performance loss during chronoamperometry measurement, **Figures 6-18 and 6-19**) of PNGF_ADOP(op) are considerably superior to the noble metal counterparts.

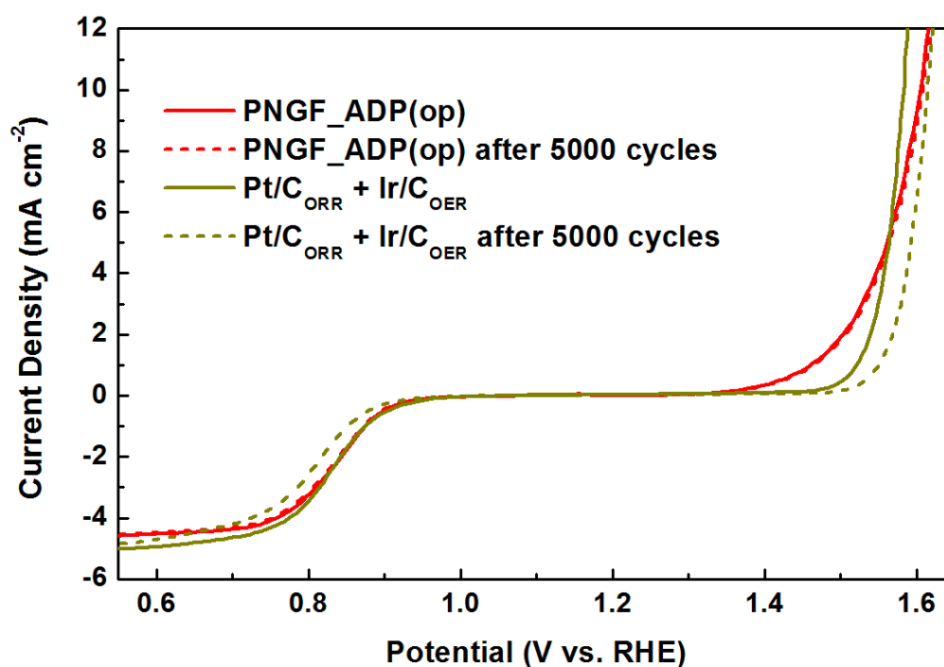


Figure 6-17. Comparison of bifunctional ORR / OER performance for PNGF_ADOP(op) and Pt/C+Ir/C before and after potential cycling between 0.2 and 1.2 V vs. RHE for ORR, or between 1.2 and 2.0 V vs. RHE for OER, using a scan rate of 100 mV s⁻¹ for 5,000 times,

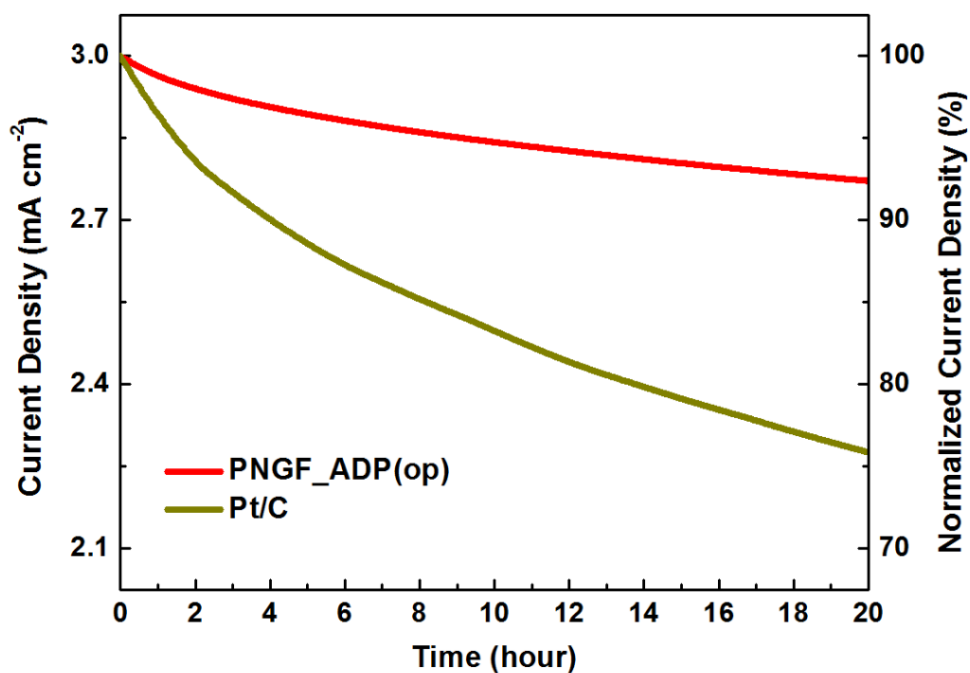


Figure 6-18. Chronoamperometry measurement of PNGF_ADOP and Pt/C in O₂-saturated 0.1M KOH, under 1600RPM, at an initial ORR current of 3 mA cm⁻².

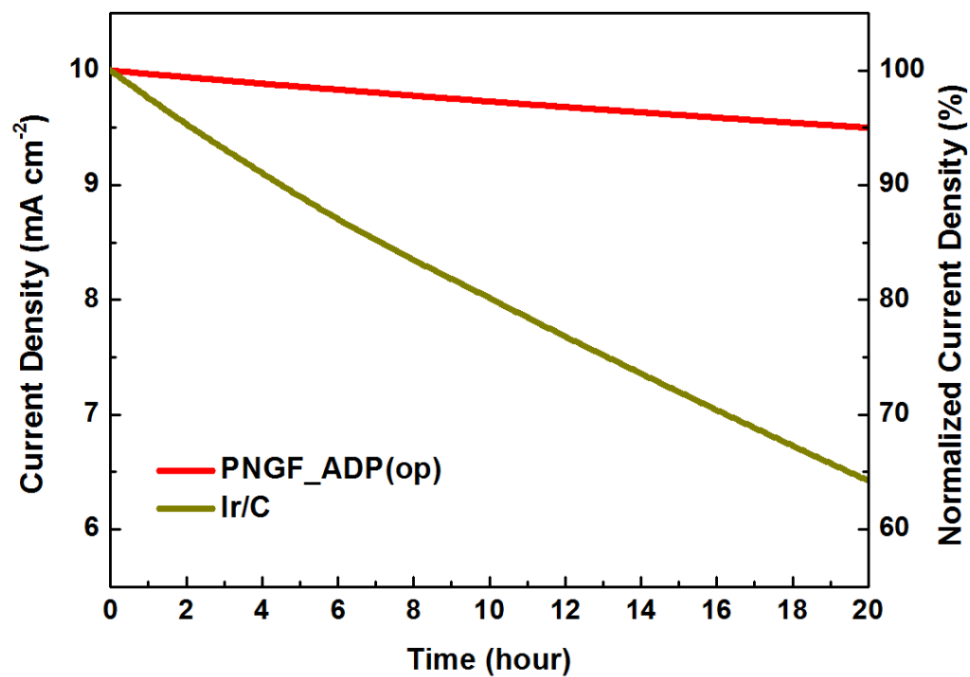


Figure 6-19. Chronoamperometry measurement of PNGF_ADOP and Ir/C in O₂-saturated 0.1M KOH, under 1600RPM, at an initial OER current of 10 mA cm⁻².

For a better comparison with other metal-free bifunctional catalysts, I have increased the catalysts loading from 0.10 to 0.15 mg cm⁻² as used in previous reports.^{8,19} In this case, PNGF_ADOP(op) shows an ORR potential of 0.830 V vs. RHE at 3 mA cm⁻² and OER potential of 1.567 V vs. RHE at 10 mA cm⁻², determined by RDE at a rotating speed of 1600 RPM (**Figure 6-20**).

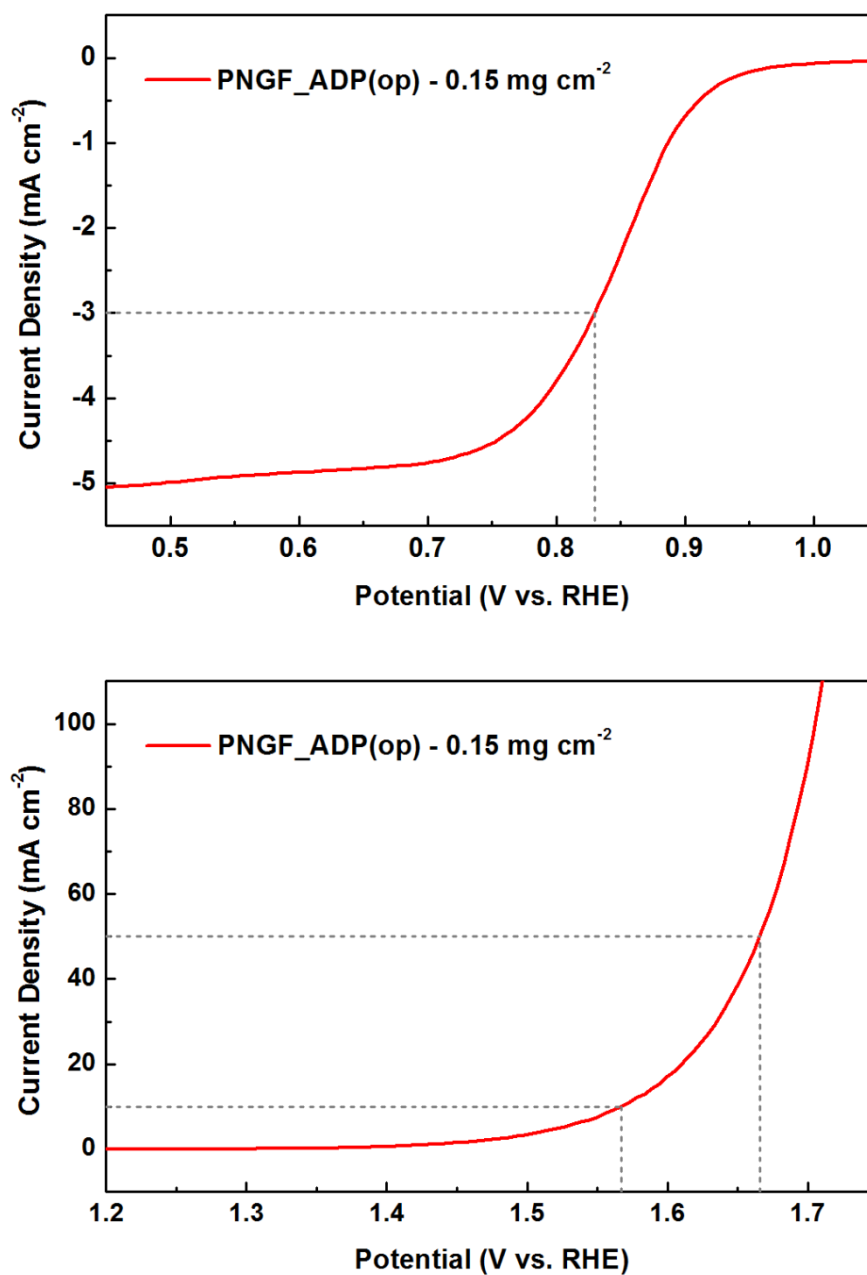


Figure 6-20. ORR (top) / OER (bottom) LSV plots of PNGF_ADOP(op) in 0.1M O₂-saturated KOH under 1600 RPM, using a catalyst loading of 0.15 mg cm⁻².

As shown in **Figure 6-21**, the resulting ORR / OER potential gap of 737 mV for PNGF_ADP(op) is among the top of all the previously reported metal-free bifunctional catalysts, to the best of my knowledge.^{10, 12, 231-233} Notably, PNGF_ADP(op) exhibits rather good OER kinetics especially at a high current. It only needs a reasonably small over-potential of less than 440 mV to reach 50 mA cm^{-2} , which is 130 mV smaller than the over-potential required by the formerly reported best metal-free catalysts to achieve the same current density, **Figure 21**.¹⁹

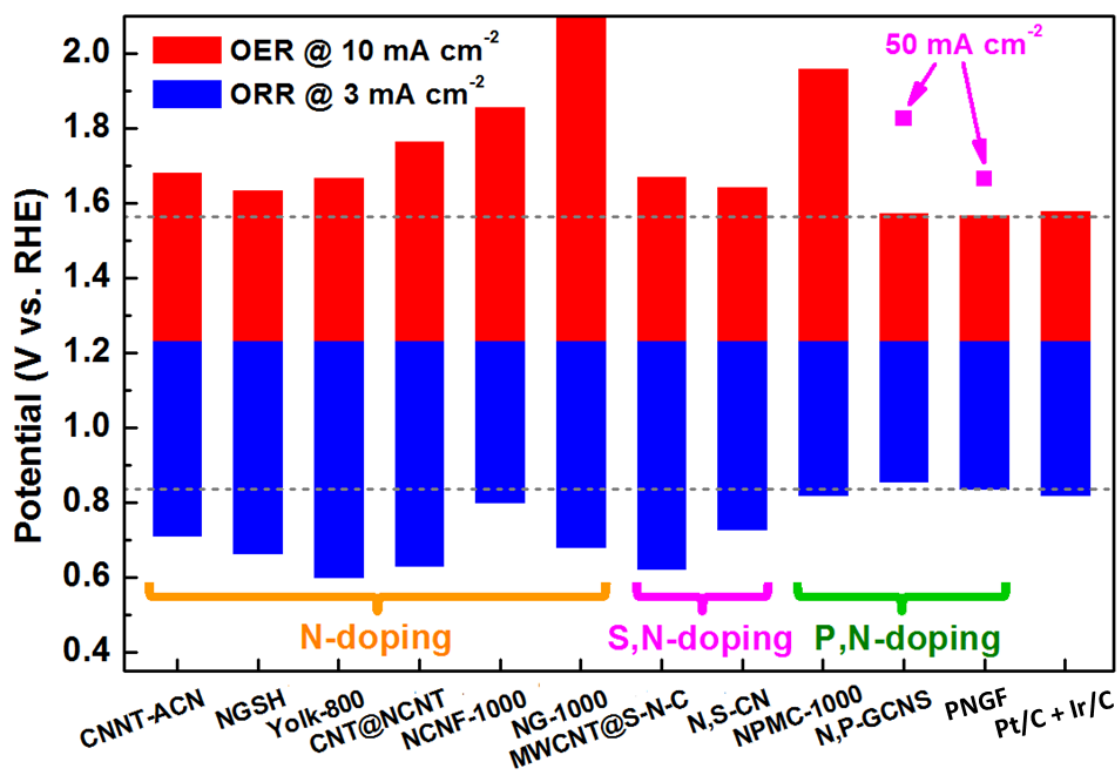


Figure 6-21. Comparison of ORR (blue) and OER potential (red) at 3 mA cm^{-2} , respectively, measured by RDE at 1600 RPM in 0.1 M O_2 -saturated KOH, for the previously reported bifunctional metal-free catalysts. The much smaller OER potential of our PNGF than that of N,P-GCNS at 50 mA cm^{-2} , measured by the same method, indicates a first OER kinetics.

6.3. Summary

To summarize, I have successfully coupled first-principles simulations and experiments to identify and confirm clearly the effective ORR / OER active sites for P, N co-doped metal-free materials, and thereafter rationally synthesised highly efficient bi-functional catalysts. My results show that the OER performance is strongly correlated with the P-N bonds, while the ORR activity with N-doped moieties. Such catalytic sites were effectively introduced into a carefully designed P, N co-doped graphene framework (PNGF). The optimised bifunctional catalyst shows almost identical activity and much superior durability compared with the commercial noble metal counterparts, Pt/C for ORR and Ir/C for OER, respectively. In addition, the highly efficient bifunctional ORR / OER activity of PNGF is also among the best of all the existing metal-free bifunctional catalysts.

Chapter 7. Conclusion and Future Work

In short, three different graphene based electrocatalysts have been rationally designed and synthesized in this thesis, based on the detailed mechanistic understanding of oxygen electrocatalysis in alkaline electrolytes, so as to replace the commercial noble metal counterparts, namely the platinum loaded carbon (Pt/C) for oxygen reduction reaction (ORR) and the iridium loaded carbon (Ir/C) for oxygen evolution reaction (OER), respectively. These three graphene based electrocatalysts are

- 1) The intercalated graphene / graphitic carbon nitride composite (GS/GCN) as a metal-free catalyst for oxygen reduction reaction (**Chapter 4**);
- 2) The maghemite embedded nitrogen doped graphene framework ($\gamma\text{-Fe}_2\text{O}_3\text{@N-GF}$) as a non-precious metal catalyst for oxygen reduction reaction (**Chapter 5**);
- 3) The phosphorus and nitrogen co-doped graphene framework (PNGF) as a metal-free bifunctional catalyst for oxygen reduction and evolution (**Chapter 6**).

The electrochemical performance evaluations of the developed systems have clearly demonstrated that, for a same catalyst loading,

- 1) The GS/GCN composite can exhibit comparable ORR activity but superior methanol tolerance and long-term durability to the commercial 20wt% Pt/C, and its performance is among the best of all the GCN based ORR catalysts (**Chapter 4**);
- 2) The $\gamma\text{-Fe}_2\text{O}_3\text{@N-GF}$ can exhibit both superior ORR activity and durability to the commercial 20wt% Pt/C, and its ORR performance is indeed among the best of all the

iron-based ORR catalysts evaluated in alkaline electrolytes (**Chapter 5**);

3) The PNGF can exhibit exceptional bifunctionality with both ORR and OER catalytic activity and durability superior to the commercial Pt/C and Ir/C, respectively, and is at the top of all the reported metal-free catalysts, in good accordance with the computational prediction from my colleague (**Chapter 6**).

The results in this thesis strongly support the argument that heteroatom doped graphene based materials, either in the form of catalysts themselves or as the substrates for other co-catalysts for ORR and OER, can be highly efficient and durable in alkaline electrolytes at ambient conditions. Hence, development of rechargeable metal-air batteries or regenerative fuel cells based on such catalysts are urgently demanded, in order to transfer the knowledge gained from in thesis to industrial demonstration.

Apart from the promising results shown in this thesis, several other issues need to be taken into account during the further development of graphene based electrocatalysts for ORR / OER:

- 1) The ORR / OER activities of graphene based metal-free catalysts are yet to be comparable with the state-of-the-art noble metal or non-noble metal catalysts (e.g. ORR / OER overpotentials at 3 and 10 mA cm⁻² measured by RDE at 1600 RPM are only 330 and 200 mV, respectively).^{5,159} In particular, the poor OER kinetics of metal-free catalysts is the major issues. To further address this issue, I have managed to design heteroatom doped graphene with extraordinarily good

OER and ORR activity under the guidance of simulation predictions, in one of my latest work (No. 10 in the **List of Publications**, not included in thesis). The bifunctional activity achieved can even surpass the state-of-the-art non-noble metal catalysts;

- 2) The exceptional durability of metal-free catalysts including heteroatom doped graphene based materials at ambient conditions has been commonly regarded as one of the key advantages of such materials.^{20,24} This observation, however, is in contrary to the Pourbaix diagram of carbon, indicating that carbon is not thermodynamically stable under the operational potential range for ORR / OER, either in acid or alkaline electrolytes. The reason for this conflict has to be the kinetic stability of carbon materials against oxidation. On the other hand, the atomic dopants cause far less lattice distortions and/or stronger coherency than supported nanoparticles, which is why metal-free catalysts have been commonly reported to demonstrate superior durability to commercial noble metal (oxide) loaded carbon. Note that quite a few PEMFC tests suggest that carbon based materials (i.e. graphite) are seldom stable under real operational conditions (e.g. 80 °C), indicating further evaluation of metal-free materials' durability at elevated temperatures is highly necessary.
- 3) With regard to the experimental setup for electrochemical measurement, the Ag/AgCl (saturated KCl) reference electrodes used in this work are better to be replaced with the Hg/HgO ones (the concentration of NaOH depends on the specific tests), the platinum sheets counter electrodes are better to be replaced with the 'electrocatalytically-inert' graphite or glassy carbon electrodes, and the

glass electrochemical cells are better to be replaced with the PTFE ones. By using such a setup, the potential contaminations such as the dissolved Pt from counter electrodes and silicate ions from glass cells into alkaline electrolytes can be largely avoided, and the reference potential can be more constant and reliable. The current setup should be fine for short-term measurement (e.g. CV and LSV tests), however the recommend one can be better for the long-term measurement to eliminate the influence of possible contamination (e.g. **Figure 4-22**).

- 4) The difference between the direct $4e^-$ pathway and the indirect 2+2 pathway has not been studied in details in this work. One potential way of telling them from is to conduct the RRDE measurement at a very low catalysts loading (Note that even though RRDE has been adopted in this thesis, the relatively high catalysts loading can immediate reduce the peroxide formed during the reaction on the glass carbon disk electrode, before it is detected by the platinum ring electrode. Nevertheless, the catalysts that have been studied in this thesis are mainly metal-free carbon based materials and non-noble metals such as iron compound, and thus the observed 'four electron transfer' via rotating (ring) disk electrode measurement (e.g. **Figure 5-23**) should be mostly referred to the associative $4e^-$ pathway, or in other word, an indirect 2+2 pathway.
- 5) Since the final product for ORR in alkaline electrolytes is either hydroxide or peroxide, the difference can be most or less inter-changeable with concept of electron transfer number. However, as for OER, the observed current density of metal-free materials (e.g. Figure 6-14) may also be due to the carbon oxidation

(i.e. formation of carbon dioxide / monoxide). Hence, calculation of the faradic efficiency is necessary. The most appropriate method should be to quantify the amount of gas formed during the reaction via (in-situ) Gas Chromatography / Mass Spectrometry (GC/MS). Alternatively, the simpler way is to calculate the theoretical current density value associated with the oxygen evolution, and compare with the experimentally measured values; if the experimental one is much larger, then carbon oxidation side reactions are very likely be involved.

References

1. Lefevre, M., Proietti, E., Jaouen, F. & Dodelet, J.P. Iron-Based Catalysts with Improved Oxygen Reduction Activity in Polymer Electrolyte Fuel Cells. *Science* **324**, 71-74 (2009).
2. Suntivich, J., Gasteiger, H.A., Yabuuchi, N., Nakanishi, H., Goodenough, J.B. & Shao-Horn, Y. Design Principles for Oxygen-Reduction Activity on Perovskite Oxide Catalysts for Fuel Cells and Metal-Air Batteries. *Nature Chemistry* **3**, 546-550 (2011).
3. Liao, L., Zhang, Q., Su, Z., Zhao, Z., Wang, Y., Li, Y., Lu, X., Wei, D., Feng, G., Yu, Q., Cao, X., Zhao, J., Ren, Z., Fang, H., Robles-Hernandez, F., Baldelli S. & Bao, J. Efficient Solar Water-Splitting using a Nanocrystalline CoO Photocatalyst. *Nature Nanotechnology* **9**, 69-73 (2014).
4. Steele, B.C.H. & Heinzel, A. Materials for Fuel-Cell Technologies. *Nature* **414**, 345-352 (2001).
5. Huang, X.Q., Zhao, Z.P., Cao, L., Chen, Y., Zhu, E.B., Lin, Z.Y., Li, M.F., Yan, A.M., Zettl, A., Wang, Y.M., Duan, X.F., Mueller, T. & Huang, Y. High-Performance Transition Metal-doped Pt₃Ni Octahedra for Oxygen Reduction Reaction. *Science* **348**, 1230-1234 (2015).
6. Lee, Y., Suntivich, J., May, K.J., Perry, E.E. & Shao-Horn, Y. Synthesis and Activities of Rutile IrO₂ and RuO₂ Nanoparticles for Oxygen Evolution in Acid and Alkaline Solutions. *The Journal of Physical Chemistry Letters* **3**, 399-404 (2012).

7. Xia, B.Y., Yan, Y., Li, N., Wu, H.B., Lou, X.W. & Wang, X. A Metal–Organic Framework-derived Bifunctional Oxygen Electrocatalyst. *Nature Energy* **1**, 15006 (2016).
8. Zitolo, A., Goellner, V., Armel, V., Sougrati, M.-T., Mineva, T., Stievano, L., Fonda, E. & Jaouen, F. Identification of Catalytic Sites for Oxygen Reduction in Iron- and Nitrogen-doped Graphene Materials. *Nature Materials* **14**, 937-942 (2015).
9. Snyder, J., Fujita, T., Chen, M.W. & Erlebacher, J. Oxygen Reduction in Nanoporous Metal-ionic Liquid Composite Electrocatalysts. *Nature Materials* **9**, 904-907 (2010).
10. Zhang, J., Zhao, Z., Xia, Z. & Dai, L. A Metal-free Bifunctional Electrocatalyst for Oxygen Reduction and Oxygen Evolution Reactions. *Nature Nanotechnology* **10**, 444-452 (2015).
11. Tang, C., Wang, H.F., Chen, X., Li, B.Q., Hou, T.Z., Zhang, B., Zhang, Q., Titirici, M.M. & Wei, F. Topological Defects in Metal-Free Nanocarbon for Oxygen Electrocatalysis. *Advanced Materials* **28**, 6845-6851 (2016).
12. Tian, G.-L., Zhang, Q., Zhang, B., Jin, Y.-G., Huang, J.-Q., Su, D.S. & Wei, F. Toward Full Exposure of “Active Sites”: Nanocarbon Electrocatalyst with Surface Enriched Nitrogen for Superior Oxygen Reduction and Evolution Reactivity. *Advanced Functional Materials* **24**, 5956-5961 (2014).
13. Chai, G.-L., Hou, Z., Shu, D.-J., Ikeda, T. & Terakura, K. Active Sites and Mechanisms for Oxygen Reduction Reaction on Nitrogen-Doped Carbon Alloy Catalysts: Stone-Wales Defect and Curvature Effect. *Journal of the American Chemical Society* **136**, 13629-13640 (2014).

14. Greeley, J., Stephens, I.E.L., Bondarenko, A.S., Johansson, T.P., Hansen, H.A., Jaramillo, T.F., Rossmeisl, J., Chorkendorff, I. & Nørskov, J.K. Alloys of Platinum and Early Transition Metals as Oxygen Reduction Electrocatalysts. *Nature Chemistry* **1**, 552-556 (2009).
15. Nørskov, J.K., Bligaard, T., Rossmeisl, J. & Christensen, C.H. Towards the Computational Design of Solid Catalysts. *Nature Chemistry* **1**, 37-46 (2009).
16. Calle-Vallejo, F., Martinez, J.I. & Rossmeisl, J. Density Functional Studies of Functionalized Graphitic Materials with Late Transition Metals for Oxygen Reduction Reactions. *Physical Chemistry Chemical Physics* **13**, 15639-15643 (2011).
17. Zhou, X., Qiao, J., Yang, L. & Zhang, J. A Review of Graphene-Based Nanostructural Materials for Both Catalyst Supports and Metal-Free Catalysts in PEM Fuel Cell Oxygen Reduction Reactions. *Advanced Energy Materials* **4**, 1301523 (2014).
18. Fan, X., Zhang, G. & Zhang, F. Multiple Roles of Graphene in Heterogeneous Catalysis. *Chemical Society Reviews* **44**, 3023-3035 (2015).
19. Gao, W., Havas, D., Gupta, S., Pan, Q., He, N., Zhang, H., Wang, H.-L. & Wu, G. Is Reduced Graphene Oxide Favorable for Nonprecious Metal Oxygen-Reduction Catalysts? *Carbon* **102**, 346-356 (2016).
20. Higgins, D., Zamani, P., Yu, A. & Chen, Z. The Application of Graphene and Its Composites in Oxygen Reduction Electrocatalysis: A Perspective and Review of Recent Progress. *Energy & Environmental Science* **9**, 357-390 (2016).
21. Jiao, Y., Zheng, Y., Jaroniec, M. & Qiao, S.Z. Origin of the Electrocatalytic

- Oxygen Reduction Activity of Graphene-based Catalysts: A Roadmap to Achieve the Best Performance. *Journal of the American Chemical Society* **136**, 4394-4403 (2014).
22. Zhao, Z., Li, M., Zhang, L., Dai, L. & Xia, Z. Design Principles for Heteroatom-Doped Carbon Nanomaterials as Highly Efficient Catalysts for Fuel Cells and Metal-Air Batteries. *Advanced Materials* **27**, 6834-6840 (2015).
23. Wang, D.-W. & Su, D. Heterogeneous Nanocarbon Materials for Oxygen Reduction Reaction. *Energy & Environmental Science* **7**, 576-591 (2014).
24. Huang, C., Li, C. & Shi, G. Graphene based Catalysts. *Energy & Environmental Science* **5**, 8848-8868 (2012).
25. Deng, D., Novoselov, K.S., Fu, Q., Zheng, N., Tian, Z. & Bao, X. Catalysis with Two-dimensional Materials and Their Heterostructures. *Nature Nanotechnology* **11**, 218-230 (2016).
26. Blizanac, B.B., Ross, P.N. & Markovic, N.M. Oxygen Electroreduction on Ag(1 1 1): The pH Effect. *Electrochimica Acta* **52**, 2264-2271 (2007).
27. Wan, K., Yu, Z., Li, X.-H., Liu, M.-Y., Yang, G., Piao, J. & Liang, Z. pH Effect on Electrochemistry of Nitrogen-Doped Carbon Catalyst for Oxygen Reduction Reaction. *ACS Catalysis* **5**, 4325-4332 (2015).
28. Ramaswamy, N. & Mukerjee, S. Influence of Inner- and Outer-Sphere Electron Transfer Mechanisms during Electrocatalysis of Oxygen Reduction in Alkaline Media. *The Journal of Physical Chemistry C* **115**, 18015-18026 (2011).
29. Ramaswamy, N. & Mukerjee, S. Fundamental Mechanistic Understanding of Electrocatalysis of Oxygen Reduction on Pt and Non-Pt Surfaces: Acid versus

- Alkaline Media. *Advances in Physical Chemistry* **2012**, 17 (2012).
30. Winter, M. & Brodd, R.J. What Are Batteries, Fuel Cells, and Supercapacitors? *Chemical Reviews* **104**, 4245-4270 (2004).
31. Cheng, F. & Chen, J. Metal-Air Batteries: From Oxygen Reduction Electrochemistry to Cathode Catalysts. *Chemical Society Reviews* **41**, 2172-2192 (2012).
32. Wang, Z.-L., Xu, D., Xu, J.-J. & Zhang, X.-B. Oxygen Electrocatalysts in Metal-Air Batteries: From Aqueous to Nonaqueous Electrolytes. *Chemical Society Reviews* **43**, 7746-7786 (2014).
33. Lee, J.-S., Tai Kim, S., Cao, R., Choi, N.-S., Liu, M., Lee, K.T. & Cho, J.. Metal-Air Batteries with High Energy Density: Li-Air versus Zn-Air. *Advanced Energy Materials* **1**, 34-50 (2011).
34. Vielstich, W. Ideal and Effective Efficiencies of Cell Reactions and Comparison to Carnot Cycles. *Handbook of Fuel Cells: Fundamentals, Technology, and Applications* (John Wiley and Sons, Inc., New York, 2010).
35. Liang, Y., Li, Y., Wang, H. & Dai, H. Strongly Coupled Inorganic/Nanocarbon Hybrid Materials for Advanced Electrocatalysis. *Journal of the American Chemical Society* **135**, 2013-2036 (2013).
36. Li, Y. & Dai, H. Recent Advances in Zinc-Air Batteries. *Chemical Society Reviews* **43**, 5257-5275 (2014).
37. Lopes, T., Kucernak, A., Malko, D. & Ticianelli, E.A. Mechanistic Insights into the Oxygen Reduction Reaction on Metal-N-C Electrocatalysts under Fuel Cell Conditions. *ChemElectroChem* (2016). DOI: 10.1002/celec.201600354.

38. Cifrain, M. & Kordesch, K. Hydrogen/Oxygen (Air) Fuel Cells with Alkaline Electrolytes. *Handbook of Fuel Cells: Fundamentals, Technology, and Applications* (John Wiley and Sons, Inc., New York, 2010).
39. Kordesch, K. & Cifrain, M. A Comparison between the Alkaline Fuel Cell (AFC) and the Polymer Electrolyte Membrane (PEM) Fuel Cell. *Handbook of Fuel Cells: Fundamentals, Technology, and Applications* (John Wiley and Sons, Inc., New York, 2010).
40. Varcoe, J.R. & Slade, R.C.T. Prospects for Alkaline Anion-Exchange Membranes in Low Temperature Fuel Cells. *Fuel Cells* **5**, 187-200 (2005).
41. Merle, G., Wessling, M. & Nijmeijer, K. Anion Exchange Membranes for Alkaline Fuel Cells: A Review. *Journal of Membrane Science* **377**, 1-35 (2011).
42. Debe, M.K. Electrocatalyst Approaches and Challenges for Automotive Fuel Cells. *Nature* **486**, 43-51 (2012).
43. Scofield, M.E., Liu, H. & Wong, S.S. A Concise Guide to Sustainable PEMFCs: Recent Advances in Improving both Oxygen Reduction Catalysts and Proton Exchange Membranes. *Chemical Society Reviews* **44**, 5836-5860 (2015).
44. Shao, Y., Cheng, Y., Duan, W., Wang, W., Lin, Y., Wang, Y. & Liu, J. Nanostructured Electrocatalysts for PEM Fuel Cells and Redox Flow Batteries: a Selected Review. *ACS Catalysis* **5**, 7288-7298 (2015).
45. Neergat, M., Friedrich, K.A. & Stimming, U. New Materials for DMFC MEAs. *Handbook of Fuel Cells: Fundamentals, Technology, and Applications* (John Wiley and Sons, Inc., New York, 2010).
46. Lamm, A. & Müller, J. System Design for Transport Applications. *Handbook of*

- Fuel Cells: Fundamentals, Technology, and Applications* (John Wiley and Sons, Inc., New York, 2010).
47. Narayanan, S.R., Valdez, T.I. & Rohatgi, N. DMFC System Design for Portable Applications. *Handbook of Fuel Cells: Fundamentals, Technology, and Applications* (John Wiley and Sons, Inc., New York, 2010).
 48. Adler, S.B. Factors Governing Oxygen Reduction in Solid Oxide Fuel Cell Cathodes. *Chemical Reviews* **104**, 4791-4843 (2004).
 49. Li, Y.H., Gemmen, R. & Liu, X.B. Oxygen Reduction and Transportation Mechanisms in Solid Oxide Fuel Cell Cathodes. *Journal of Power Sources* **195**, 3345-3358 (2010).
 50. Kawada, T. & Mizusaki, J. Current Electrolytes and Catalysts. *Handbook of Fuel Cells: Fundamentals, Technology, and Applications* (John Wiley and Sons, Inc., New York, 2010).
 51. Chen, Y., Zhou, W., Ding, D., Liu, M., Ciucci, F., Tade, M. & Shao, Z. Advances in Cathode Materials for Solid Oxide Fuel Cells: Complex Oxides without Alkaline Earth Metal Elements. *Advanced Energy Materials* **5**, 1500537 (2015).
 52. Zhou, Y., Wu, H., Luo, T., Wang, J., Shi, Y., Xia, C., Wang, S. & Zhan, Z. A Nanostructured Architecture for Reduced-Temperature Solid Oxide Fuel Cells. *Advanced Energy Materials* **5**, 1500375 (2015).
 53. Zhu, Y., Zhou, W., Ran, R., Chen, Y., Shao, Z. & Liu, M.. Promotion of Oxygen Reduction by Exsolved Silver Nanoparticles on a Perovskite Scaffold for Low-Temperature Solid Oxide Fuel Cells. *Nano Letters* **16**, 512-518 (2016).
 54. Yamamoto, O. Low Temperature Electrolytes and Catalysts. *Handbook of Fuel*

- Cells: Fundamentals, Technology, and Applications* (John Wiley and Sons, Inc., New York, 2010).
55. Ishihara, T. Novel Electrolytes Operating at 400-600 °C. *Handbook of Fuel Cells: Fundamentals, Technology, and Applications* (John Wiley and Sons, Inc., New York, 2010).
56. Rahman, M.A., Wang, X. & Wen, C. High Energy Density Metal-Air Batteries: A Review. *Journal of the Electrochemical Society* **160**, A1759-A1771 (2013).
57. Neburchilov, V., Wang, H., Martin, J.J. & Qu, W. A Review on Air Cathodes for Zinc-Air Fuel Cells. *Journal of Power Sources* **195**, 1271-1291 (2010).
58. Harting, K., Kunz, U. & Turek, T. Zinc-Air Batteries: Prospects and Challenges for Future Improvement. *International Journal of Research in Physical Chemistry & Chemical Physics* **226**, 151-166 (2012).
59. Koscher, G.A. & Kordesch, K. Alkaline Methanol/Air Power Devices. *Handbook of Fuel Cells: Fundamentals, Technology, and Applications* (John Wiley and Sons, Inc., New York, 2010).
60. IEC. Electrical Energy Storage. *International Electrotechnical Commission White Papers*, 1-78 (International Electrotechnical Commission, Switzerland, 2015).
61. Toussaint, G., Stevens, P., Akrou, L., Rouget, R. & Fourgeot, F. Development of a Rechargeable Zinc-Air Battery. *Metal/Air and Metal/Water Batteries* **28**, 25-34 (2010).
62. Ma, H., Wang, B., Fan, Y. & Hong, W. Development and Characterization of an Electrically Rechargeable Zinc-Air Battery Stack. *Energies* **7**, 6549-6557 (2014).
63. Pei, P., Wang, K. & Ma, Z. Technologies for Extending Zinc-Air Battery's Cyclelife:

- A Review. *Applied Energy* **128**, 315-324 (2014).
64. Gallaway, J.W., Gaikwad, A.M., Hertzberg, B., Erdonmez, C.K., Chen-Wiegart, Y.K. Sviridov, L.A., Evans-Lutterodt, K., Wang, J., Banerjee, S. & Steingart, D.A. An In Situ Synchrotron Study of Zinc Anode Planarization by a Bismuth Additive. *Journal of the Electrochemical Society* **161**, A275-A284 (2014).
65. Xu, M., Ivey, D.G., Xie, Z. & Qu, W. Rechargeable Zn-Air Batteries: Progress in Electrolyte Development and Cell Configuration Advancement. *Journal of Power Sources* **283**, 358-371 (2015).
66. Leung, P. Li, X., Ponce de Leon, C., Berlouis, L., Low, C.T.J. & Walsh, F.C. Progress in Redox Flow Batteries, Remaining Challenges and Their Applications in Energy Storage. *RSC Advances* **2**, 10125-10156 (2012).
67. Li, Y., Gong, M., Liang, Y., Feng, J., Kim, J.E., Wang, H., Hong, G. Zhang, B. & Dai, H.. Advanced Zinc-Air Batteries Based on High-performance Hybrid Electrocatalysts. *Nature Communications* **4**, 1805 (2013).
68. Narayanan, S.R., Prakash, G.K.S., Manohar, A., Yang, B., Malkhandi, S. & Kindler, A. Materials Challenges and Technical Approaches for Realizing Inexpensive and Robust Iron-Air Batteries for Large-scale Energy Storage. *Solid State Ionics* **216**, 105-109 (2012).
69. Egan, D.R., Ponce de León, C., Wood, R.J.K., Jones, R.L. Stokes, K.R. & Walsh, F.C. Developments in Electrode Materials and Electrolytes for Aluminium-Air Batteries. *Journal of Power Sources* **236**, 293-310 (2013).
70. Zhang, T., Tao, Z. & Chen, J. Magnesium-Air Batteries: From Principle to Application. *Materials Horizons* **1**, 196-206 (2014).

71. Öjefors, L. & Carlsson, L. An Iron-Air Vehicle Battery. *Journal of Power Sources* **2**, 287-296 (1978).
72. Zaromb, S. The Use and Behavior of Aluminum Anodes in Alkaline Primary Batteries. *Journal of the Electrochemical Society* **109**, 1125-1130 (1962).
73. Carson, W., Kent, C. & Collins, D. The Magnesium/Air Cell. *Power Sources: Research Development in Non-Mechanical Electrical Power* (Pergamon Press, Oxford, 1966).
74. Girishkumar, G., McCloskey, B., Luntz, A.C., Swanson, S. & Wilcke, W. Lithium-Air Battery: Promise and Challenges. *The Journal of Physical Chemistry Letters* **1**, 2193-2203 (2010).
75. Hartmann, P., Bender, C.L., Vračar, M., Dürr, A.N., Garsuch, A., Janek J. & Adelhelm P. A rechargeable Room-Temperature Sodium Superoxide (NaO₂) Battery. *Nature Materials* **12**, 228-232 (2013).
76. Ren, X. & Wu, Y. A Low-Overpotential Potassium-Oxygen Battery Based on Potassium Superoxide. *Journal of the American Chemical Society* **135**, 2923-2926 (2013).
77. Bruce, P.G., Freunberger, S.A., Hardwick, L.J. & Tarascon, J.-M. Li-O₂ and Li-S Batteries with High Energy Storage. *Nature Materials* **11**, 19-29 (2012).
78. Aurbach, D., McCloskey, B.D., Nazar, L.F. & Bruce, P.G. Advances in Understanding Mechanisms Underpinning Lithium-air Batteries. *Nature Energy* **1**, 16128 (2016).
79. Peng, Z., Freunberger, S.A., Chen, Y. & Bruce, P.G. A Reversible and Higher-Rate Li-O₂ Battery. *Science* **337**, 563-566 (2012).

80. Chen, Y., Freunberger, S.A., Peng, Z., Fontaine, O. & Bruce, P.G. Charging a Li-O₂ Battery Using a Redox Mediator. *Nature Chemistry* **5**, 489-494 (2013).
81. Ottakam Thotiyl, M.M., Freunberger, S.A., Peng, Z., Chen, Y., Liu, Z. & Bruce, P.G., A Stable Cathode for the Aprotic Li-O₂ Battery. *Nature Materials* **12**, 1050-1056 (2013).
82. Johnson, L., Li, C., Liu, Z., Chen, Y., Freunberger, S.A., Ashok, P.C., Praveen, B.B., Dholakia, K., Tarascon, J.-M. & Bruce, P.G. The Role of LiO₂ Solubility in O₂ Reduction in Aprotic Solvents and its Consequences for Li-O₂ Batteries. *Nature Chemistry* **6**, 1091-1099 (2014).
83. Gao, X., Chen, Y., Johnson, L. & Bruce, P.G. Promoting Solution Phase Discharge in Li-O₂ Batteries Containing Weakly Solvating Electrolyte Solutions. *Nature Materials* **15**, 882-888 (2016).
84. Wang, Y., Kong, A., Chen, X., Lin, Q. & Feng, P. Efficient Oxygen Electroreduction: Hierarchical Porous Fe-N-doped Hollow Carbon Nanoshells. *ACS Catalysis* **5**, 3887-3893 (2015).
85. Liu, R., von Malotki, C., Arnold, L., Koshino, N., Higashimura, H., Baumgarten, M. & Müllen, K. Triangular Trinuclear Metal-N₄ Complexes with High Electrocatalytic Activity for Oxygen Reduction. *Journal of the American Chemical Society* **133**, 10372-10375 (2011).
86. Lin, L., Zhu, Q. & Xu, A.-W. Noble-Metal-Free Fe-N/C Catalyst for Highly Efficient Oxygen Reduction Reaction under Both Alkaline and Acidic Conditions. *Journal of the American Chemical Society* **136**, 11027-11033 (2014).
87. Li, M., Xiong, Y., Liu, X., Han, C., Zhang, Y., Bo, X. & Guo, L. Iron and Nitrogen

- co-doped Carbon Nanotube@Hollow Carbon Fibers Derived from Plant Biomass as Efficient Catalysts for the Oxygen Reduction Reaction. *Journal of Materials Chemistry A* **3**, 9658-9667 (2015).
88. Gattrell, M. & MacDougall, B. Reaction mechanisms of the O₂ reduction/evolution reaction. *Handbook of Fuel Cells: Fundamentals, Technology, and Applications* (John Wiley and Sons, Inc., New York, 2010).
89. Ge, X., Sumboja, A., Wu, D., An, T., Li, B., Goh, F.W.T., Hor, T.S.A., Zong, Y. & Liu, Z. Oxygen Reduction in Alkaline Media: From Mechanisms to Recent Advances of Catalysts. *ACS Catalysis* **5**, 4643-4667 (2015).
90. Nørskov, J.K. Rossmeisl, J., Logadottir A., Lindqvist, L., Kitchin, J.R., Bligaard, T. & Jónsson, H. Origin of the Overpotential for Oxygen Reduction at a Fuel-Cell Cathode. *The Journal of Physical Chemistry B* **108**, 17886-17892 (2004).
91. Busch, M., Halck, N.B., Kramm, U.I., Siahrostami, S., Krttil, P. & Rossmeisl, J. Beyond the Top of the Volcano? A Unified Approach to Electrocatalytic Oxygen Reduction and Oxygen Evolution. *Nano Energy* (2016).
92. Koper, M.T.M. Theory of Multiple Proton-electron Transfer Reactions and its Implications for Electrocatalysis. *Chemical Science* **4**, 2710-2723 (2013).
93. Rossmeisl, J., Logadottir, A. & Nørskov, J.K. Electrolysis of Water on (Oxidized) Metal Surfaces. *Chemical Physics* **319**, 178-184 (2005).
94. Koper, M.T.M. Thermodynamic Theory of Multi-electron Transfer Reactions: Implications for Electrocatalysis. *Journal of Electroanalytical Chemistry* **660**, 254-260 (2011).
95. Medford, A.J., Vojvodic, A., Hummelshøj, J.S., Voss, J., Abild-Pedersen, F.,

- Studdt, F., Bligaard, T., Nilsson, A. & Nørskov, J.K. From the Sabatier Principle to a Predictive Theory of Transition-metal Heterogeneous Catalysis. *Journal of Catalysis* **328**, 36-42 (2015).
96. Man, I.C., Su, H.-Y., Calle-Vallejo, F., Hansen, H.A., Martínez, J.I., Inoglu, N.G., Kitchin, J., Jaramillo, T.F., Nørskov, J.K. & Rossmeisl, J. Universality in Oxygen Evolution Electrocatalysis on Oxide Surfaces. *ChemCatChem* **3**, 1159-1165 (2011).
97. Jiao, Y., Zheng, Y., Jaroniec, M. & Qiao, S.Z. Design of Electrocatalysts for Oxygen- and Hydrogen-involving Energy Conversion Reactions. *Chemical Society Reviews* **44**, 2060-2086 (2015).
98. Borup, R., Meyers, J., Pivovar, B., Kim, Y.S., Mukundan, R., Garland, N., Myers, D., Wilson, M., Garzon, F., Wood, D., Zelenay, P., More, K., Stroh, K., Zawodzinski, T., Boncella, J., McGrath, J.E., Inaba, M., Miyatake, K., Hori, M., Ota, K., Ogumi, Z., Miyata, S., Nishikata, A., Siroma, Z., Uchimoto, Y., Yasuda, K., Kimijima, K. & Iwashita, N. Scientific Aspects of Polymer Electrolyte Fuel Cell Durability and Degradation. *Chemical Reviews* **107**, 3904-3951 (2007).
99. Stephens, I.E.L., Bondarenko, A.S., Gronbjerg, U., Rossmeisl, J. & Chorkendorff, I. Understanding the Electrocatalysis of Oxygen Reduction Platinum and its Alloys. *Energy & Environmental Science* **5**, 6744-6762 (2012).
100. Guo, S., Zhang, S. & Sun, S. Tuning Nanoparticle Catalysis for the Oxygen Reduction Reaction. *Angewandte Chemie International Edition* **52**, 8526-8544 (2013).
101. Rabis, A., Rodriguez, P. & Schmidt, T.J. Electrocatalysis for Polymer Electrolyte

- Fuel Cells: Recent Achievements and Future Challenges. *ACS Catalysis* **2**, 864-890 (2012).
102. Gasteiger, H.A., Kocha, S.S., Sompalli, B. & Wagner, F.T. Activity Benchmarks and Requirements for Pt, Pt-alloy, and non-Pt Oxygen Reduction Catalysts for PEMFCs. *Applied Catalysis B: Environmental* **56**, 9-35 (2005).
103. Morozan, A., Josselme, B. & Palacin, S. Low-platinum and Platinum-free Catalysts for the Oxygen Reduction Reaction at Fuel Cell Cathodes. *Energy & Environmental Science* **4**, 1238-1254 (2011).
104. Wu, J. & Yang, H. Platinum-Based Oxygen Reduction Electrocatalysts. *Accounts of Chemical Research* **46**, 1848-1857 (2013).
105. Greeley, J., Stephens, I.E.L., Bondarenko, A.S., Johansson, T.P., Hansen, H.A., Jaramillo, T.F., Rossmeisl, J., Chorkendorff, I. & Norskov, J.K. Alloys of Platinum and Early Transition Metals as Oxygen Reduction Electrocatalysts. *Nature Chemistry* **1**, 552-556 (2009).
106. Zhang, J., Yang, H., Fang, J. & Zou, S. Synthesis and Oxygen Reduction Activity of Shape-Controlled Pt₃Ni Nanopolyhedra. *Nano Letters* **10**, 638-644 (2010).
107. Paffett, M.T., Daube, K.A., Gottesfeld, S. & Campbell, C.T. Electrochemical and Surface Science Investigations of PtCr Alloy Electrodes. *Journal of Electroanalytical Chemistry and Interfacial Electrochemistry* **220**, 269-285 (1987).
108. Wang, C., Chi, M., Li, D., van der Vliet, D., Wang, G., Lin, Q., Mitchell, J.F., More, K.L., Markovic, N.M. & Stamenkovic, V.R. Synthesis of Homogeneous Pt-Bimetallic Nanoparticles as Highly Efficient Electrocatalysts. *ACS Catalysis* **1**,

- 1355-1359 (2011).
109. Yano, H., Kataoka, M., Yamashita, H., Uchida, H. & Watanabe, M. Oxygen Reduction Activity of Carbon-Supported Pt-M (M = V, Ni, Cr, Co, and Fe) Alloys Prepared by Nanocapsule Method. *Langmuir* **23**, 6438-6445 (2007).
110. Feng, Y.-Y., Zhang, G.-R., Ma, J.-H., Liu, G. & Xu, B.-Q. Carbon-supported Pt/Ag nanostructures as cathode catalysts for oxygen reduction reaction. *Physical Chemistry Chemical Physics* **13**, 3863-3872 (2011).
111. Kang, Y. & Murray, C.B. Synthesis and Electrocatalytic Properties of Cubic Mn-Pt Nanocrystals (Nanocubes). *Journal of the American Chemical Society* **132**, 7568-7569 (2010).
112. Zhang, S., Zhang, X., Jiang, G., Zhu, H., Guo, S., Su, D., Lu, G. & Sun S. Tuning Nanoparticle Structure and Surface Strain for Catalysis Optimization. *Journal of the American Chemical Society* **136**, 7734-7739 (2014).
113. Wang, C. , Li, D., Chi, M., Pearson, J., Rankin, R.B., Greeley, J., Duan, Z., Wang, G., van der Vliet, D., Mor, K.L., Markovic, N.M. & Stamenkovic, V.R. Rational Development of Ternary Alloy Electrocatalysts. *The Journal of Physical Chemistry Letters* **3**, 1668-1673 (2012).
114. Strasser, P. Catalysts by Platonic design. *Science* **349**, 379-380 (2015).
115. Stamenkovic, V.R., Fowler, B., Mun, B.S., Wang, G.F., Ross, P.N., Lucas, C.A. & Markovic, N.M. Improved Oxygen Reduction Activity on Pt₃Ni(111) via Increased Surface Site Availability. *Science* **315**, 493-497 (2007).
116. Gasteiger, H.A. & Marković, N.M. Just a Dream or Future Reality? *Science* **324**, 48-49 (2009).

117. Gan, L., Cui, C., Heggen, M., Dionigi, F., Rudi, S. Strasser, P. Element-specific Anisotropic Growth of Shaped Platinum Alloy Nanocrystals. *Science* **346**, 1502-1506 (2014).
118. Wu, J., Zhang, J., Peng, Z., Yang, S., Wagner F.T. & Yang H. Truncated Octahedral Pt₃Ni Oxygen Reduction Reaction Electrocatalysts. *Journal of the American Chemical Society* **132**, 4984-4985 (2010).
119. Wu, J., Gross, A. & Yang, H. Shape and Composition-Controlled Platinum Alloy Nanocrystals Using Carbon Monoxide as Reducing Agent. *Nano Letters* **11**, 798-802 (2011).
120. Cui, C., Gan, L., Li, H.H., Yu, S.H., Heggen, M. & Strasser, P. Octahedral PtNi Nanoparticle Catalysts: Exceptional Oxygen Reduction Activity by Tuning the Alloy Particle Surface Composition. *Nano Letters* **12**, 5885-5889 (2012).
121. Cui, C., Gan, L., Heggen, M., Rudi, S. & Strasser, P. Compositional Segregation in Shaped Pt Alloy Nanoparticles and Their Structural Behaviour during Electrocatalysis. *Nature Materials* **12**, 765-771 (2013).
122. Choi, S.-I., Xie, S., Shao, M., Odell, J.H., Lu, N., Peng, H.S., Protsailo, L., Guerrero, S., Park, J. Xia, X., Wang, J. Kim, M.J. & Xia, Y. Synthesis and Characterization of 9 nm Pt-Ni Octahedra with a Record High Activity of 3.3 A/mg_{Pt} for the Oxygen Reduction Reaction. *Nano Letters* **13**, 3420-3425 (2013).
123. Chen, C., Kang, Y., Huo, Z., Zhu, Z., Huang, W., Xin, H.L., Snyder, J.D., Li, D., Herron, J.A., Mavrikakis, M., Chi, M., More, K.L., Li, Y., Markovic, N.M., Somorjai, G.A., Yang, P. & Stamenkovic, V.R. Highly Crystalline Multimetallic Nanoframes with Three-Dimensional Electrocatalytic Surfaces. *Science* **343**, 1339-1343

- (2014).
124. Huang, X., Zhao, Z., Cao, L., Chen, Y., Zhu, E., Lin, Z., Li, M., Yan, A., Zettl, A., Wang, Y.M., Duan, X., Mueller, T. & Huang, Y. High-performance Transition Metal-doped Pt₃Ni Octahedra for Oxygen Reduction Reaction. *Science* **348**, 1230-1234 (2015).
 125. Tang, C. & Zhang, Q. Can Metal-Nitrogen-Carbon Catalysts Satisfy Oxygen Electrochemistry? *Journal of Materials Chemistry A* **4**, 4998-5001 (2016).
 126. Garsuch, A., Bonakdarpour, A., Liu, G., Yang, R. & Dahn, J.R. Time to Move beyond Transition Metal-N-C Catalysts for Oxygen Reduction. *Handbook of Fuel Cells: Fundamentals, Technology, and Applications* (John Wiley and Sons, Inc., New York, 2010).
 127. Jasinski, R. A New Fuel Cell Cathode Catalyst. *Nature* **201**, 1212-1213 (1964).
 128. van Veen, J.A.R. & Visser, C. Oxygen Reduction on Monomeric Transition Metal Phthalocyanines in Acid Electrolyte. *Electrochimica Acta* **24**, 921-928 (1979).
 129. Wiesener, K., Ohms, D., Neumann, V. & Franke, R. N₄ Macrocycles as Electrocatalysts for the Cathodic Reduction of Oxygen. *Materials Chemistry and Physics* **22**, 457-475 (1989).
 130. Shi, C. & Anson, F.C. Catalytic Pathways for the Electroreduction of Oxygen by Iron Tetrakis(4-N-methylpyridyl)porphyrin or Iron Tetraphenylporphyrin Adsorbed on Edge Plane Pyrolytic Graphite Electrodes. *Inorganic Chemistry* **29**, 4298-4305 (1990).
 131. Dodelet, J.-P. Oxygen Reduction in PEM Fuel Cell Conditions: Heat-Treated Non-Precious Metal-N₄ Macrocycles and Beyond. *N₄-macrocyclic Metal*

Complexes (2007).

132. Gupta, S., Tryk, D., Bae, I., Aldred, W. & Yeager, E. Heat-treated Polyacrylonitrile-based Catalysts for Oxygen Electroreduction. *Journal of Applied Electrochemistry* **19**, 19-27 (1989).
133. Lalande, G., Côté, R., Guay, D., Dodelet, J.P., Weng, L.T. & Bertrand, P. Is Nitrogen Important in the Formulation of Fe-based Catalysts for Oxygen Reduction in Solid Polymer Fuel Cells? *Electrochimica Acta* **42**, 1379-1388 (1997).
134. Lefèvre, M. & Dodelet, J.-P. Fe-based Catalysts for the Reduction of Oxygen in Polymer Electrolyte Membrane Fuel Cell Conditions: Determination of the Amount of Peroxide Released during Electroreduction and Its Influence on the Stability of the Catalysts. *Electrochimica Acta* **48**, 2749-2760 (2003).
135. Marcotte, S., Villers, D., Guillet, N., Roué, L. & Dodelet, J.P. Electroreduction of Oxygen on Co-based Catalysts: Determination of the Parameters Affecting the Two-electron Transfer Reaction in an Acid Medium. *Electrochimica Acta* **50**, 179-188 (2004).
136. Subramanian, N.P., Subramanian, N.P., Kumaraguru, S.P., Colon-Mercado, H., Kim, H., Popov, B.N., Black, T. & Chen, D.A. Studies on Co-based Catalysts Supported on Modified Carbon Substrates for PEMFC Cathodes. *Journal of Power Sources* **157**, 56-63 (2006).
137. Zheng, Y., Jiao, Y., Jaroniec, M., Jin, Y.G. & Qiao, S.Z. Nanostructured Metal-Free Electrochemical Catalysts for Highly Efficient Oxygen Reduction. *Small* **8**, 3550-3566 (2012).

138. Gong, K.P., Du, F., Xia, Z.H., Durstock, M. & Dai, L.M. Nitrogen-Doped Carbon Nanotube Arrays with High Electrocatalytic Activity for Oxygen Reduction. *Science* **323**, 760-764 (2009).
139. Liang, H.-W., Zhuang, X., Brüller, S., Feng, X. & Müllen, K. Hierarchically Porous Carbons with Optimized Nitrogen Doping as Highly Active Electrocatalysts for Oxygen Reduction. *Nature Communications* **5** 4973 (2014).
140. Paraknowitsch, J.P. & Thomas, A. Doping Carbons beyond Nitrogen: An Overview of Advanced Heteroatom Doped Carbons with Boron, Sulphur and Phosphorus for Energy Applications. *Energy & Environmental Science* **6**, 2839-2855 (2013).
141. Kattel, S., Atanassov, P. & Kiefer, B. Density Functional Theory Study of the Oxygen Reduction Reaction Mechanism in a BN co-doped Graphene Electrocatalyst. *Journal of Materials Chemistry A* **2**, 10273-10279 (2014).
142. Zheng, Y., Jiao, Y., Ge, L., Jaroniec, M. & Qiao, S.Z. Two-Step Boron and Nitrogen Doping in Graphene for Enhanced Synergistic Catalysis. *Angewandte Chemie International Edition* **52**, 3110-3116 (2013).
143. Liang, J., Jiao, Y., Jaroniec, M. & Qiao, S.Z. Sulfur and Nitrogen Dual-Doped Mesoporous Graphene Electrocatalyst for Oxygen Reduction with Synergistically Enhanced Performance. *Angewandte Chemie International Edition* **51**, 11496-11500 (2012).
144. Yu, D., Xue, Y. & Dai, L. Vertically Aligned Carbon Nanotube Arrays Co-doped with Phosphorus and Nitrogen as Efficient Metal-Free Electrocatalysts for Oxygen Reduction. *Journal of Physical Chemistry Letters* **3**, 2863-2870 (2012).

145. Choi, C.H., Park, S.H. & Woo, S.I. Binary and Ternary Doping of Nitrogen, Boron, and Phosphorus into Carbon for Enhancing Electrochemical Oxygen Reduction Activity. *ACS Nano* **6**, 7084-7091 (2012).
146. Zhao, Z. & Xia, Z. Interactions between Dopants in Dual-Doped Graphene Nanoribbons as Metal-Free Bifunctional Catalysts for Fuel Cell and Metal-Air Batteries. *MRS Advances* **1**, 421-425 (2016).
147. Damjanovic, A., Dey, A. & Bockris, J.O.M. Electrode Kinetics of Oxygen Evolution and Dissolution on Rh, Ir, and Pt-Rh Alloy Electrodes. *Journal of The Electrochemical Society* **113**, 739-746 (1966).
148. Danilovic, N., Subbaraman, R., Chang, K.-C., Chang, S.H., Kang, Y.J., Snyder, J., Paulikas, A.P., Strmcnik, D., Kim, Y.-T., Myers, D., Stamenkovic, V.R. & Markovic, N.M. Activity-Stability Trends for the Oxygen Evolution Reaction on Monometallic Oxides in Acidic Environments. *The Journal of Physical Chemistry Letters* **5**, 2474-2478 (2014).
149. Frydendal, R., Paoli, E.A., Knudsen, B.P., Wickman, B., Malacrida, P., Stephens, I.E.L. & Chorkendorff, I. Benchmarking the Stability of Oxygen Evolution Reaction Catalysts: The Importance of Monitoring Mass Losses. *ChemElectroChem* **1**, 2075-2081 (2014).
150. Kötz, R., Stucki, S., Scherson, D. & Kolb, D.M. In-situ Identification of RuO₄ as the Corrosion Product During Oxygen Evolution on Ruthenium in Acid Media. *Journal of Electroanalytical Chemistry and Interfacial Electrochemistry* **172**, 211-219 (1984).
151. McCrory, C.C.L., Jung, S., Peters, J.C. & Jaramillo, T.F. Benchmarking

- Heterogeneous Electrocatalysts for the Oxygen Evolution Reaction. *Journal of the American Chemical Society* **135**, 16977-16987 (2013).
152. Deng, X. & Tüysüz, H. Cobalt-Oxide-Based Materials as Water Oxidation Catalyst: Recent Progress and Challenges. *ACS Catalysis* **4**, 3701-3714 (2014).
153. Jiao, F. & Frei, H. Nanostructured Cobalt and Manganese Oxide Clusters as Efficient Water Oxidation Catalysts. *Energy & Environmental Science* **3**, 1018-1027 (2010).
154. Friebel, D., Louie, M.W., Bajdich, M., Sanwald, K.E., Cai, Y., Wise, A.M., Cheng, M.-J., Sokaras, D., Weng, T.-C., Alonso-Mori, R., Davis, R.C., Bargar, J.R., Nørskov, J.K., Nilsson, A. & Bell, A.T. Identification of Highly Active Fe Sites in (Ni,Fe)OOH for Electrocatalytic Water Splitting. *Journal of the American Chemical Society* **137**, 1305-1313 (2015).
155. Burke, M.S., Kast, M.G., Trotochaud, L., Smith, A.M. & Boettcher, S.W. Cobalt-Iron (Oxy)hydroxide Oxygen Evolution Electrocatalysts: The Role of Structure and Composition on Activity, Stability, and Mechanism. *Journal of the American Chemical Society* **137**, 3638-3648 (2015).
156. Louie, M.W. & Bell, A.T. An Investigation of Thin-Film Ni-Fe Oxide Catalysts for the Electrochemical Evolution of Oxygen. *Journal of the American Chemical Society* **135**, 12329-12337 (2013).
157. Bajdich, M., García-Mota, M., Vojvodic, A., Nørskov, J.K. & Bell, A.T. Theoretical Investigation of the Activity of Cobalt Oxides for the Electrochemical Oxidation of Water. *Journal of the American Chemical Society* **135**, 13521-13530 (2013).
158. McCrory, C.C.L., Jung, S., Ferrer, I.M., Chatman, S.M., Peters, J.C. & Jaramillo,

- T.F. Benchmarking Hydrogen Evolving Reaction and Oxygen Evolving Reaction Electrocatalysts for Solar Water Splitting Devices. *Journal of the American Chemical Society* **137**, 4347-4357 (2015).
159. Zhang, B., Zheng, X., Voznyy, O., Comin, R., Bajdich, M., García-Melchor, M., Han, L., Xu, J., Liu, M., Zheng, L., García de Arquer, F.P., Dinh, C.T., Fan, F., Yuan, M., Yassitepe, E., Chen, N., Regier, T., Liu, P., Li, Y., De Luna, P., Janmohamed, A. Xin, H.L., Yang, H., Vojvodic, A. & Sargent, E.H. Homogeneously Dispersed Multimetal Oxygen-evolving Catalysts. *Science* **352**, 333-337 (2016).
160. Zhao, Z. & Xia, Z. Design Principles for Dual-Element-Doped Carbon Nanomaterials as Efficient Bifunctional Catalysts for Oxygen Reduction and Evolution Reactions. *ACS Catalysis* **6**, 1553-1558 (2016).
161. Yang, H.B., Miao, J., Hung, S.-F., Chen, J., Tao, H.B., Wang, X., Zhang, L., Chen, R., Gao, J., Chen, H.M., Dai, L. & Liu, B. Identification of Catalytic Sites for Oxygen Reduction and Oxygen Evolution in N-doped Graphene Materials: Development of Highly Efficient Metal-free Bifunctional Electrocatalyst. *Science Advances* **2**, e1501122 (2016).
162. Wallace, P.R. The Band Theory of Graphite. *Physical Review* **71**, 622-634 (1947).
163. Geim, A.K. & Novoselov, K.S. The Rise of Graphene. *Nature Materials* **6**, 183-191 (2007).
164. Fradkin, E. Critical Behavior of Disordered Degenerate Semiconductors. II. Spectrum and Transport Properties in Mean-field Theory. *Physical Review B* **33**,

- 3263-3268 (1986).
165. Novoselov, K.S., Geim, A.K., Morozov, S.V., Jiang, D., Zhang, Y., Dubonos, S.V., Grigorieva, I.V. & Firsov, A.A. Electric Field Effect in Atomically Thin Carbon Films. *Science* **306**, 666-669 (2004).
166. Ruoff, R. Graphene: Calling all Chemists. *Nature Nanotechnology* **3**, 10-11 (2008).
167. Zhu, Y., Murali, S., Cai, W., Li, X., Suk, J.W., Potts, J.R. & Ruoff, R.S. Graphene and Graphene Oxide: Synthesis, Properties, and Applications. *Advanced Materials* **22**, 3906-3924 (2010).
168. Dreyer, D.R., Park, S., Bielawski, C.W. & Ruoff, R.S. The Chemistry of Graphene Oxide. *Chemical Society Reviews* **39**, 228-240 (2010).
169. Geim, A.K. Graphene: Status and Prospects. *Science* **324**, 1530-1534 (2009).
170. Stoller, M.D., Park, S., Zhu, Y., An, J. & Ruoff, R.S. Graphene-Based Ultracapacitors. *Nano Letters* **8**, 3498-3502 (2008).
171. Morozov, S.V., Novoselov, K.S., Katsnelson, M.I., Schedin, F., Elias, D.C. Jaszczak, J.A. & Geim, A.K. Giant Intrinsic Carrier Mobilities in Graphene and Its Bilayer. *Physical Review Letters* **100**, 016602 (2008).
172. Balandin, A.A., Ghosh, S., Bao, W., Calizo, I., Teweldebrhan, D., Miao, F. & Lau, C.N. Superior Thermal Conductivity of Single-Layer Graphene. *Nano Letters* **8**, 902-907 (2008).
173. Lee, C., Wei, X., Kysar, J.W. & Hone, J. Measurement of the Elastic Properties and Intrinsic Strength of Monolayer Graphene. *Science* **321**, 385-388 (2008).
174. Singh, V., Joung, D., Zhai, L., Das, S., Khondaker, S.I. & Seal, S. Graphene

- based Materials: Past, Present and Future. *Progress in Materials Science* **56**, 1178-1271 (2011).
175. Huang, X., Yin, Z., Wu, S., Qi, X., He, Q., Zhang, Q., Yan, Q., Boey, F. & Zhang, H. Graphene-Based Materials: Synthesis, Characterization, Properties, and Applications. *Small* **7**, 1876-1902 (2011).
176. Xu, C., Xu, B., Gu, Y., Xiong, Z., Sun, J. & Zhao, X.S. Graphene-based Electrodes for Electrochemical Energy Storage. *Energy & Environmental Science* **6**, 1388-1414 (2013).
177. Reina, A., Jia, X., Ho, J., Nezich, D., Son, H., Bulovic, V., Dresselhaus, M.S. & Kong, J. Large Area, Few-Layer Graphene Films on Arbitrary Substrates by Chemical Vapor Deposition. *Nano Letters* **9**, 30-35 (2009).
178. Li, X., Cai, W., An, J., Kim, S., Nah, J., Yang, D., Piner, R., Velamakanni, A., Jung, I., Tutuc, E., Banerjee, S.K., Colombo, L. & Ruoff, R.S. Large-Area Synthesis of High-Quality and Uniform Graphene Films on Copper Foils. *Science* **324**, 1312-1314 (2009).
179. Wang, Y., Xu, X., Lu, J., Lin, M., Bao, Q., Özyilmaz, B. & Loh, K.P. Toward High Throughput Interconvertible Graphene-to-Graphene Growth and Patterning. *ACS Nano* **4**, 6146-6152 (2010).
180. Berger, C., Song, Z. Li, X., Wu, X., Brown, N., Naud, C., Mayou, D., Li, T., Hass, J., Marchenkov, A.N., Conrad, E.H., First, P.N. & de Heer, W.A. Electronic Confinement and Coherence in Patterned Epitaxial Graphene. *Science* **312**, 1191-1196 (2006).
181. Emtsev, K.V., Bostwick, A., Horn, K., Jobst, J., Kellogg, G.L., Ley, L., McChesney,

- J.L., Ohta, T., Reshanov, S.A., Rohrl, J., Rotenberg, E., Schmid, A.K., Waldmann, D., Weber, H.B. & Seyller, T. Towards Wafer-size Graphene Layers by Atmospheric Pressure Graphitization of Silicon Carbide. *Nature Materials* **8**, 203-207 (2009).
182. Choucair, M., Thordarson, P. & Stride, J.A. Gram-scale Production of Graphene based on Solvothermal Synthesis and Sonication. *Nature Nanotechnology* **4**, 30-33 (2009).
183. Wang, X., Zhi, L., Tsao, N., Tomović, Ž., Li, J. & Müllen, K. Transparent Carbon Films as Electrodes in Organic Solar Cells. *Angewandte Chemie International Edition* **47**, 2990-2992 (2008).
184. Yan, X., Cui, X. & Li, L.-s. Synthesis of Large, Stable Colloidal Graphene Quantum Dots with Tunable Size. *Journal of the American Chemical Society* **132**, 5944-5945 (2010).
185. Hernandez, Y., Nicolosi, V., Lotya, M., Blighe, F.M., Sun, Z., De, S., McGovern, I.T., Holland, B., Byrne, M., Gun'Ko, Y.K., Boland, J.J., Niraj, P. Duesberg, G., Krishnamurthy, S., Goodhue, R., Hutchison, J., Scardaci, V., Ferrari, A.C. & Coleman, J.N. High-yield Production of Graphene by Liquid-phase Exfoliation of Graphite. *Nature Nanotechnology* **3**, 563-568 (2008).
186. Guo, H.-L., Wang, X.-F., Qian, Q.-Y., Wang, F.-B. & Xia, X.-H. A Green Approach to the Synthesis of Graphene Nanosheets. *ACS Nano* **3**, 2653-2659 (2009).
187. Dikin, D.A., Stankovich, S., Zimney, E.J., Piner, R.D., Dommett, G.H.B., Evmenenko, G., Nguyen, S.T. & Ruoff, R.S. Preparation and Characterization of Graphene Oxide Paper. *Nature* **448**, 457-460 (2007).

188. Lee, J.H., Shin, D.W., Makotchenko, V.G., Nazarov, A.S., Fedorov, V.E., Kim, Y.H., Choi, J.-Y., Kim, J.M. & Yoo, J.-B. One-Step Exfoliation Synthesis of Easily Soluble Graphite and Transparent Conducting Graphene Sheets. *Advanced Materials* **21**, 4383-4387 (2009).
189. Vallés, C., Drummond, C., Saadaoui, H., Furtado, C.A., He, M., Roubeau, O., Ortolani, L., Monthieux, M. & Pénicaud, A. Solutions of Negatively Charged Graphene Sheets and Ribbons. *Journal of the American Chemical Society* **130**, 15802-15804 (2008).
190. Burrell, J.W., Gadipelli, S., Ford, J., Simmons, J.M., Zhou, W. & Yildirim, T. Graphene Oxide Framework Materials: Theoretical Predictions and Experimental Results. *Angewandte Chemie International Edition* **49**, 8902-8904 (2010).
191. Qiu, K. & Guo, Z.X. Hierarchically Porous Graphene Sheets and Graphitic Carbon Nitride Intercalated Composites for Enhanced Oxygen Reduction Reaction. *Journal of Materials Chemistry A* **2**, 3209-3215 (2014).
192. Wang, X., Maeda, K., Thomas, A., Takahashi, K., Xin, G., Carlsson, J.M., Domen, K. & Antonietti, M. A Metal-free Polymeric Photocatalyst for Hydrogen Production from Water under Visible Light. *Nature Materials* **8**, 76-80 (2009).
193. Qiu, K., Chai, G.-L., Jiang, C., Ling, M., Tang, J. & Guo, Z. Highly Efficient Oxygen Reduction Catalysts by Rational Synthesis of Nanoconfined Maghemite in a Nitrogen-Doped Graphene Framework. *ACS Catalysis* **6**, 3558-3568 (2016).
194. Ferrero, G.A., Preuss, K., Fuertes, A.B., Sevilla, M. & Titirici, M.M. The Influence of Pore Size Distribution on the Oxygen Reduction Reaction Performance in

- Nitrogen Doped Carbon Microspheres. *Journal of Materials Chemistry A* **4**, 2581-2589 (2016).
195. Huang, S.-F., Terakura, K., Ozaki, T., Ikeda, T., Boero, M., Oshima, M., Ozaki, J. & Miyata, S. First-principles Calculation of the Electronic Properties of Graphene Clusters Doped with Nitrogen and Boron: Analysis of Catalytic Activity for the Oxygen Reduction Reaction. *Physical Review B* **80**, 235410 (2009).
196. Hu, X., Wu, Y., Li, H. & Zhang, Z. Adsorption and Activation of O₂ on Nitrogen-Doped Carbon Nanotubes. *The Journal of Physical Chemistry C* **114**, 9603-9607 (2010).
197. Yang, S., Feng, X., Wang, X. & Müllen, K. Graphene-Based Carbon Nitride Nanosheets as Efficient Metal-Free Electrocatalysts for Oxygen Reduction Reactions. *Angewandte Chemie International Edition* **50**, 5339-5343 (2011).
198. Chen, S., Bi, J., Zhao, Y., Yang, L., Zhang, C., Ma, Y., Wu, Q., Wang, X. & Hu, Z. Nitrogen-Doped Carbon Nanocages as Efficient Metal-Free Electrocatalysts for Oxygen Reduction Reaction. *Advanced Materials* **24**, 5593-5597 (2012).
199. Sharifi, T., Hu, G., Jia, X. & Wågberg, T. Formation of Active Sites for Oxygen Reduction Reactions by Transformation of Nitrogen Functionalities in Nitrogen-Doped Carbon Nanotubes. *ACS Nano* **6**, 8904-8912 (2012).
200. Lai, L., Potts, J.R., Zhan, D., Wang, L., Poh, C.K., Tang, C., Gong, H., Shen, Z., Lin, J. & Ruoff, R.S. Exploration of the Active Center Structure of Nitrogen-doped Graphene-based Catalysts for Oxygen Reduction Reaction. *Energy & Environmental Science* **5**, 7936-7942 (2012).
201. Thomas, A., Fischer, A., Goettmann, F., Antonietti, M., Müller, J.-O., Schlogl, R.

- & Carlsson, J.M. Graphitic Carbon Nitride Materials: Variation of Structure and Morphology and Their Use as Metal-free Catalysts. *Journal of Materials Chemistry* **18**, 4893-4908 (2008).
202. Niu, P., Zhang, L.L., Liu, G. & Cheng, H.M. Graphene-Like Carbon Nitride Nanosheets for Improved Photocatalytic Activities. *Advanced Functional Materials* **22**, 4763-4770 (2012).
203. Zheng, Y., Liu, J., Liang, J., Jaroniec, M. & Qiao, S.Z. Graphitic Carbon Nitride Materials: Controllable Synthesis and Applications in Fuel Cells and Photocatalysis. *Energy & Environmental Science* **5**, 6717-6731 (2012).
204. Sun, Y., Li, C., Xu, Y., Bai, H., Yao, Z. & Shi, G. Chemically Converted Graphene as Substrate for Immobilizing and Enhancing the Activity of a Polymeric Catalyst. *Chemical Communications* **46**, 4740-4742 (2010).
205. Zheng, Y., Jiao, Y., Chen, J., Liu, J., Liang, J., Du, A., Zhang, W., Zhu, Z., Smith, S.C., Jaroniec, M., Lu, G.Q. & Qiao, S.Z. Nanoporous Graphitic-C₃N₄@Carbon Metal-Free Electrocatalysts for Highly Efficient Oxygen Reduction. *Journal of the American Chemical Society* **133**, 20116-20119 (2011).
206. Lyth, S.M., Nabaee, Y., Moriya, S., Kuroki, S., Kakimoto, M., Ozaki, J. & Miyata, S. Carbon Nitride as a Nonprecious Catalyst for Electrochemical Oxygen Reduction. *The Journal of Physical Chemistry C* **113**, 20148-20151 (2009).
207. Liang, J., Zheng, Y., Chen, J., Liu, J., Hulicova-Jurcakova, D., Jaroniec, M. & Qiao, S.Z. Facile Oxygen Reduction on a Three-Dimensionally Ordered Macroporous Graphitic C₃N₄/Carbon Composite Electrocatalyst. *Angewandte Chemie-International Edition* **51**, 3892-3896 (2012).

208. Pei, S. & Cheng, H.-M. The Reduction of Graphene Oxide. *Carbon* **50**, 3210-3228 (2012).
209. Du, A., Sanvito, S., Li, Z., Wang, D., Jiao, Y., Liao, T., Sun, Q., Ng, Y.H., Zhu, Z. Amal, R. & Smith, S.C. Hybrid Graphene and Graphitic Carbon Nitride Nanocomposite: Gap Opening, Electron–Hole Puddle, Interfacial Charge Transfer, and Enhanced Visible Light Response. *Journal of the American Chemical Society* **134**, 4393-4397 (2012).
210. Kwon, K., Sa, Y.J., Cheon, J.Y. & Joo, S.H. Ordered Mesoporous Carbon Nitrides with Graphitic Frameworks as Metal-Free, Highly Durable, Methanol-Tolerant Oxygen Reduction Catalysts in an Acidic Medium. *Langmuir* **28**, 991-996 (2012).
211. Zhu, Y., Murali, S., Stoller, M.D., Velamakanni, A., Piner, R.D. & Ruoff, R.S. Microwave Assisted Exfoliation and Reduction of Graphite Oxide for Ultracapacitors. *Carbon* **48**, 2118-2122 (2010).
212. Vivekchand, S.R.C., Rout, C.S., Subrahmanyam, K.S., Govindaraj, A. & Rao, C.N.R. Graphene-based Electrochemical Supercapacitors. *Journal of Chemical Sciences* **120**, 9-13 (2008).
213. Bojdys, M.J., Müller, J.-O., Antonietti, M. & Thomas, A. Ionothermal Synthesis of Crystalline, Condensed, Graphitic Carbon Nitride. *Chemistry – A European Journal* **14**, 8177-8182 (2008).
214. Yan, S.C., Li, Z.S. & Zou, Z.G. Photodegradation Performance of g-C₃N₄ Fabricated by Directly Heating Melamine. *Langmuir* **25**, 10397-10401 (2009).
215. Dong, F., Wu, L., Sun, Y., Fu, M., Wu, Z. & Lee, S.C. Efficient Synthesis of

- Polymeric g-C₃N₄ Layered Materials as Novel Efficient Visible Light Driven Photocatalysts. *Journal of Materials Chemistry* **21**, 15171-15174 (2011).
216. Liu, J., Zhang, T., Wang, Z., Dawson, G. & Chen, W. Simple Pyrolysis of Urea into Graphitic Carbon Nitride with Recyclable Adsorption and Photocatalytic Activity. *Journal of Materials Chemistry* **21**, 14398-14401 (2011).
217. Zhang, Y., Mori, T., Niu, L. & Ye, J. Non-covalent Doping of Graphitic Carbon Nitride Polymer with Graphene: Controlled Electronic Structure and Enhanced Optoelectronic Conversion. *Energy & Environmental Science* **4**, 4517-4521 (2011).
218. Li, X., Wang, H., Robinson, J.T., Sanchez, H., Diankov, G. & Dai, H. Simultaneous Nitrogen Doping and Reduction of Graphene Oxide. *Journal of the American Chemical Society* **131**, 15939-15944 (2009).
219. Wang, H., Maiyalagan, T. & Wang, X. Review on Recent Progress in Nitrogen-Doped Graphene: Synthesis, Characterization, and Its Potential Applications. *ACS Catalysis* **2**, 781-794 (2012).
220. Li, X.-H., Chen, J.-S., Wang, X., Sun, J. & Antonietti, M. Metal-Free Activation of Dioxygen by Graphene/g-C₃N₄ Nanocomposites: Functional Dyads for Selective Oxidation of Saturated Hydrocarbons. *Journal of the American Chemical Society* **133**, 8074-8077 (2011).
221. Liang, J., Du, X., Gibson, C., Du, X.W. & Qiao, S.Z. N-Doped Graphene Natively Grown on Hierarchical Ordered Porous Carbon for Enhanced Oxygen Reduction. *Advanced Materials* **25**, 6226-6231 (2013).
222. Liu, R., Wu, D., Feng, X. & Müllen, K. Nitrogen-Doped Ordered Mesoporous

- Graphitic Arrays with High Electrocatalytic Activity for Oxygen Reduction. *Angewandte Chemie International Edition* **49**, 2565-2569 (2010).
223. Yang, W., Fellingner, T.-P. & Antonietti, M. Efficient Metal-Free Oxygen Reduction in Alkaline Medium on High-Surface-Area Mesoporous Nitrogen-Doped Carbons Made from Ionic Liquids and Nucleobases. *Journal of the American Chemical Society* **133**, 206-209 (2011).
224. Bezerra, C.W.B., Zhang, L., Lee, K., Liu, H., Marques, A.L.B., Marques, E.P. Wang, H. & Zhang, J. A Review of Fe–N/C and Co–N/C Catalysts for the Oxygen Reduction Reaction. *Electrochimica Acta* **53**, 4937-4951 (2008).
225. Wang, H. & Dai, H. Strongly Coupled Inorganic-Nanocarbon Hybrid Materials for Energy Storage. *Chemical Society Reviews* **42**, 3088-3113 (2013).
226. Yaldagard, M., Jahanshahi, M. & Seghatoleslami, N. Carbonaceous Nanostructured Support Materials for Low Temperature Fuel Cell Electrocatalysts - A Review. *World Journal of Nano Science and Engineering* **3**, 33 (2013).
227. Zadick, A., Dubau, L., Sergent, N., Berthomé, G. & Chatenet, M. Huge Instability of Pt/C Catalysts in Alkaline Medium. *ACS Catalysis* **5**, 4819-4824 (2015).
228. Cao, R., Thapa, R., Kim, H., Xu, X.G., Kim, M., Li, Q., Park, N., Liu, M. & Cho, J. Promotion of Oxygen Reduction by a Bio-inspired Tethered Iron Phthalocyanine Carbon Nanotube-based Catalyst. *Nature Communications* **4**, 2076 (2013).
229. Kong, A., Zhu, X., Han, Z., Yu, Y., Zhang, Y., Dong, B. & Shan, Y. Ordered Hierarchically Micro- and Mesoporous Fe–N_x-Embedded Graphitic Architectures as Efficient Electrocatalysts for Oxygen Reduction Reaction. *ACS Catalysis* **4**,

1793-1800 (2014).

230. Liu, J., Sun, X., Song, P., Zhang, Y., Xing, W. & Xu, W. High-Performance Oxygen Reduction Electrocatalysts based on Cheap Carbon Black, Nitrogen, and Trace Iron. *Advanced Materials* **25**, 6879-6883 (2013).
231. Tian, G.-L., Zhao, M.-Q, Yu, D., Kong, X.-Y., Huang, J.-Q., Zhang, Q. & Wei, F. Nitrogen-Doped Graphene/Carbon Nanotube Hybrids: In Situ Formation on Bifunctional Catalysts and Their Superior Electrocatalytic Activity for Oxygen Evolution/Reduction Reaction. *Small* **10**, 2251-2259 (2014).
232. Shao, Z., Zhang, W., An, D., Zhang, G. & Wang, Y. Pyrolyzed Egg Yolk as an Efficient Bifunctional Electrocatalyst for Oxygen Reduction and Evolution Reactions. *RSC Advances* **5**, 97508-97511 (2015).
233. Liu, Q., Wang, Y., Dai, L. & Yao, J. Scalable Fabrication of Nanoporous Carbon Fiber Films as Bifunctional Catalytic Electrodes for Flexible Zn-Air Batteries. *Advanced Materials* **28**, 3000-3006 (2016).